REPORT DOCUMENTATION PAGE			Form Approved OMB No. 0704-0188

1. AGENCY USE ONLY *(Leave blank)*	2. REPORT DATE	3. REPORT TYPE AND DATES COVERED
	14.Oct.98	THESIS

4. TITLE AND SUBTITLE
A STUDY OF FRETTING FATIGUE IN AIRCRAFT COMPONENTS

5. FUNDING NUMBERS

6. AUTHOR(S)
2D LT BIRCH PAUL R

7. PERFORMING ORGANIZATION NAME(S) AND ADDRESS(ES)
MASSACHUSETTS INSTITUTE OF TECHNOLOGY

8. PERFORMING ORGANIZATION REPORT NUMBER

9. SPONSORING/MONITORING AGENCY NAME(S) AND ADDRESS(ES)
THE DEPARTMENT OF THE AIR FORCE
AFIT/CIA, BLDG 125
2950 P STREET
WPAFB OH 45433

10. SPONSORING/MONITORING AGENCY REPORT NUMBER
98-088

11. SUPPLEMENTARY NOTES

12a. DISTRIBUTION AVAILABILITY STATEMENT
Unlimited distribution
In Accordance With AFI 35-205/AFIT Sup 1

12b. DISTRIBUTION CODE

13. ABSTRACT *(Maximum 200 words)*

14. SUBJECT TERMS			15. NUMBER OF PAGES
			16. PRICE CODE
17. SECURITY CLASSIFICATION OF REPORT	18. SECURITY CLASSIFICATION OF THIS PAGE	19. SECURITY CLASSIFICATION OF ABSTRACT	20. LIMITATION OF ABSTRACT

A Study of Fretting Fatigue in Aircraft Components

by

Paul R. Birch

B.S., Engineering Mechanics (1996)

United States Air Force Academy

Submitted to the Department of Materials Science and Engineering
on May 8, 1998, in partial fulfillment of the
requirements for the degree of
Master of Science in Materials Science and Engineering

Abstract

This thesis presents theoretical, computational, and experimental approaches to the problem of fretting fatigue in materials systems relevant to aircraft components. The basic contact mechanics for fretting fatigue in a sphere-plane contact geometry are reviewed. Various elastic criteria for predicting fretting failure are discussed; selected fretting maps created from one of these — the modified Crossland criterion — are presented. Fail/no-fail predictions based on these maps have verified trends observed in experimental work performed on Al 7075-T6 specimens. A three-dimensional finite element model of sphere-plane fretting contact is reviewed. This model has been used to model elastic and elastoplastic fretting contact. The evolution of tangential loads coincident with plastic flow has been simulated, as well as the accumulation of equivalent plastic strains for these fretting conditions. This information may be used to predict the life of components subject to fretting contact high cycle fatigue (HCF) via a Coffin-Manson type relation. Design and construction of an apparatus for performing quantitative fretting experiments are described, and results of early tests performed on 7075-T6 aluminum alloys are presented. These experiments validate the proper operation of the experimental apparatus. Finally, basic principles of fracture mechanics and the limitations of applying traditional linear elastic fracture mechanics (LEFM) to fretting fatigue are discussed. The new crack analogue concept of Giannakopoulos et al. is reviewed as a means of uniting LEFM and fretting contact mechanics to achieve a life prediction scheme for components subject to HCF that is superior to the modified Goodman diagram approach currently employed by the US Air Force.

Thesis Supervisor: Subra Suresh
Title: Richard P. Simmons Professor of Metallurgy
Professor of Mechanical Engineering

Thesis Supervisor: Antonios E. Giannakopoulos
Title: Research Scientist

A Study of Fretting Fatigue in Aircraft Components

by

Paul R. Birch
B.S., Engineering Mechanics (1996)
United States Air Force Academy

Submitted to the Department of Materials Science and Engineering
in partial fulfillment of the requirements for the degree of

Master of Science in Materials Science and Engineering

at the

MASSACHUSETTS INSTITUTE OF TECHNOLOGY

June 1998

Author .....
Department of Materials Science and Engineering
May 8, 1998

Certified by .....
Subra Suresh
Richard P. Simmons Professor of Metallurgy
Professor of Mechanical Engineering
Thesis Supervisor

Certified by .....
Antonios E. Giannakopoulos
Research Scientist
Thesis Supervisor

Accepted by .....
Linn Hobbs
John F. Elliott Professor of Materials
Chairman, Department Committee on Graduate Students

Acknowledgments

This work was supported by the Multi-University Research Initiative on "High-Cycle Fatigue", which is funded at MIT by the Air Force Office of Scientific Research, Grant No. F49620-96-1-0478, through a subcontract from the University of California at Berkeley.

This material is based upon work supported under a National Science Foundation Graduate Fellowship.

I would like to thank Prof. Jaime Dominguez and Dr. Bettina U. Wittkowsy for their guidance and help in performing the experimental section of this work, and Mr. George Labonte for his invaluable assistance. I am also indebted to Prof. Dominguez for his assistance in creation of analytical fretting maps. The finite element work I have completed would have been beyond my grasp but for the patient assistance of Dr. Antonious E. Giannakopoulos, who also spent countless hours discussing the problem of fretting contact in general with me.

Above all, I am grateful to Prof. Subra Suresh for the opportunity to work in his LEXCOM group at MIT. It has been a very rewarding experience.

Additionally, I would like to acknowledge the following people and organizations: Dr. William L. Hallauer, the National Science Foundation, the Air Force Office of Scientific Research, the University of California at Berkeley, Professor Robert S. Ritchie, Andrew Gouldstone (who kept me sane at MIT), Professor Jaime Dominguez, Amanda S. Birch (who brought joy into my life at MIT and beyond), the Air Force Institute of Technology, Air Force ROTC Detachment 365, Aaron T. Hicks, Toby M. Freyman, Dr. Ching-Te Lin, Fred Gaudette, Olivera Kesler, Raj Thampuran, Ricardo Torres, Otmar Kolednik, Patrick Palloux, Trevor Lindley, all the rest of the LEXCOM group I've not named here, Robert and Sylvia Birch, Richard and Marjorie Myers, and the First United Presbyterian Church of Cambridge.

The fear of the Lord is the beginning of knowledge,
but fools despise wisdom and discipline. –Prov. 2:9

Contents

List of Figures

List of Tables

Chapter 1

Background & Literature Survey

1.1 Definitions & history

1.1.1 Definitions

Fretting is the application of oscillating tangential forces to two nominally clamped free surfaces. Although the surfaces may appear to be stationary with respect to one another, sections move relative to one another, creating regions of microslip. Fretting may cause considerable damage, both via stress effects and through the wear-induced formation of third body particles in the contact area. The surface damage associated with the wear that occurs in fretting is naturally termed *fretting wear*, e.g. see Waterhouse (1972, 1981). When either or both of the contacting bodies are subjected to repeated loads that can cause the initiation and propagation of fatigue cracks, the system is said to experience *fretting fatigue*. (This loading may be due to the stresses transmitted across the interface or because of oscillatory loading conditions far from the contact region.) Many experimentalists have demonstrated that the presence of fretting along with fatigue conditions can significantly reduce the life of a component relative to its *plain* (i.e., without fretting) *fatigue* life; cf. Forsyth (1981) and Hoeppner (1974*a*). Deleterious effects on fatigue life are exacerbated if fretting occurs in a chemically corrosive atmosphere; fretting in a corrosive environment is termed *fretting corrosion*; see Suresh (1998). *Fretting damage* refers broadly to any damage

mechanism occurring under conditions of fretting contact, as in Vincent (1992).

1.1.2 Abridged summary of fretting research

The first identification of fretting fatigue came from Eden et al. (1911) in the early part of this century, who noted the formation of iron oxide on the surface of a fatigue specimen in the areas contacting the grips of a test machine. Tomlinson (1927) performed the first scientific study of the phenomenon (again using steel) and concluded that it was related to tangential motion between contacting surfaces. Other researchers, e.g. Peterson (1935), Evans (1937), Almen (1937), Campbell (1938, 1939), helped sustain interest in fretting with their work, and knowledge of it increased so that by 1939 Tomlinson and co-workers could assert that fretting was purely a mechanical process that involved microslip. In 1941, Warlow-Davies proved conclusively that fretting reduced fatigue strength. He separated the effects of fretting and the unknown stress concentration induced by a fretting contact when he fretted specimens in the absence of bulk stresses and compared their fatigue strength to unfretted specimens in subsequent fatigue tests.

Nowell (1988) points out that after World War II, research into fretting diverged into two bodies: scientific literature began to distinguish *fretting wear* from *fretting fatigue*. Godfrey (1950) discovered that adhesion occurred in fretting contact and that fine debris particles broke loose and were oxidized, and Feng and Rightmire (1952) proposed mechanistic fretting models. Uhlig and Feng (1953) refined these ideas, and Uhlig (1954) developed a model that described fretting in terms of both mechanical and chemical variables.

The first of many symposia on fretting fatigue was sponsored by the ASTM in 1952, bringing together several investigators and spawning much new research. The phenomenon of fretting was at that time referred to as *friction oxidation*, *wear oxidation*, *false brinelling*, *bleeding*, and *'cocoa'*. Waterhouse, who has now researched fretting fatigue for over four decades, published his first paper on the topic in 1955, and was one of the first (1961) to discuss the possibility of the occurrence and consequences of a temperature rise in the contact zone.

US military concern over fretting fatigue was first tangibly manifest in Comyn and Furlani's (1963) literature review. According to Hoeppner (1994), real application of the scientific investigation of fretting fatigue to engineering practice commenced around 1965, with the development of the concept of a life reduction factor for fretting. The work of well-known fretting investigators Nishioka, Nishimura, and Hirakawa emerged in 1968-69, as did that of Endo and Goto. Nishioka et al.'s publications led them to propose a model for predicting fatigue life under fretting conditions that was a function slip amplitude, contact pressure, and materials. This body of work identified many fretting parameters that remain of interest to investigators and is discussed in more detail in section 1.2. Endo and Goto's first work on fretting dealt with environmental effects in fretting, although their later application of fracture mechanics to fretting fatigue is very important. Hoeppner (1994) notes that it was the first such attempt in the field. Similarly, it is discussed further in section 1.2.

Work on fretting fatigue in the 1970s and 80s continued to advance understanding of its mechanisms, and dozens of papers dedicated to it were produced. Hurricks (1970) identified three stages present in fretting mechanisms:

$\rightarrow$ initial adhesion and metal transfer;

$\rightarrow$ production of debris in a normally oxidized state;

$\rightarrow$ steady state wear condition.

Concurrently, further understanding of environmental effects on fretting was gained, e.g. Waterhouse (1971*a*,1971*b*) and Hurricks (1972). The prevailing conclusion of the day was that fretting effects arose from mechanical surface damage. The concept of a fretting damage envelope was developed, as well as the idea of a damage threshold; cf. Hoeppner (1974). A NATO conference on fretting fatigue in aircraft components in 1974 added to the existing impetus to perform research. Situations that caused fretting, and engineering design approaches for avoiding it, received attention; cf. Hoeppner (1981*a*, 1981*b*).

Notable among many important developments later in the same era was the use of fracture mechanics to predict crack growth under fretting fatigue conditions. Along

with Endo's (1976) work already mentioned, Edwards' (1981) paper marks the beginning of the application of this tool to the problem. Another application-oriented research area came into focus via papers exploring the issue of fretting fatigue in orthopedic implants; cf. Brown (1981) and Cook (1983).

In the middle to late 1980s, Johnson's (1985) excellent contact mechanics monograph solidified the understanding of one of the key components of fretting fatigue, namely the conditions of stress and strain resulting at the interface between two bodies. Journal literature began to call greater attention to the importance of third body matter in fretting; cf. Colombie (1984, 1986) and Berthier (1987). Nix (1985*a*, 1985*b*) and Lindley (1985) produced notable case studies that incorporated fretting fatigue damage and the application of fracture mechanics to the propagation of cracks that resulted. There developed (and remains) speculation by some that a localized rise in temperature accompanies fretting contact, notably Attia (1985, 1986), and the application of fracture mechanics to fretting continued; cf. Hattori (1988).

Interest in fretting fatigue continues, as the problem has not been solved by any estimation. Nowell and Hills (1990) merit mention as prominent investigators in this area since 1988. In his doctoral thesis, Nowell (1988) examined fretting crack initiation and its effect on fatigue life in an Al/4%Cu alloy. He utilized cylindrical fretting pads for the experimental part of his research, as the elastic fields resulting from cylinder-plane contact are known and hence amenable to linear elastic fracture mechanics (LEFM) analysis for fatigue crack growth prediction. The present work employs the same logic in its selection of sphere-plane contact for experimentation. The book on fretting fatigue by Hills and Nowell (1994) is an excellent recent refinement of the application of contact mechanics, LEFM, and fracture mechanics in general to the problem. Discussion of various experimental methods continues in section 1.2. General discussion of the problem of fretting fatigue and some related research concludes here with Table 1.1, which lists locations of some common fretting fatigue failures and areas of concern in current research, as compiled by Suresh (1998).

1.2 Fretting experimentation

It is apparent after a cursory review of the literature that the variables and phenomena involved in fretting fatigue are great in number. Del Puglia et al. (1994) list some thirty-one parameters monitored in their fretting tests. Earlier, Beard (1982) listed more than fifty parameters of concern in fretting. The paring of these variables to a much smaller critical list is desirable for a focused and meaningful academic study, but critical for application of academia's results to service conditions. This identification of critical fretting parameters has been either an aim or an end in all fretting experimentation to date.

1.2.1 Abridged summary of fretting experiments

The first formal experimentation dealing with fretting fatigue was Tomlinson's (1927) work, which as discussed earlier led him to the important conclusion that fretting damage related to tangential motion between two sufaces. He and other investigators (1939) continued experiments from which they concluded that fretting was a purely mechanical phenomenon that arose from microslip. Warlow-Davies (1941) solved the question that Tomlinson et al. could not answer, i.e. whether fretting imposed a strength reduction, by fretting specimens in the absence of bulk stresses and finding that their subsequent fatigue strength was reduced by up to 18% as compared to unfretted specimens.

Following World War II, Uhlig and Ming Feng (1953,1954) performed work that led to a mechanical and chemical explanation for the fretting wear mechanism. Fenner and Field (1960) soon after this developed their popular 'bridge' fretting test pad, incorporating two flat surfaces that contact two distinct areas on a single side of a fretting specimen (see Figure 1-1) and used by many researchers; cf. Doeser (1981) and Edwards (1981). In contrast, Milestone (1970) pioneered the use of cylindrical fretting pads, which enjoy the benefit of having an analytically calculable stress field beneath the contact.

Nishioka and Hirakawa's (1969*a*) extensive contribution to the body of exper-

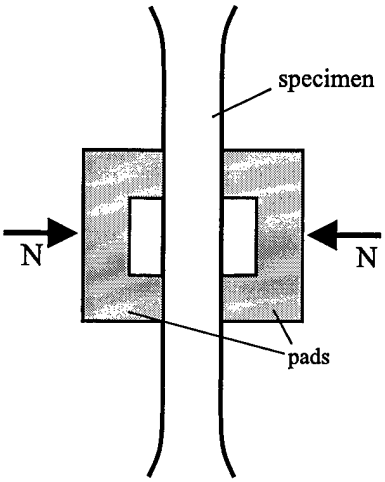

Figure 1-1: Showing 'bridge'-type fretting pads.

imental research in fretting fatigue utilized cylindrical steel pads contacting steel specimens. They reported non-propagating fretting fatigue cracks, evidence that while fretting damage may contribute to the initiation and early growth of cracks, these cracks may self-arrest under certain loading conditions. In the same work, they identified a critical range of slip amplitude for which fretting damage is of concern: minimal life reduction occurs at an amplitude below 5 μm; a slip amplitude above 50 μm did not contribute to observed crack growth because extensive wear removes incipient cracks before they propagate. In the 5–50 μm slip range, fatigue strength was as little as 1/8 that of unfretted specimens, making this range of slip amplitude of critical concern in fretting. These investigators (1969*b*) found that fatigue cracks initiated in the high stress regions near the edge of contact and initially propagated at an angle oblique to the surface of the specimen. This article described an increase in the coefficient of friction μ during the course of a test from 0.2 initially to a limit of 0.67 after about 100 cycles. This changing friction coefficient was observed by other researchers, including Milestone (1971) and Endo (1974), and remains an important consideration in the conduct and analysis of fretting experiments. Nishioka and Hirakawa (1969*c*) further separated the crack initiation effects of fretting fatigue from the bulk stresses that may occur in a specimen. Increasing mean stress had little effect on the rate of crack initiation, but a high mean stress did reduce fatigue

life. This suggests that fretting contributes to crack initiation, but that bulk stresses alone are responsible for any significant propagation. In their fourth fretting paper (1969*d*), the pair furthered knowledge of the effects of slip amplitude on fretting, showing first that tangential forces of a lesser amplitude than that needed to cause gross slip would cause microslip at the edges of contact. Tangential force and slip amplitude are dependent parameters, with greater force causing greater slip. This in turn decreases fatigue life, but the surface stresses created by the higher tangential force explain this effect; faster initiation of cracks is then a stronger function of the stresses created at the surface than it is of slip amplitude. Bryggman and Söderberg (1986) observed the same results, and named three distinct slip regimes:

→ elastic slip;

→ plastic slip;

→ gross sliding.

These regimes are discussed in depth in Chapter 2; fretting fatigue occurs only in the first two, under conditions of partial slip. The final paper in the Nishioka and Hirakawa series (1972) addressed material hardness and contact pressure effects. Hardness had a negligible influence on life; increased pressure led to a reduced life, but because experiments were performed with a fixed slip amplitude, the higher tangential forces sustained during the experiments were thought likely responsible for the life reduction.

Many other experimentalists have looked at the ramifications of varying other test parameters, including the effects of periodic high loads during fretting [Kantimathi (1981)], environmental conditions, bulk stress levels [Poon (1981)], and contact size [Bramhall (1973)]. Often an aspect of fretting tests involves careful observation of some aspects of crack initiation and growth. Frost et al. (1974) discussed the initiation and growth phases of fretting fatigue cracks. Endo and Goto (1976) have observed the variation of crack growth rate under fretting conditions. The recent work of Lamacq et al. (1997) in predicting and observing crack initiation angles is of particular note because of its potential use with the crack analogue method described in this work.

1.2.2 Regarding palliatives

Within the extensive body of fretting fatigue literature lie many researchers' thoughts and suggestions for ameliorating or eliminating the damaging effects of fretting fatigue. The conclusions reached are often contradictory. We discuss a few briefly to demonstrate this point.

Chivers and Gordelier (1979) reviewed some suggested palliatives for fretting fatigue. The early work of Nishioka and Hirakawa (1968, 1969*a–d*, 1972) leads to four basic suggestions: (*i*) raise the fatigue strength of the fretted components by choosing different materials, (*ii*) reduce the amount of relative slip to achieve only partial slip or to reduce the amplitude of partial slip present, (*iii*) reduce the contact pressure, and (*iv*) reduce the coefficient of friction. Obviously, these suggestions are practicable to a limited degree within the constraints of aircraft engine design. Several investigators have examined the effects of chemical surface coatings on fretting fatigue life. Waterhouse and Allery (1965) found that phosphated coatings greatly reduced fretting fatigue performance of unlubricated components, presumably for their reduction of material fatigue strength. An opposite finding is discussed by Wise and Burdon (1965), who found that the resulting increase in friction coefficient after application of these coatings reduced relative motion and thus reduced the amount of damage produced in contacting components. They also report favorable effects on fretting fatigue performance from chromium coatings, while researchers such as McDowell (1953) report deleterious effects. Chivers and Gordelier (1979) report that all investigators who have examined sulphidizing treatments have found them to increase fretting fatigue life because they increase the inherent fatigue strength of materials.

Surface mechanical treatments, including shot peening, cold rolling, roll peening, etc., are generally successful at inhibiting the initiation and growth of cracks due to fretting, and hence increase fatigue performance. Waters (1959) published a paper on cold working of all types to increase fretting fatigue life, finding an increase in life of up to 300% for certain aluminum alloys. It is of no great surprise that virtually all metal components for which fretting fatigue is a concern are shot peened or (lately)

laser shock peened to induce a crack-closing layer of residual compressive stress at their fretted surfaces.

Metal coatings, both hard and soft, have been employed to combat the damage of fretting fatigue. Hard metal coatings may include composites with non-metallic inclusions within a metal matrix, e.g., chromium or tungsten carbides in nickel or nickel-chrome binders. Harris (1974) reports success in limiting fretting fatigue in titanium up to 350°C using plasma-sprayed and detonation-gun-deposited WC in a cobalt matrix. Waterhouse et al. (1962) found that chromium and nickel coatings contain flaws that can act as crack initiation sites instead of inhibiting crack formation as desired. For soft metal coatings, Waterhouse (1972) mentions widespread use of cadmium in the automobile industry. Several researchers, among them Von Tein and Seibert (1974) and Johnson and Bill (1974), have found success with silver coatings. There are a great number of other workers who have looked at the effects of a multitude of coatings. Discussion of these will be truncated here, though, with the remark that in high-cycle fatigue, coatings tend to degrade or wear away rapidly. Any palliative effect they may have on fretting damage may be limited to a small percentage of the design life of a turbine blade, and they may even exacerbate the problem by forming wear particles that contribute to crack nucleation.

We adopt as reasonable the outlook of Hoeppner and Gates (1981*b*), who find that fretting fatigue is such a complicated problem involving so many variables that there will never be a universal easy fix. As with the basic tenets arising out of Nishioka and Hirakawa's work (mentioned above), though, there seem to be some reasonable findings that one would do well to consider when approaching the problem of fretting fatigue. Fundamentally, Endo and Goto (1969, 1974, 1976) have shown that fatigue cracks initiate and propagate faster under fretting conditions than they do under plain fatigue conditions. Wright (1970) recognized that high stresses due to asperity contact cause accelerated crack initiation and growth; he saw that the effect was due to more than a mere stress concentration. Bramhall (1973) further recognized that the contact stress field must be large enough to grow cracks to a size that would allow them to propagate under the bulk stresses present in a component; if it was not, no

fretting life reduction effect would be observed. Similarly, Hoeppner and Goss (1974*b*) describe a fretting fatigue threshold, i.e., they claim that there must be a minimum amount of damage caused by the local contact fields, or there will be no appreciable effect on fatigue life.

One may observe that if the literature pertaining to fretting has thus far been unable to recommend a universal palliative, it has succeeded in defining trends and commonalties for fretting situations, and consideration of these tenets has aided the present investigation considerably.

1.2.3 Material systems of interest

Extensive fretting research has been performed on a wide range of material systems. Endo and Goto (1974) have studied fretting in low carbon steels, as have others, including Dobro (1987) and Gaul (1980*a*, 1980*b*). Several researchers have examined 7075 Al alloys — cf. Alic (1979) and Adib (1993) — as well as many types of high-temperature titanium and nickel aircraft alloys; cf. Ruiz (1984) and Ravich (1990). All of these materials are used in systems susceptible to fretting damage. As early as the mid-1970s, Hoeppner and Goss (1974) were examining fretting wear in Ti-6Al-4V and Al 7075-T6 alloys. Recently, Antoniou and Radtke (1997) have investigated fretting fatigue via tests designed to induce stresses approximately equal to those experienced by a gas turbine engine blade.

The Ti-6Al-4V alloy has an $\alpha-\beta$ stabilized grain structure and is typically used for turbine blades in the relatively low-temperature early fan stages of military turbofan engines. These components have exhibited particularly problematic failure tendencies. During the course of this work, Ti-6Al-4V fretting specimens have been created for anticipated experimental use, although no experimentation has been performed in the present work.

1.3 Motivation

Motivation for this study arises from two distinct perspectives: in a broad sense it is part of an overall effort to identify and expand understanding of the mechanisms of fretting fatigue in ductile metals; specifically it addresses the problem of fretting fatigue in aircraft components. Currently the US Air Force faces serious monetary and force readiness problems because of fretting fatigue. A Scientific Advisory Board ad-hoc committee commissioned by the Air Force in 1991 found that most failures of titanium components in high-performance gas turbine engines in military jet aircraft were due to high cycle fatigue (HCF). Fretting fatigue is a form of HCF, and a particularly worrisome cause of failure in titanium blade and disk attachments. There are two primary blade materials used in a modern military aircraft gas turbine engine: titanium alloys and nickel-based superalloys. It is necessary to use nickel-based superalloys in the later, high-temperature stages of the engine; in fact these are the only materials with suitable strengths at the high temperatures realized inside an engine. Ambient temperatures are in fact above the melting point of even these alloys, but airflow across the blades and through intricate internal cooling channels allow these components to operate without melting. However, in those parts of the engine, such as the fan and early compressor stages, where ambient temperatures are not as high, titanium alloys are favored for their superior strength-to-weight ratios (Antoniou and Radtke 1997). A drawback of using these alloys is that they are particularly susceptible to fatigue life reduction due to fretting. Theoretical and analytical work presented here address fretting fatigue issues in these components.

Additionally, fretting fatigue is a critical concern in aircraft structures, occurring between all rivets and the plates which they connect, as well as any components attached via a nominally tight fit. One of the most common aircraft structural alloys is 7075 aluminum. Conveniently, the author and coworkers have used this material system for verification and refinement of the experimental apparatus developed in the current work. It is a relatively inexpensive alloy from which to create 'practice' specimens, but the information collected in these preliminary tests is still of some

application to practical fretting fatigue problems.

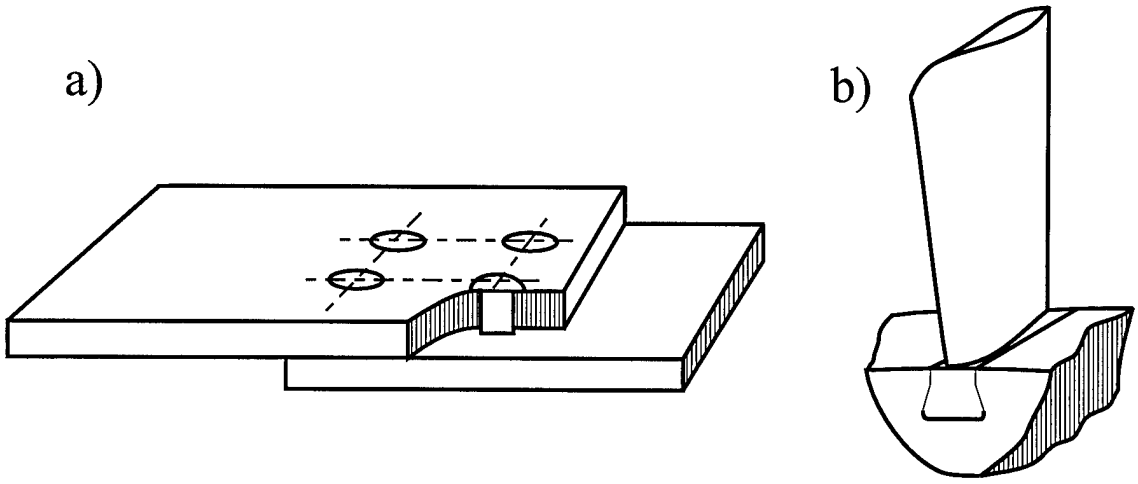

Figure 1-2: Two of the primary areas of concern for fretting fatigue in military aircraft: (a) riveted aluminum alloy structures and (b) gas turbine engine blades.

Cowles (1996) reminds us that the current design techniques used with regard to HCF effects (and hence fretting) in Air Force aircraft are based on a Goodman diagram approach. Nicholas (1996), on behalf of the US Air Force, points out that because HCF damage mechanisms in general and fretting fatigue in particular are so sensitive to surface conditions and strongly interact with other damage modes, the Goodman diagram approach as currently practiced is too empirical to be widely applied to HCF with a good degree of success. The Air Force now seeks, as a replacement, a design system consisting of two phases:

1. A means of predicting crack initiation for components subjected to HCF effects only that is superior to the current Goodman diagram approach.
2. An approach, based on fracture mechanics but including HCF interaction with non-HCF damage mechanisms, that can be used to predict life and inspection intervals for the aforementioned components.

Cowles (1996) likens the current state knowledge about how to design for HCF effects to creep problems of the 1950s and low cycle fatigue (LCF) concerns of the middle 1970s. Creep resistant nickel-based superalloys were the answer to the creep issue. To deal with low cycle fatigue, military gas turbine engine manufacturers developed and employed a damage tolerant approach based on fracture mechanics to

prevent unexpected LCF failure. The criteria formulated collectively became the Air Force's Engine Structural Integrity Program (ENSIP), which has all but eliminated low cycle fatigue failure in Air Force aircraft and saved hundreds of millions of dollars in maintenance and inspection costs. Whether such success in dealing with HCF concerns will be realized in spite of its apparently high degree of mechanistic complexity remains to be seen, but the outlook based on progress even to date is bright. Viable new approaches to the problem have been put forth by various investigators [c.f. Giannakopoulos et al. (1998)], and work to determine the validity of these is progressing rapidly.

While these concerns are particular to the Air Force, Hoeppner (1994) lists the following goals that he believes all researchers concerned with the problem of fretting fatigue would like to realize:

1. Physical/chemical understanding of the phenomenon and appropriate models.
2. Successful development of alleviation and prevention schemes.
3. Determination of appropriate maintenance, inspection, and replacement intervals.
4. Development of models of the various stages of fretting fatigue which permit application of holistic damage tolerance concepts.
5. Standardization of test practices.

It is with a mind to improve the overall understanding of fretting fatigue (which is also a critical HCF damage mechanism as identified by the US Air Force) that this study is undertaken. The primary material system of choice is Ti-6Al-4V, a material used in production gas turbine engine blades and disks. A secondary material, aluminum 7075 with a T6 heat treatment, was used extensively in refinement of the experimental method. Since it is an alloy of concern in aircraft structural fretting fatigue damage, corresponding analytical and computational analyses have been performed for this material, also. Advances in basic understanding of the fretting mechanism will be useful for all engineering alloys.

This thesis is organized in the following manner: Chapter 2 describes the basic contact mechanics pertinent to this investigation of fretting, i.e. the sphere-plane contact condition. Chapter 3 describes fretting maps constructed using various failure

criteria in conjunction with a knowledge of the contact stresses produced during fretting conditions. Chapter 4 describes a computational approach to the problem of fretting fatigue that utilizes a finite element model. Chapter 5 describes the design and construction of an experimental test frame for fretting fatigue tests, and Chapter 6 gives some of the results achieved with this apparatus that verify its proper operation. Chapter 7 describes how selected techniques of linear elastic fracture mechanics (LEFM) might be further applied to fretting fatigue. Chapter 8 concludes the work with suggestions for further study related to the problem of fretting fatigue in aircraft components.

Application	Location of fretting fatigue failure
Steam or gas turbine engines	• The seating of the turbine disk on drive shafts in land-based turbines • The dovetail or fir-tree section of aircraft jet engines where the blade attaches to the disk • The flanged joint between the disk/beveled gear and the drive shaft in gas turbine helicopter power transmission systems • Rotor-tooth contact area near gaps between stiffness compensation wedges in axially slotted turbogenerator rotors
Cables and ropes	• Fretting and rubbing in interwire contacts in: electric power transmission lines, cable car ropes, and marine hawsers and moorings
Structural joints	• Rivets in wing/fuselage aircraft structures • Splines and keyways in shafts and couplings • Shrink-fitted components
Bio-implant devices	• Fracture on underside of screwhead and countersink hole in base plates attached to bone • Femoral stem in total hip replacements where lesser trochometer bone is wired around femoral stem component

Table 1.1: Locations of fretting fatigue failure, after Suresh (1998).

Chapter 2

Review of Fretting Contact Mechanics

Selection of a contact condition for modeling is of critical concern in this investigation. Available options include the use of a complete or an incomplete contact geometry, as described by Hills and Nowell (1994). Complete contact produces a contact area that is independent of load, as with a flat punch on a plane (see figure 2*a*). Incomplete contact, e.g. the cylinder on a flat plate shown in figure 2*b*, produces a contact area whose size depends on the magnitude of the normal force. Although contact area is variable for incomplete contact, the contact pressure is in all places non-singular, falling continuously to zero at the edge of contact. A complete contact condition necessarily has singularities at its outside edges which are accommodated by local plasticity, and are thus more difficult to model analytically or numerically than nonsingular cases.

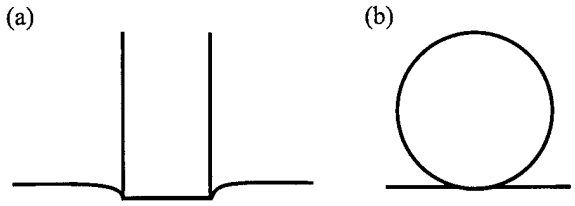

Figure 2-1: Two main types of contact: (a) complete and (b) incomplete.

In addition to the completeness of contact, conformality of contacting surfaces

is also important. The sphere-plane arrangement in Figure 2*b* is nonconformal for small normal loads, i.e., the contact area half-width (a) will be much smaller than the characteristic radius (R) of the sphere. In contrast, a sphere pushed into a complementary spherical depression with just a slightly larger radius will contact over a distance that is substantial in comparison to the radius of the sphere; this is an example of conforming contact. Nonconformal contact permits approximation of the sphere as a half-plane when calculating local contact stress-strain fields.

The condition chosen for the experimental work and analysis was that of a sphere contacting a plane. This incomplete, nonconformal option has two advantages:

- The elastic fields for this contact condition are known via a closed-form analytic solution.

- Fretting contact in actual service conditions involves micro-scale asperity contact rather than contact of ideally flat or round components; at a small size scale, sphere-on-plane contact is a reasonable model of this asperity contact.

This chapter describes sphere-on-plane contact and the elastic fields beneath the contacting surfaces as previously derived.

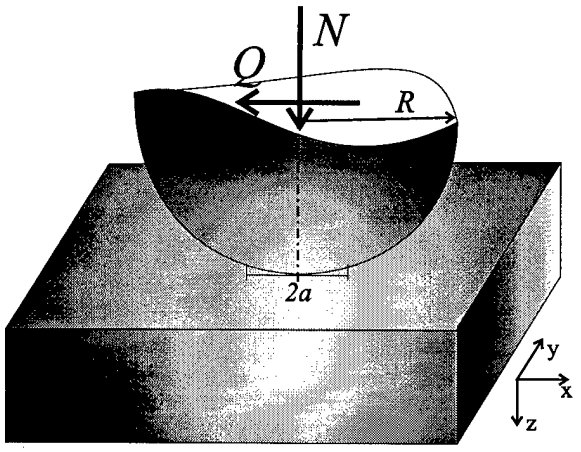

Figure 2-2: Sphere-plane contact, coordinate system, and relevant parameters.

2.1 Hertzian contact problem

Hertz (1882) analyzed the problem of frictionless normal contact between two spheres well over a century ago while he was studying under Helmholtz. Some optics experiments he conducted gave him a curiosity to know how glass lenses deform when they contact one another and led him to the solution, which he achieved entirely over his Christmas vacation when he was 23 years of age. Huber (1904) first solved for the stress fields beneath the surfaces of contacting spheres. Mindlin (1949) considered the problem in the case of sliding — where friction is a concern — and later, with Deresiewicz (1953), discussed the ramifications of changing normal and tangential forces during contact. For a sphere contacting a plane without friction, Hertz' theory predicts a circular contact surface of radius

$$a = \sqrt[3]{KNR} \tag{2.1}$$

where N is the normal force, R is the radius of the sphere[1], and $K = \frac{3(1-\nu^2)}{4E}$;[2] ν and E are Poisson's ratio and Young's modulus, respectively. Points on both bodies distant from the contact region approach each other a distance given by

$$\alpha = 2\left[\frac{KN}{R^{\frac{1}{2}}}\right]^{\frac{2}{3}} \tag{2.2}$$

and the normal tractions on the contact surface are

$$N = \frac{3N}{2\pi a^3}\sqrt{(a^2-\rho^2)} \tag{2.3}$$

where ρ is the radial distance from the center of contact. The maximum contact pressure is given by

$$p_{\max} = \frac{3N}{2\pi a^2} \tag{2.4}$$

Thus $p_{\max}$ incorporates the material properties, contact geometry, and loading conditions for sphere-plane contact into a single convenient parameter. The parameters

[1]The relation in Eqn. 2.1 is for two spheres with identical radii. For the case of a sphere on a plane, let $\frac{1}{R_{eff}} = \frac{1}{R_{sphere}} + \frac{1}{\infty}$; then $R = R_{eff} = R_{sphere}$.

[2]Similarly, Hertz' relations assumed that both spheres were of the same material. For the case of two different materials, $K = K_{eff} = \frac{3}{4}\left[\frac{1-\nu_1^2}{E_1} + \frac{1-\nu_2^2}{E_2}\right]$

a and $p_{\max}$ are particularly useful for nondimensionalizing length and stress values, respectively, in this investigation.

2.2 Sphere sliding elastically on a plane

The problem considered here necessitates consideration of friction. For sliding contact, the Amonton-Coulomb law relates tangential tractions (q) and normal pressure (p):

$$\frac{|q|}{p} = \frac{|Q|}{N} = \mu, \tag{2.5}$$

where Q is tangential force and μ is the coefficient of kinetic friction (hereafter in this work called the coefficient of friction). The friction force acts to oppose tangential motion.

Cattaneo (1938) and Mindlin (1949) solved the case of contacting spheres subjected to a tangential force following normal contact. If, after normal indentation, a tangential force is applied to the indenter and monotonically increased from zero, solution of the subsequent mixed boundary value problem (normal traction and tangential displacement on the contact surface are given; three components of traction are zero on the rest of the surface) requires that slip begin at the outside edges of contact. Without slip, infinite tractions are required to meet the boundary conditions, a physical impossibility for non-adhering materials. The radial symmetry of shear tractions (τ) predict that the slip associated with accommodation of tangential tractions will occur over an annulus. Shear tractions on the annulus of slip are taken to be $\tau = \mu\sigma$[3] with the same direction as the tangential force. Symmetry also dictates that the tangential component of displacement is constant on the region where no slip occurs (the 'stick zone'). A second mixed boundary value problem (now with tangential displacement and normal traction defined on the stick zone and all tractions given in the slip zone and remainder of the sphere) results. A solution of this

[3] σ denotes surface normal tractions.

problem gives the inner radius of the annulus of slip (c):

$$c = a\left(1 - \frac{Q}{\mu N}\right)^{\frac{1}{3}} \tag{2.6}$$

(The outer radius is given by a, the contact radius.) Shear tractions on the contact surface are distributed as

$$q = \frac{3\mu N}{2\pi a^3}\left(a^2 - \rho^2\right)^{\frac{1}{2}} = \frac{p_0}{a}\left(a^2 - \rho^2\right)^{\frac{1}{2}}, c \leqslant \rho \leqslant a \tag{2.7a}$$

$$q = \frac{p_0}{a}\left[\left(a^2 - \rho^2\right)^{\frac{1}{2}} - \left(c^2 - \rho^2\right)^{\frac{1}{2}}\right], \rho \leqslant c \tag{2.7b}$$

Points distant from the stick zone have relative displacements (δ) given by

$$\delta = \frac{3(2-\nu)\mu N}{16Ga}\left(1 - \frac{c^2}{a^2}\right) \tag{2.8a}$$

$$= \frac{3(2-\nu)\mu N}{16Ga}\left[1 - \left(1 - \frac{Q}{\mu N}\right)^{\frac{2}{3}}\right] \tag{2.8b}$$

Tangential tractions and the evolution of tangential load with increasing relative displacement are shown in Figure 2-3. As the shear force (Q) approaches μN, its maximum value, the inner radius of the slip zone approaches the center of contact. When $Q = \mu N$, the stick zone disappears and the displacements of distant points is indeterminate, as global sliding also coincides with this situation. The maximum relative displacement between the two spheres prior to sliding is then

$$\delta = \frac{3(2-\nu)\mu N}{16Ga} \tag{2.8c}$$

If a tangential force greater than zero but below the maximum value of μN has been applied to the sphere and this force is decreased, the tangential tractions on the the slip annulus are now everywhere opposite in sense to the initial tractions. Solving a boundary value problem analogous to that of the initial loading problem reveals that slip in the opposite direction begins at the contact perimeter a and penetrates to an inner radius b in the interval $c < b < a$. As before, tangential tractions on the slip annulus are $\mu\sigma$, but in the opposite direction of the initial loading tractions. Therefore, the change in tangential traction on the slip annulus upon loading in the

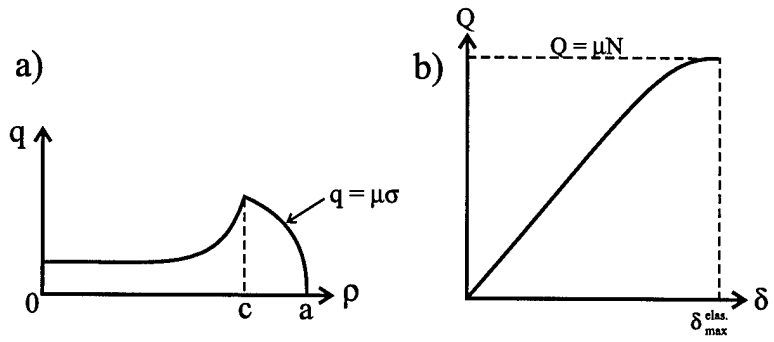

Figure 2-3: a) Tangential tractions on the contact zone. Outside of the stick zone ($c \leqslant \rho \leqslant a$), q is equal to the product of μ and the surface normal tractions (σ), which fall smoothly to zero at the edge of contact. b) The evolution of tangential load (Q) with increasing sliding displacement for fully elastic loading. At $\delta_{\max}^{\text{elas.}}$, $Q = \mu N$, the maximum attainable tangential force, and global sliding commences. After Mindlin and Deresiewicz (1953).

opposite direction is $-2\mu\sigma$. No more slip may occur than that experienced upon initial loading, so from a symmetry argument, the slip annulus experiences tangential displacement as a rigid body.

Another boundary value problem, this one similar to the second one encountered on initial tangential loading, now presents itself. The change in tangential tractions is analogous to that found for initial loading:

$$\Delta q = -\frac{p_0}{a}\left(a^2 - \rho^2\right)^{\frac{1}{2}}, b \leqslant \rho \leqslant a \tag{2.9a}$$

$$q = -\frac{p_0}{a}\left[\left(a^2 - \rho^2\right)^{\frac{1}{2}} - \left(b^2 - \rho^2\right)^{\frac{1}{2}}\right], \rho \leqslant b \tag{2.9b}$$

This change is shown by the curve a–A'–B' in Figure 2-4.

Resultant tractions for a reduction of Q are obtained by adding Eqs. 2.7 and Eqs. 2.9 to obtain

$$q = -\frac{p_0}{a}\left(a^2 - \rho^2\right)^{\frac{1}{2}}, b \leqslant \rho \leqslant a \tag{2.10a}$$

$$q = -\frac{p_0}{a}\left[\left(a^2 - \rho^2\right)^{\frac{1}{2}} - 2\left(b^2 - \rho^2\right)^{\frac{1}{2}}\right], c \leqslant \rho \leqslant b \tag{2.10b}$$

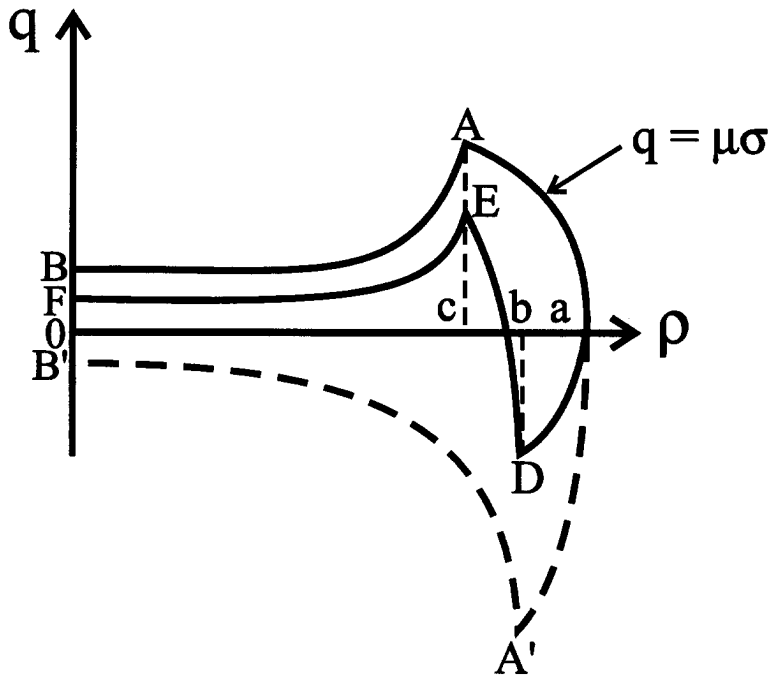

Figure 2-4: Tangential tractions on the contact zone. In this figure are represented the tractions and change in tractions for a load reversal, which are described in the pertinent text. After Mindlin and Deresiewicz (1953).

$$q = -\frac{p_0}{a}\left[\left(a^2-\rho^2\right)^{\frac{1}{2}} - 2\left(b^2-\rho^2\right)^{\frac{1}{2}} + \left(c^2-\rho^2\right)^{\frac{1}{2}}\right], \rho \leqslant c. \tag{2.10c}$$

These are shown in Figure 2-4 by curve a–D–E–F, the sum of a–A–B and a–A'–B'.

The equilibrium condition

$$Q = \int_0^{2\pi}\int_0^a q\rho\, d\rho\, d\theta \tag{2.11}$$

yields

$$Q = \frac{\mu N}{a^3}\left(a^3-c^3\right) - \frac{2\mu N}{a^3}\left(a^3-b^3\right) \tag{2.12}$$

after insertion of Eqs. 2.10.

The first term on the right of Eq. 2.12 is the initial tangential force, thus the second term is the unloading tangential force (Q^*), and the 'counterslip' annulus is defined by

$$b = a\left(1 - \frac{Q^*-Q}{2\mu N}\right)^{\frac{1}{3}}. \tag{2.13}$$

If $Q = Q^*$ (i.e., fully reversed loading), $b = c$ and the counterslip has penetrated the same radial distance as the initial slip. The tractions are identical in magnitude to those arising from force Q, but opposite in sense. This situation is elastically equivalent to the loading case where Q is never applied, only Q^*. If $Q^* = \mu N$, global sliding in the opposite direction commences.

Displacement of distant points relative to the surface of the stick zone is found by a superposition process similar to that used to determine tangential tractions upon unloading. It is analagous to Eqs. 2.8 (the displacement of adhered points for loading):

$$\delta = \frac{3(2-\nu)\mu N}{16Ga}\left(2\frac{b^2}{a^2} - \frac{c^2}{a^2} - 1\right) \tag{2.14a}$$

$$= \frac{3(2-\nu)\mu N}{16Ga}\left[2\left(1 - \frac{Q^* - Q}{2\mu N}\right)^{\frac{2}{3}} - \left(1 - \frac{Q^*}{\mu N}\right)^{\frac{2}{3}} - 1\right]. \tag{2.14b}$$

The compliance $\left(\frac{\mathrm{d}\delta}{\mathrm{d}Q}\right)$ upon unloading is

$$\frac{\mathrm{d}\delta}{\mathrm{d}Q} = \frac{2-\nu}{8Ga}\left(1 - \frac{Q^* - Q}{2\mu N}\right)^{-\frac{1}{3}}. \tag{2.15}$$

Although it was not given before, the initial compliance upon loading is identical to Eq. 2.15 for initial unloading, i.e. $Q = Q^*$. This load reversal compliance is of importance in calculating the relative displacement of contacting points at the surface, as described in Section 5.5.

Upon a second and all subsequent load reversals, the behavior of tractions and displacements follows that of the first unloading, and a closed-loop load-displacement curve results for cyclic tangential loading oscillating between $\pm Q^*$. The load-displacement curve for initial loading continuing into fully reversed cyclic loading is given in Figure 2-5.

2.3 Limitations of the analysis

The following qualifications apply to the above discussion of sphere-plane contact:

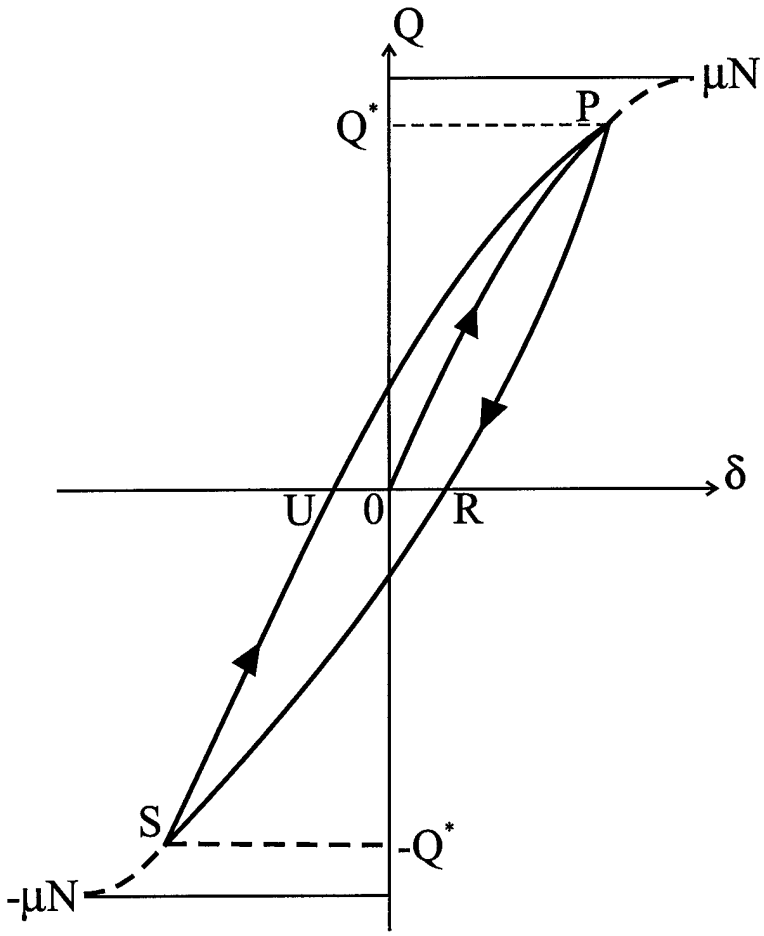

Figure 2-5: Load-displacement curve for fully reversed cyclic tangential loading. Following initial loading (path O–P), a closed-loop curve forms for the first and all subsequent load reversals (path P–R–S–U–P). After Mindlin and Deresiewicz (1953).

→ The analysis is strictly valid for a sphere-plane combination whose materials have no elastic mismatch.

→ If there is an elastic mismatch, the analysis is strictly valid for incompressible materials, i.e. those materials for which $\nu = 0.5$, if the equivalent Young's modulus (E^*) is used.

→ For the case of elastic mismatch and $\mu \neq 0.5$, the actual solution for sliding contact becomes equivalent to the Mindlin solution after one full fretting cycle (two reversals of load). The discussion then applies to all but the first fretting cycle, which is generally unimportant in relation to the number of fretting cycles

applied in HCF.

2.4 Contact stresses

Hamilton (1983) has derived a closed form solution for all elastic stress fields associated with spheres in contact and subject to tangential tractions (a subset of this solution includes the solution for sphere-plane contact). The reader is encouraged to review this solution as well as Hamilton and Goodman's (1966) preliminary solution to the same problem that left the stress fields in implicit forms involving imaginary parts of complex expressions. Neither the approach nor the final solutions are reproduced directly here, but Hamilton's expressions are an integral part of the algorithm used to construct the fretting maps described in Chapter 3.

The reader with in-depth interest should see Johnson's (1985) authoritative contact mechanics text and Hills' and Nowell's (1994) tome on the mechanics of fretting fatigue.

Chapter 3

Construction of New Fretting Failure Maps

3.1 Introduction

Vingsbo and Söderberg (1988) are among the first researchers to describe *fretting maps.* They describe three regimes of fretting surface damage: a *complete stick* regime, a *stick-slip* regime, and a *gross slip* regime. Reduction of fatigue life is limited in the complete stick and gross slip regimes; in the former surface damage is minimal, while in the latter surface damage is extensive (it constitutes fretting wear), but material disruption and removal with each fretting cycle tend to abrade away incipient cracks before they can propagate appreciably. The maps they create describe the transition between damage regimes as a function of two variables: normal force (N) *vs.* displacement amplitude (δ), N *vs.* tangential force (Q), and frequency of vibration (f) *vs.* δ. These maps are compared to then available experimental data, verifying expected general trends. One of these trends is a decreasing fatigue life up to a certain δ (approximately equal to the gross sliding displacement) with an increase after this is value is exceeded, observed by both Gaul and Duquette (1980*a*) and Nishioka and Hirakawa (1969*a*).

While knowledge of the particular damage regime into which a fretting loading condition falls is important, this information is not directly useful for life prediction.

The fretting maps created for this study are a design tool for fatigue life prediction of components subjected to fretting loads. They may more accurately be termed *fretting failure maps*. For the purposes of this work, fretting maps are constructed exclusively from information contained in the local elastic fields associated with fretting contact. The scope of fretting contact considered remains limited to sphere-plane contact, for which all elastic fields are known analytically after their derivation by Hamilton (1983). This is the advantage of fretting maps: they may be created with low computational cost for a given contact condition.

The disadvantage is obvious as well: a tool that only incorporates elastic information must make use of some elastic failure criterion. Since fretting damage involves plasticity, the use of elastic criteria for failure prediction may seem a tenuous approach. However, other researchers have shown that for certain types of multiaxial loading, elastic criteria provide good agreement with experimentation.

3.2 Elastic criteria available

Papadopoulos et al. (1997) have reviewed the elastic failure criteria available for prediction of HCF failure. They divide the approaches into four categories:

- → critical plane approaches;
- → criteria based on stress invariants;
- → approaches based on stress averages in an elementary volume;
- → mesoscopic scale approaches incorporating the change in crystal plasticity ($\Delta\gamma^{p}$) within a single metal grain.

The context of their review is to point out how the first three types of criteria fall short in accurately predicting failure when compared to the mesoscopic scale approach developed by Dang Van (1973) and improved by Papadopoulos (1987). Of particular focus are out-of-phase bending and torsion results, for which Papadopoulos' theory is well-suited. However, the experimental data included in this work show that for

in-phase loading, the stress invariant-based modified Crossland criterion[1] is identical to the considerably more complicated Papadopoulos mesoscopic criterion. Since the modified Crossland criterion exhibits slightly better agreement with experimental data than the Sines criterion (another stress invariant approach), it emerges as the best choice from this category of failure criteria.

The modified Crossland criterion (hereafter referred to as simply the 'Crossland criterion') is

$$\sqrt{J_{2,\mathrm{a}}} + \kappa\sigma_{\mathrm{H,max}} \leqslant \lambda; \tag{3.1}$$

$J_{2,\mathrm{a}}$ is the cyclic amplitude of the second invariant of the stress deviator, $\sigma_{\mathrm{H,max}}$ is the maximum hydrostatic stress, and κ and λ are constants given, respectively, by

$$\kappa = \frac{3t_{-1}}{f_{-1}} - \sqrt{3} \tag{3.2a}$$

and

$$\lambda = t_{-1}, \tag{3.2b}$$

where t_{-1} is the material fatigue limit in fully reversed torsional loading and f_{-1} is the fatigue limit in fully reversed bending. Eq. 3.1 accounts for the independence of the torsion fatigue limit from a superimposed mean torsional load.

Aluminum alloys do not exhibit a fatigue limit *per se*; fatigue strength is given as a stress level at which failure occurs only after a very high number of cycles, often 10^8 or 10^9. The bending fatigue limits for many engineering alloys are well known and reported in many sources. For Al 7075-T6, f_{-1} is 160 MPa,[2]e.g. see Fuchs and Stephens (1980). A less commonly reported value is the torsional fatigue limit (t_{-1}). The ratio of the fully reversed torsion fatigue limit to the fully reversed bending fatigue limit for hard metals is known to lie in the range

$$\frac{1}{\sqrt{3}} \leqslant \frac{t_{-1}}{f_{-1}} \leqslant 0.8 \qquad \textit{or} \qquad 0.577 \leqslant \frac{t_{-1}}{f_{-1}} \leqslant 0.8.$$

[1]The modification is use of the square root of the second invariant of the stress amplitudes rather than simply the square root of J_2.

[2]This limit is based on 10^9 *reversals* (5×10^8 cycles) for fully reversed rotating bending.

In this work, the value is taken to be 0.65, implying that $t_{-1} = 104$ MPa. The ratio t_{-1}/f_{-1} is selected based on the work of McDiarmid (1987), who reported a value of 0.64 for a commercial aluminum alloy.

3.3 Physical basis

A particular feature of the Crossland parameter commends it to this author for use as an HCF failure criterion: its inclusion of the hydrostatic component of stress. It is commonly thought that cracks nucleate at a microscopic level via the growth of persistent slip bands (PSBs) at a free surface. Repetto and Ortiz (1997) have described a theory of crack initiation at a microscopic scale. Roughening of material begins at the intersection of the free surfaces of single metal crystals and the intersections of PSBs that extend completely through the crystal. Dislocation pair annihilation due to applied stress in the material results in climb, causing a PSB to extend. Vacancy generation accompanies annihilation, creating a higher vacancy concentration within the PSB than in the bulk material comprising the crystal. Hydrostatic stress provides a driving force for vacancy diffusion; after transport within the crystal, vacancies are aided in movement to the free surface of the slip band via short-circuit or pipe diffusion. Movement of vacancies to the free surface of a PSB causes the groove between the PSB and the free surface to deepen and sharpen, becoming a small crack after a finite number of loading cycles.

We may postulate that the kinetics of vacancy pipe diffusion along PSB boundaries would be enhanced by the hydrostatic stress component within the bulk material, effectively increasing the driving force for this short-circuit diffusion mechanism [Cottrell (1964)]. The maximum hydrostatic stress realized during a loading cycle may be indicative of the amount of vacancy diffusion and roughening that can occur during that cycle. The success of the Crossland parameter as a predictor of HCF failure may stem in part from its incorporation of a macroscopic stress invariant that affects the kinetics of crack nucleation on a microscopic level.

3.4 Fretting map creation

It is desired that the failure prediction maps be simple to create and apply to fretting loading conditions. It is a very straightforward exercise to analytically determine the stress fields beneath the spherical contact sliding on a planar substrate. The stress invariants are then easily determined. A Mathematica® (1992) program utilizing the stress solutions of Hamilton (1983) has been created for this purpose. Any set of fretting contact parameters may be accommodated, including all values of $Q/\mu N$ in the interval $0 < Q/\mu N \leqslant 1$. The program is of particular use in determining the theoretical stress conditions and contact pressure distributions for the experimentation described in Chapter 5.

The present work does not utilize the critical plane approach, average volumetric stress, or small-scale average volumetric stress approaches described by Papadopoulos et al. (1997), eschewing their much higher comparative computational complexity. A stress invariant approach does not give any indication of the orientation of fatigue cracks, it merely allows a *fail/no fail* prediction for a given loading case.

In the creation of preliminary failure prediction maps, a conservative approach is taken. It is known that the maximum fretting contact stress will arise from the case where the tangential force developed reaches its maximum value, i.e., when $Q = \mu N$. Since global sliding ensues at that point, resulting in fretting wear which as discussed previously is not as detrimental to fatigue life degradation as a stick-slip condition, the stress fields associated with service fretting contact will probably not be of such high magnitudes. There may be conditions that lead to stick-slip fretting contact where Q is less than but very close to μN; this is the most dangerous fretting contact regime, and the stress fields associated with it are conservatively estimated by taking $Q = \mu N$. For $\mu \geqslant 0.3$, the maximum von Mises stress will be found at the surface near the edge of contact for tangential loading cases.

The Mathematica code is used to calculate the stress fields beneath a sliding spherical contact. The maximum contact pressure and contact radius are normalized to unity; all stresses and lengths are normalized to these values, respectively. Using

the appropriate components of the calculated stresses, the second invariant of the stress amplitudes and hydrostatic stress are extracted from these solutions. The code scans an area at the surface of contact over a region defined by $-1.2a \leqslant y \leqslant 1.2a$ and $-1.2a \leqslant x \leqslant 1.2a$ in the plane of contact to obtain the maxima of both these values. See Section 3.5 for an explanation of why the surface need only be considered to achieve the most conservative failure estimates. Values of the left-hand side of Eq. 3.1 normalized by p_0 are a final output.

So that a maximum amount of information may be displayed on a given fretting failure map, a matrix of Crossland parameter values is generated that corresponds to the simultaneous variation of two variables of interest. These are then plotted as isocontours of normalized Crossland parameter values. For example, Figure 3-1 shows a fretting failure map based on the Crossland parameter for which the maximum contact pressure (p_0) and coefficient of friction (μ) vary simultaneously. The design engineer wishing to use this map would use the following procedure:

1. Enter the plot on the left side at $p_0 = 1$ and draw a horizontal line.

2. Draw a vertical line up from the appropriate value of the coefficient of friction.

3. Determine the normalized value of the Crossland parameter based on the intersection point of the two lines. (In the example shown in Figure 3-1, the value is ≈ 1.2.

4. Multiply the value determined in the previous step by the maximum contact pressure (Eq. 2.4) for the known contact condition to determine the Crossland parameter.

5. Compare the calculated Crossland parameter with the fatigue strength for fully reversed torsional loading. If it is greater than or equal to t_{-1}, the map predicts component failure under HCF. If the value is less than t_{-1}, no failure is predicted.

It may be immediately observed that only a single value of p_0, namely $p_0 = 1$, is utilized to find the Crossland parameter for a given contact condition when using the

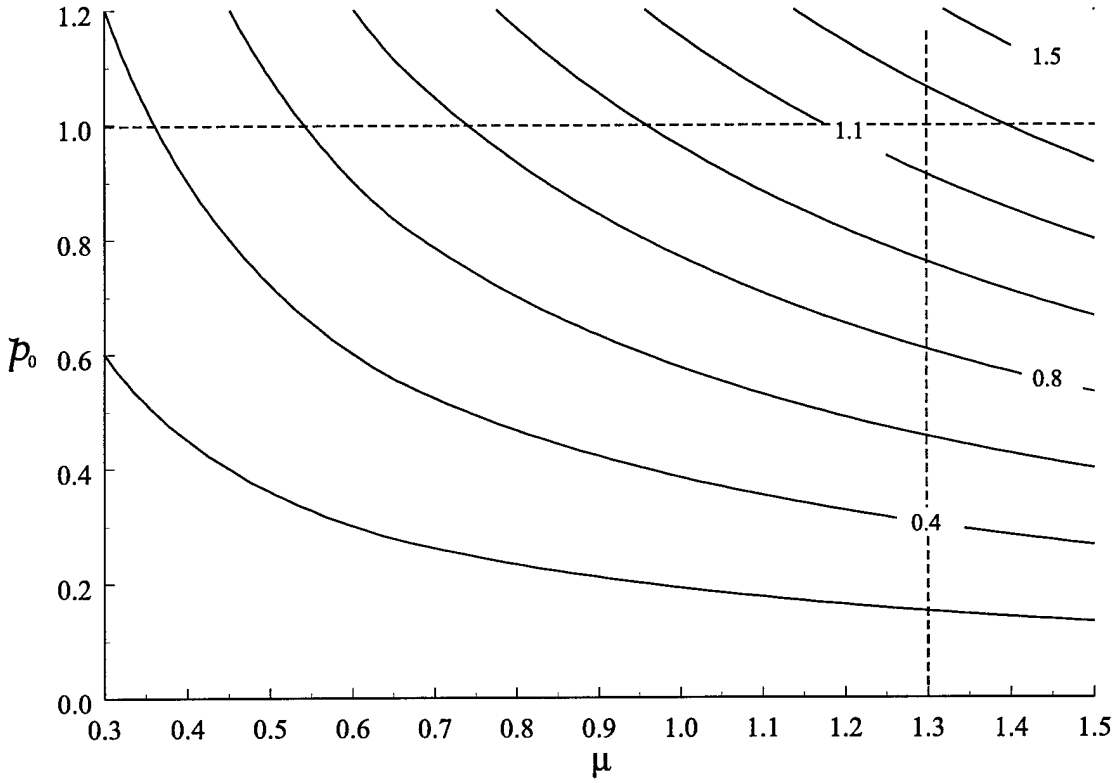

Figure 3-1: A Crossland criterion fretting map showing simultaneous variation of p_0 and μ. The plotted lines are isocontours of the Crossland parameter normalized by p_0. See text discussion for a description of how to utilize this map.

map shown in Figure 3-1. The full range of the ordinate on this map becomes useful, however, if a comparative evaluation of contact conditions is desired. A design engineer may determine that present sphere-plane loading conditions lead to a prediction of failure according to the Crossland criterion. It is a simple matter to determine the border of the *no-fail* region on the map: this is an isocontour corresponding to

$$\frac{p_0}{t_{-1}} = 1 \tag{3.3}$$

The necessary reduction of p_0 and/or μ to achieve a no-fail prediction on the map is easily determined. The value of p_0 may be altered by choice of material properties and contact geometry; adjustment of μ is achieved with lubricants or material coatings. When actual experimental values for aluminum alloys are used with this fretting map, extremely low levels of normal contact pressure must be used to reduce the resulting Crossland parameter values into the safe zone. These contact pressures are

much lower than those used in many of the experimental cases that did not result in catastrophic failure. This suggests that the approach used to create this map (in particular the fact that $Q/\mu N$ is taken to be unity — the most severe case) is overly conservative.

In Figure 3-2, a fretting map displaying isocontours of the normalized Crossland parameter is shown for varying values of both μ and applied cyclic stress amplitude, i.e., the Crossland parameter has been calculated while incorporating a range of cyclic stresses. The ordinate on this map corresponds to the amplitude of cyclic stresses applied to the substrate; the value is normalized by the maximum contact pressure (p_0). The map is utilized in a procedure similar to that described above, but the first step is to enter the map from the left side at a value corresponding to the ratio of applied cyclic stress to maximum contact pressure.

It should be noted that the isocontours of the normalized Crossland parameter in this plot are much greater than those observed in Figure 3-1. In fact, use of this failure map with any of the actual experimental conditions tested predicts failure in all cases, and by a large margin. Since many fretting tests do not exhibit failure, this suggests that this particular map is not of great value in predicting failure. We may postulate that bulk stress effects are of little importance in determining whether or not significant damage will result because of localized fretting contact stresses. Rather, bulk stress levels determine whether any cracks that might nucleate will propagate into the substrate and result in catastrophic failure, or merely self-arrest because insufficient crack extension driving force exists outside of the zone of influence of the contact stresses.

The final fretting map displayed (Figure 3-3) shows values of the normalized Crossland parameter with simultaneous variation of coefficient of friction and the ratio $Q/\mu N$. This map has proven to match most consistently the trends of experiments on aluminum alloys, and it indeed gives the closest approximation of actual contact conditions. This map demonstrates the strong dependence of the Crossland parameter on tangential tractions for fretting contact, and the same parameter seems to weigh heavily in determining the amount of damage that will result during experiments.

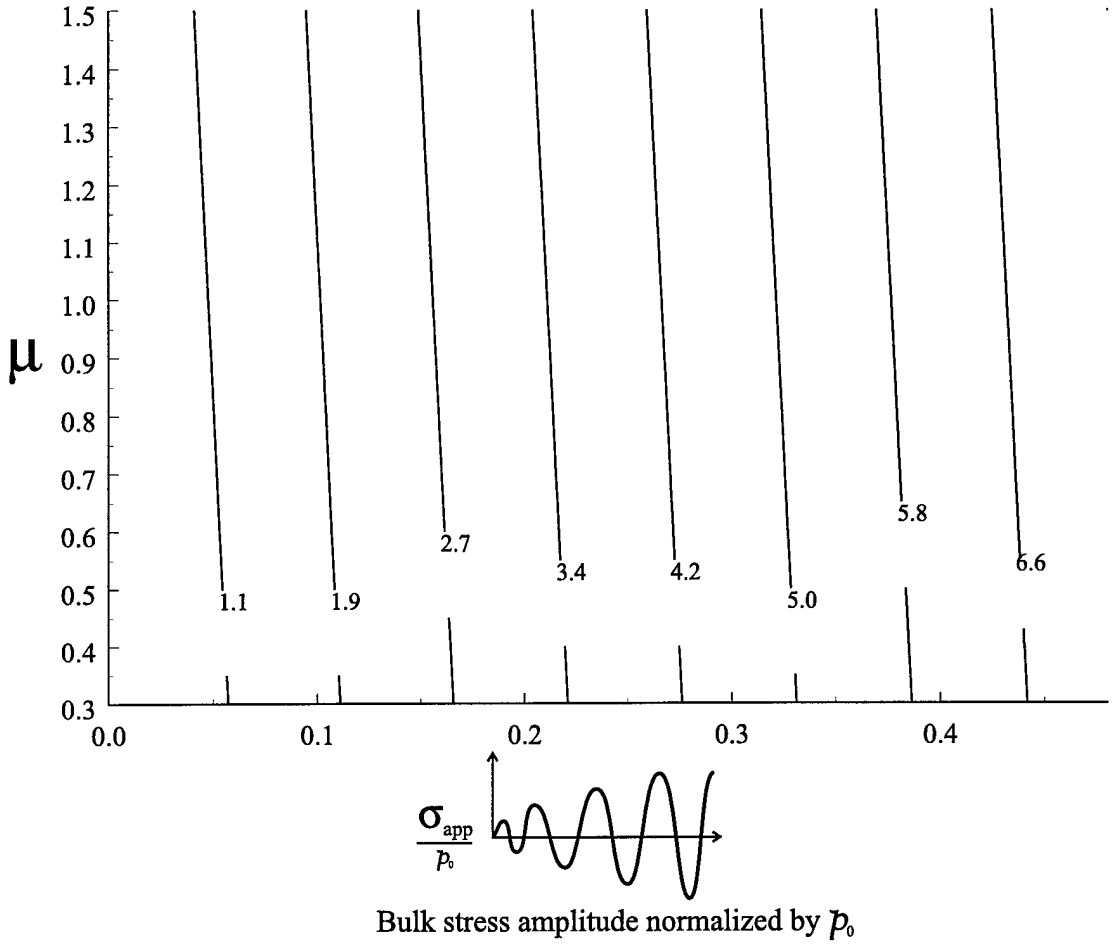

Figure 3-2: A Crossland criterion fretting map showing simultaneous variation of the amplitude of applied bulk fatigue stress (σ_{app}) and μ. Crossland parameter values calculated using bulk stress values are extremely high.

3.5 Considerations relevant to fretting failure maps

Several characteristics of the fretting failure maps described here and important considerations for their application merit mention here:

1. The maps described here are created using a stress invariant-based fatigue failure predicition criterion. Therefore they are only useful for predicting whether or not failure is likely under a given loading condition; they offer no estimate of fatigue life.

2. Maps shown in this work are created for the case of sphere-plane contact of

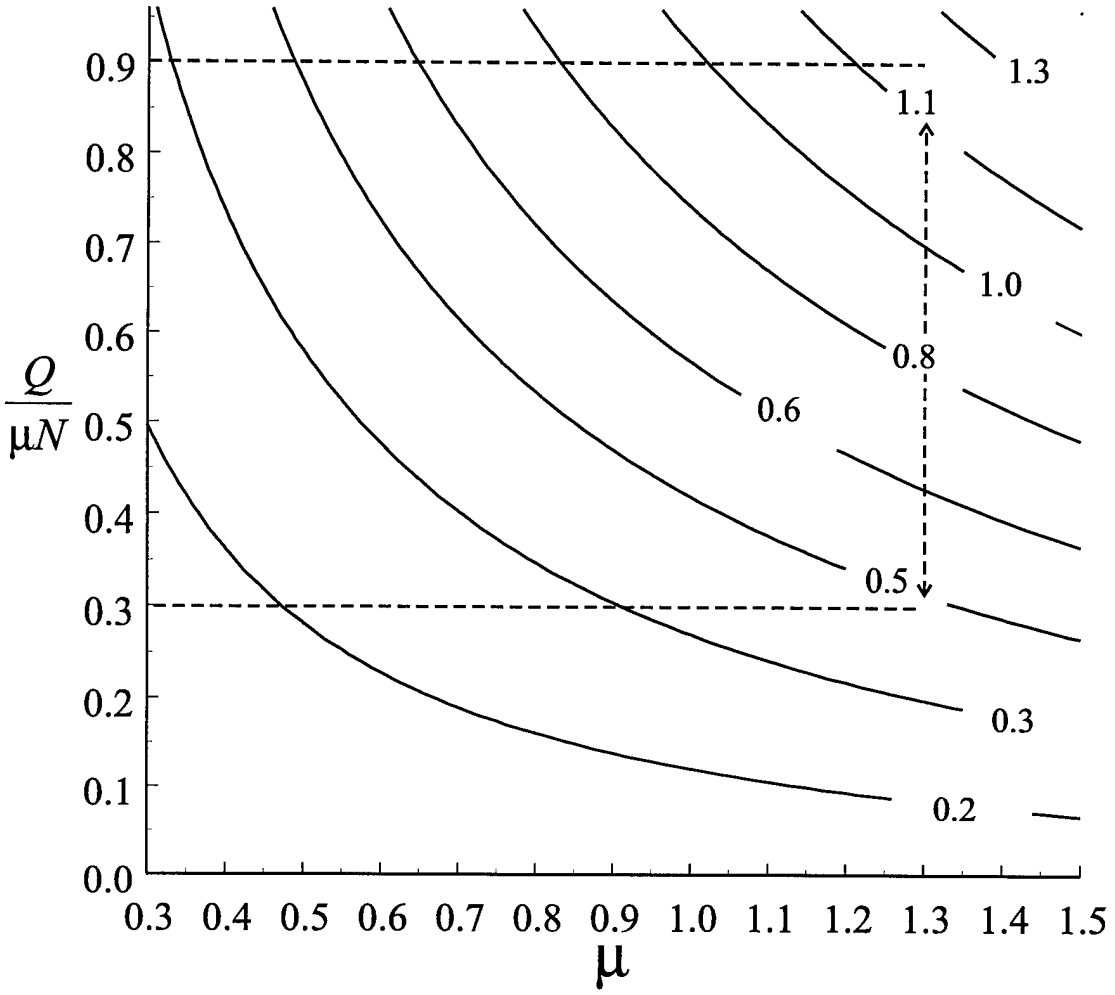

Figure 3-3: A Crossland criterion fretting map showing simultaneous variation of the ratio $Q/\mu N$ and μ. This map has demonstrated the most favorable comparison with actual experimental data.

like materials subjected to relative sliding displacements corresponding to maximum stick-slip displacement under fully elastic loading conditions ($\delta_{\max}^{\text{elas.}}$). The same conditions for validity of the Mindlin and Hamilton solutions discussed in Chapter 2 must exist for the maps to be meaningful.

3. Values of stress invariants used to calculate the Crossland parameter are those calculated for the contact surface. Figure 3-4 is a plot of normalized Crossland parameter values as they vary with depth below the contact surface (normalized by the contact radius, a) and with μ. Note that the maximum value of the

Crossland parameter for any given coefficient of friction above $\mu = 0.3$ occurs at the contact surface, just as the von Mises equivalent stress reaches a maximum value at the contact surface for stick-slip and sliding contact. Thus it is only necessary to consider the stress fields at the contact surface to obtain the most conservative estimate of the Crossland parameter.

4. In Chapter 2, sphere-plane contact is offered as a viable model for fretting fatigue on two size scales. The first is macroscopic, with contacting bodies whose size are on the order of the blade and disk in turbine engines; the second is microscopic, and contacting bodies are the size of the asperities that cover the surface of the macroscopic components. Procedures for using the maps do not change, although knowledge of loading conditions must be known at the appropriate size scale. Application of the analytical approach at a microscopic scale is more likely to be successful from a statistical viewpoint. Since there are many more contact sites when asperities are considered than there are when macroscopic contact alone is examined, there is a greater chance that the entire contact area will exhibit behavior consistent with the theoretical prediction.

The usefulness of the fretting failure map approach to predicting and designing for HCF is ultimately determined via comparison to experimental data.

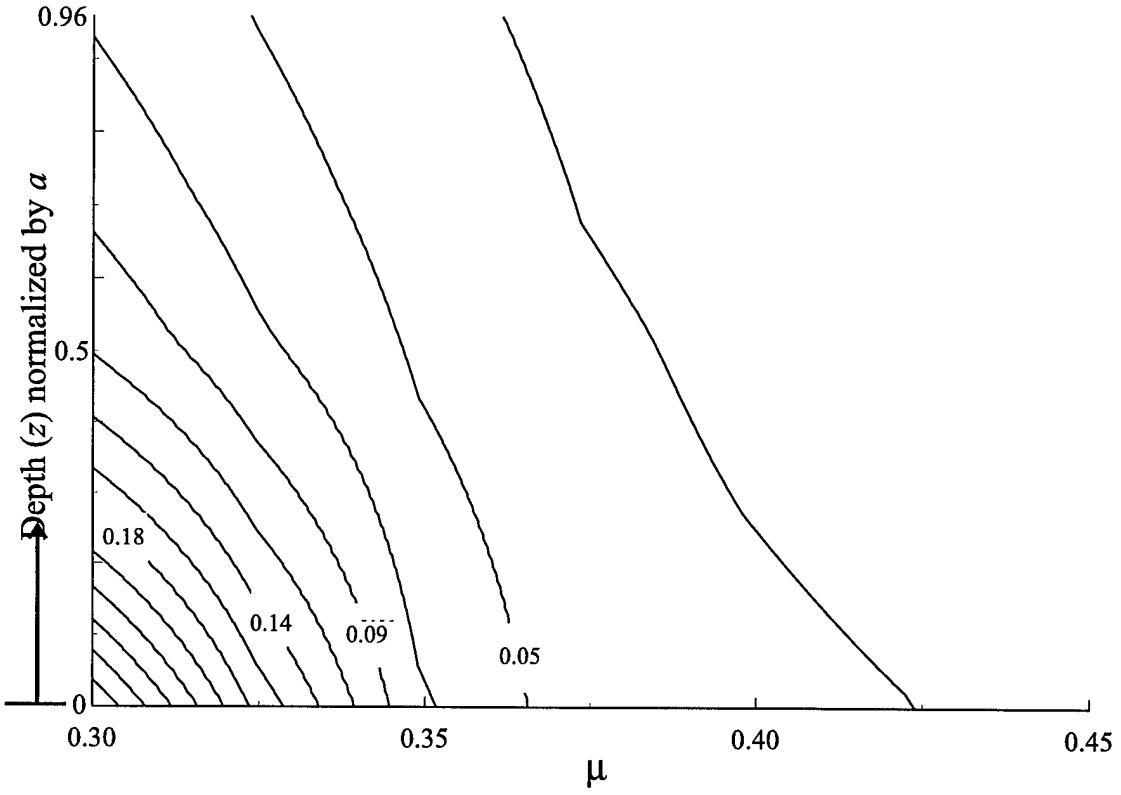

Figure 3-4: A Crossland criterion fretting map showing simultaneous variation of the amplitude of z/a and μ. The maximum Crossland parameter values are realized at the surface for all $\mu \geqslant 0.3$.

Chapter 4

Three-Dimensional Elastoplastic Finite Element Analysis of Fretting Fatigue

4.1 Motivation

Elastic fields for axisymmetric sphere-plane contact are known analytically for several cases. The works of Huber (1908), Mindlin (1949), Mindlin and Deresiewicz (1953), Deresiewicz (1957), Hamilton and Goodman (1966), and Hamilton (1983) taken together give the appropriate equations to describe the fields related to incipient full slip from a complete stick condition, partial slip, and steady-state full slip. Mindlin and Deresiewicz (1953) first described the evolution of tangential loads (Q) up to the point of sliding in closed form for elastic contact. Analytically intractable for its dual contact geometry and material property nonlinearities, though, is the evolution of stress-strain fields and Q with increasing tangential displacement for cases where plastic deformation occurs during a loading cycle. This case is of interest, occurring frequently in aircraft service conditions. Knowledge of the plastic strain accumulation behavior, for example, would permit application of a Coffin-Manson-type life prediction criterion to fretted components. The finite element computational method, as applied by Giannakopoulos and Suresh (1998) in their three-dimensional analysis of

fretting fatigue, lends itself to study of this type of plastic loading.

4.2 Three-dimensional sphere-plate model

The three-dimensional (3D) finite element model of sphere-plane contact developed by Giannakopoulos and Suresh exploits the symmetry about the principal plane containing the direction of sliding. Rather than using the ~100,000 eight-noded, trilinear elements required for acceptable resolution using a 3D mesh for a straightforward FEM simulation, they utilize Fourier expansion of the displacement fields around the center of contact. The displacement field is described by a cylindrical coordinate system (ρ,z,θ) whose origin is the center of contact. In this system, z is the vertical depth in the direction of normal indentation, ρ is the radial distance from the vertical axis, and θ is the circumferential angle measured from the direction of sliding (see Figure 4-1). For convenience in reporting some results, the ρ-θ plane is described with a Cartesian coordinate system where the x-direction is parallel to the direction the indentor slides and the y-direction is perpendicular to the x-axis. If u, v, and w are

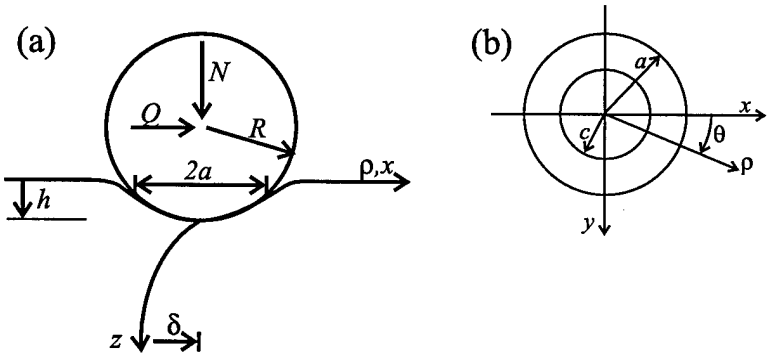

Figure 4-1: (a) A schematic and coordinate system for fretting contact. (b) A view of the same from the top, including the cylindrical coordinate system. After Giannakopoulos and Suresh (1998).

the radial, circumferential, and axial components of the displacements, the Fourier

expansion of the displacement field is given by

$$u(\rho, z, \theta) = \sum_{n=0}^{M} u_n^c(\rho, z) \cos(2n\theta), \tag{4.1a}$$

$$v(\rho, z, \theta) = \sum_{n=0}^{M} v_n^c(\rho, z) \cos(2n\theta), \tag{4.1b}$$

$$w(\rho, z, \theta) = \sum_{n=0}^{M} w_n^s(\rho, z) \cos(2n\theta), \tag{4.1c}$$

where c and s indicate the corresponding amplitudes of cosine and sinusoidal terms.

Equations (4.1) map the 3D displacement field onto a radial-axial (ρ, z) plane of reference that contains the direction of sliding; their computational advantage is that they converge rapidly. $M = 0$ corresponds to a two-dimensional analysis of axisymmetric deformation. From Jørgensen's work (1993, 1997), it is known that series expansion of $M = 2$ produces good convergence for the 3D case. The model assumes linear kinematics and small strains. In the principal plane, field variables are resolved in terms of four-noded isoparametric elements; the number of degrees of freedom per node is dependent on the choice of M. The stiffness of each ring-element is integrated using full Gaussian integration on the radial-axial (symmetry) plane. The integration in the circumferential direction uses the trapezoidal rule with six integration points and involves products of harmonic functions of θ. A fully 3D solution then results with a computational cost only slightly larger than that required for a planar, two-dimensional solution.

The substrate material is modeled as isotropic, linear elastic, with the option to introduce the associative flow rule with isotropic or kinematic strain hardening. The spherical indentor is approximated as a rigid paraboloid of revolution with radius R, where $z = r^2/(2R)$ describes the related parabola. The model can incorporate Coulomb friction with any value between $\mu \to 0$ (frictionless) and $\mu \to \infty$ (perfect stick) within each element, but in this analysis the friction coefficient is set constant on the plane of sliding. Further details of the finite element formulation are as described by Giannakopoulos and Suresh (1998). Contact conditions are achieved with displacement control of the mesh; outer mesh boundaries are moved relative to the

rigid, stationary indentor to create the same conditions that are realized in actual fretting contact.

The methodology for determining finite element model inputs is as follows: First, a desired maximum normal contact pressure ($p_{\max}$) is selected. Selection of $p_{\max}$ depends on whether the user wishes to model fully elastic contact conditions or elasto-plastic contact. Ponter et al.'s (1985) predictions for the steady-state behavior of a circular region under normal and tangential loading were consulted to determine whether loading conditions would be fully elastic or possibly involve stresses above the yield point (see Figure 4-4). A characteristic length for the mesh dimensions was selected, and a contact radius (a) was chosen such that the surface of the rigid indentor would contact no fewer than 12 nodes in the most refined mesh area upon initial normal loading. Contact with at least twelve nodes corresponds to a contact diameter that is at least half of the length of the top surface of the most refined section of the mesh. Maximum relative sliding displacements for all models are an order of magnitude smaller than contact radius, thus no portion of contact occurs outside of the most refined mesh section.

After determination of $p_{\max}$ and a, the normal load (N) is given by

$$N = \frac{2\pi a^2 p_{\max}}{3}, \tag{4.2}$$

and the radius of the sphere (R) by

$$R = \frac{a^3}{KN}, \tag{4.3}$$

with K defined as

$$K = \frac{3(1-\nu^2)}{4E},$$

as in Section 2.1. The shape of the spherical indentor is approximated in the finite element model as a rigid, axisymmetric paraboloid, described by

$$z = \frac{\rho'^2}{2R}, \tag{4.4}$$

where ρ' is a characteristic dimension equal to 24 times the length of the internodal distance of the most refined mesh section. Since this section consists of 24 elements,

ρ' is also the length of the most refined mesh section. The modeling application generates the appropriate parabola (which effectively becomes a paraboloid upon integration of the axisymmetric solution) based on the value input for z.

The finite element model utilizes a rigid, immobile indentor geometry, meaning that the substrate material is effectively 'pushed' into the indentor to simulate normal loading, and then is moved back and forth, in the opposite direction of the tangential motion of the sphere. The vertical distance which the substrate material block is displaced toward the tip of the indentor to simulate normal loading (α') is given by

$$\alpha' = \left[\frac{KN}{R^{\frac{1}{2}}}\right]^{\frac{2}{3}}. \tag{4.5}$$

This α' is one-half the α described by Eq. 2.2 to account for an indentor described as a completely rigid body that must be modeled as if it has a compliance equal to that of the substrate.

Other input parameters include the appropriate elastic constants for materials being modeled; these are given in Tables 4.1 and 4.2. For cases incorporating plasticity, the choice of isotropic or kinematic hardening is input directly, and the amount of hardening is described by linearization of the appropriate uniaxial stress-strain curve. The hardening curve may be modeled using as many linear segments as desired; for this study it was always taken to be a single continuous line.

The utility of this model lies in its 3D nature. Fretting contact is a 3D problem; the mechanical response of materials subjected to it arises in part because of the constraints imposed by material that *completely* surrounds the fretting zone. Any two-dimensional model neglects these constraints, and its results are of limited value. A 3D model renders all displacements determinant, whereas a 2D model does not. Figure A-1 in Appendix A shows a magnified displacement field created for a normal contact case, emphasizing the 3D form of the model.

4.3 Analysis of elastic cases

FEM analyses for fretting contact of a spherical Ti-6Al-4V indentor contacting a planar substrate of identical material were conducted for various normal loads, ball

diameters, and values of average friction coefficient. In all cases, contact conditions were chosen such that the Mises stress was everywhere well below τ_y. This includes a normal loading step as well as a subsequent tangential displacement equal to that when tangential force (Q) is equal to μP (i.e., the point where global sliding commences). Thus, the onset of plasticity was not expected, and model cases where analyzed using the FEM model with no possibility for material plastification. Average CPU time on a DEC 3000 32-bit processor for normal loading steps was on the order of 1300 s. Subsequent tangential displacements were modeled as a single displacement to the maximum displacement value. Processor time for the tangential displacement step was slightly less, on the order of 900 s. Since the model is fully elastic, displacement to the maximum distance in the opposite direction will yield fields that are a reflection about the $z-y$ plane of those obtained for the complementary sliding direction. Therefore only one quarter of a complete fretting cycle must be analyzed to fully know the fields associated with fully elastic contact conditions.

Figure 4-2 is a picture of the von Mises equivalent stresses[1] in a Ti-6Al-4V substrate beneath a 12.7 mm diameter spherical indentor of the same material. The normal load (N) applied is 10 N. Notice that the maximum von Mises stress is beneath the contact surface at a depth $z \approx \frac{1}{2}a$; this is true for all materials with $\nu = 0.3$. For the Ti alloy shown here, ν is taken to be 0.321. The von Mises stress serves as an indicator of imminent plastic yielding. In Figure 4-2, the maximum von Mises stress is 710 MPa, well below the material yield stress of 925 MPa. Figure 4-3 shows the same modeled case following tangential displacement to the maximum distance attainable before global sliding commences under pure elastic loading ($\delta_{\max}^{\text{elas.}}$). The maximum von Mises stress increases in magnitude, and shifts up and toward the back edge of contact. The coefficient of friction (μ) is fixed as 0.7, dictating that the maximum von Mises stress will be at the surface, as it is for all $\mu > 0.3$.

[1]The von Mises equivalent stress ($\bar{\sigma}$) is given by

$$\bar{\sigma} = \sqrt{\frac{1}{2}\left[(\sigma_{22}-\sigma_{33})^2 + (\sigma_{33}-\sigma_{11})^2 + (\sigma_{11}-\sigma_{22})^2\right] + 3\sigma_{23}^2 + 3\sigma_{31}^2 + 3\sigma_{12}^2}$$

in terms of all components of stress and by $\bar{\sigma} = \sqrt{\frac{3}{2}s_{ij}s_{ij}}$ in terms of the stress deviators.

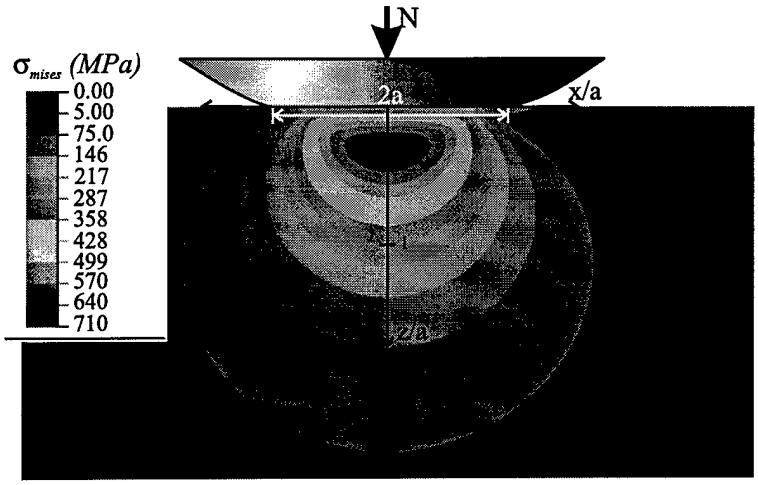

Figure 4-2: Von Mises equivalent stress ($\bar{\sigma}$) for a Ti-6Al-4V sphere, $\phi = 12.7$ mm, contacting a plane of the same material with a normal load of 10 N. The maximum von Mises stress is below the surface at a depth $z \approx \frac{1}{2}a$.

In addition to a simple elastic analysis of fretting contact in the Ti-6Al-4V system, an elementary method of modeling residual stresses present prior to fretting contact is available. Residual stresses of $-0.95\sigma_y$ (a typical value following shot or laser peening), $-0.5\sigma_y$, $0.5\sigma_y$, and $0.95\sigma_y$ were imposed by displacement of mesh boundaries. Normal indentation and subsequent fretting displacement were then simulated by adjusting model inputs in the usual way described above. Because the accumulation of plastic strains in fretting contact is influenced mainly by the local contact fields, the imposition of residual stress in the bulk substrate does not significantly alter this quantity for a given loading condition. As mentioned in Chapter 3, bulk stresses become of importance in determining whether a crack that has initiated will propagate or self-arrest, and compressive residual peening stresses are beneficial because they reduce the magnitude of crack-tip opening (tensile) stresses.

4.4 Analysis of plasticity

To more fully exploit the capabilities of the finite element model, cases where plastic yielding and flow occur are also considered. Giannakopoulos and Suresh (1997) have

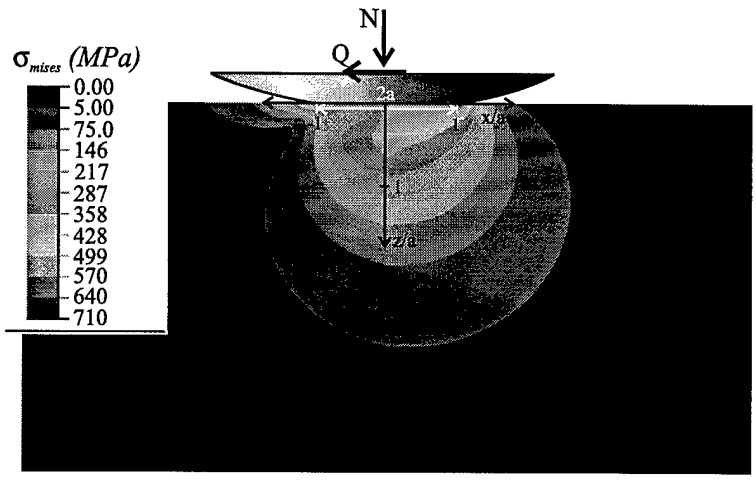

Figure 4-3: Von Mises equivalent stress ($\bar{\sigma}$) for the loading case in Fig. 4-2; the sphere has been slid to the maximum elastic sliding displacement, with $\mu = 0.7$. The maximum von Mises stress is located at the trailing edge of contact.

analyzed plastic cases with the model described here for frictionless normal contact and fretting contact with a coefficient of friction (μ) equal to 0.7. They found that the elastic shakedown limit for frictionless normal loading and unloading was

$$\frac{3P}{2\pi a^2 \tau_y} = \frac{p_{\max}}{\tau_y} = 4.5. \tag{4.6a}$$

Similarly, they found the elastic shakedown limit for fretting with $\mu = 0.7$ to be

$$\frac{p_{\max}}{\tau_y} = 1.4, \tag{4.6b}$$

and the shakedown limit against incremental growth of surface strains (so-called 'ratchetting') to be

$$\frac{p_{\max}}{\tau_y} = 1.5. \tag{4.6c}$$

Their findings agree with Ponter et al.'s (1985) theoretical upper limit of

$$\frac{p_{\max}}{\tau_y} = 4.675 \tag{4.7a}$$

for elastic shakedown and the upper bound for incremental surface strain growth of

$$\frac{p_{\max}}{\tau_y} = \frac{1}{\mu} \tag{4.7b}$$

Material Property	Value(s)
σ_y	925 MPa
E	115.7 GPa
G	43.8 GPa
ν	0.321
μ	0.3, 0.5, and 0.7

Table 4.1: Material properties of interest for Ti-6Al-4V. σ_y is tensile yield strength, E is Young's modulus, G is the shear modulus, ν is Poisson's ratio, and μ is the kinetic friction coefficient.

for $\mu > 0.3$. The theoretical predictions of Ponter et al. are summarized in Figure 4-4. Shown are the upper bound to elastic shakedown limit against alternating plasticity, the upper bound to plastic shakedown limit against incremental growth, the upper bound to elastic shakedown limit against incremental growth of surface strain, the elastic limit, and the lower bound to elastic shakedown limit.

For stick-slip conditions in elastic contact, Mindlin and Deresiewicz (1953) plot the development of tangential load (Q) with increasing tangential displacement (δ), as shown in figure 4-5. Referring to Figure 4-5(a), notice that global sliding commences at a maximum displacement, δ_{slide}. Figure 4-5(a) is for elastic loading, however. The value of δ_{slide} increases when material beneath the contact plastifies during the loading, as shown in Figure 4-5(b). Equivalently, tangential load (Q) develops more slowly over a given sliding displacement.

4.4.1 Evolution of tangential load

Giannakopoulos and Suresh (1997) have demonstrated using their finite element method approach how plasticity alters the evolution of T under elastoplastic loading conditions for one particular case of fully reversed sliding between a sphere and plane. Figure 4-6 compares the evolution of T as it changes with relative sliding distance

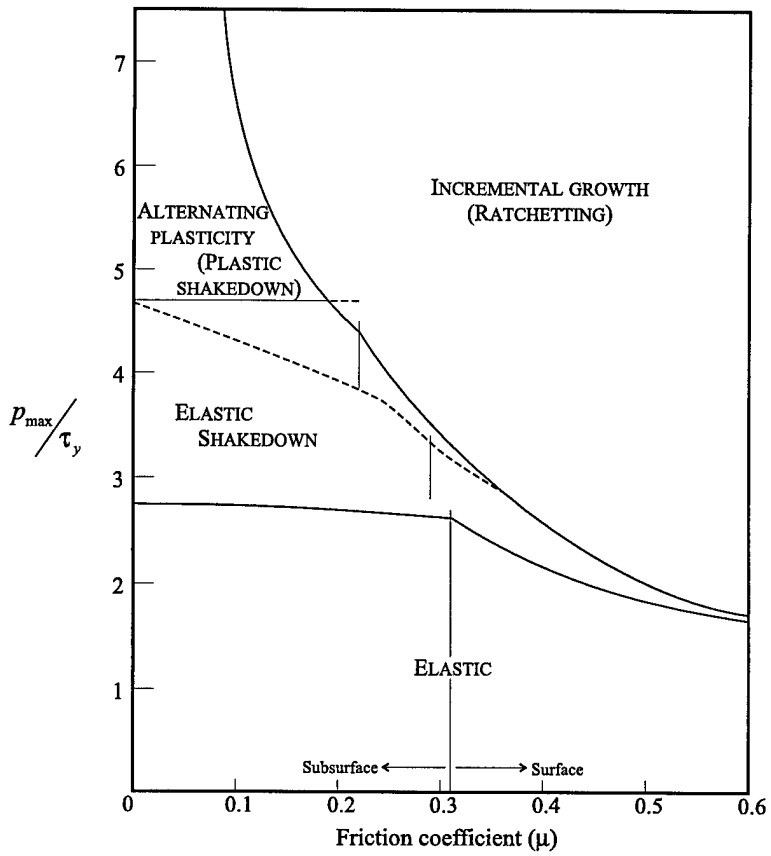

Figure 4-4: Steady-state behavior of a circular region under various tangential and normal loads. After Ponter et al. (1985).

for an elastoplastic loading case and a case using the same loading conditions but without the possibility of plasticity. This 'artificial' elastic case provides a lower limit for the amount of relative sliding that must occur before global sliding commences. The presence of plasticity, though, in particular unconstrained plastic flow at the surface of contacting bodies, effectively increases the tangential compliance ($\mathrm{d}Q/\mathrm{d}\delta$) of the system. More relative displacement may occur before development of the maximum (i.e., global sliding) tangential force because of this plastic compliance. Further, plasticity produces the hysteresis response shown in Figure 4-6. (The loop stabilizes upon the third reversal of the tangential load.) It is analytically difficult to know exactly how much additional sliding is possible because of plasticity. It is a function of the material's plastic hardenability and how much plastic flow occurs as surface plasticity, unconstrained by surrounding elastic material.

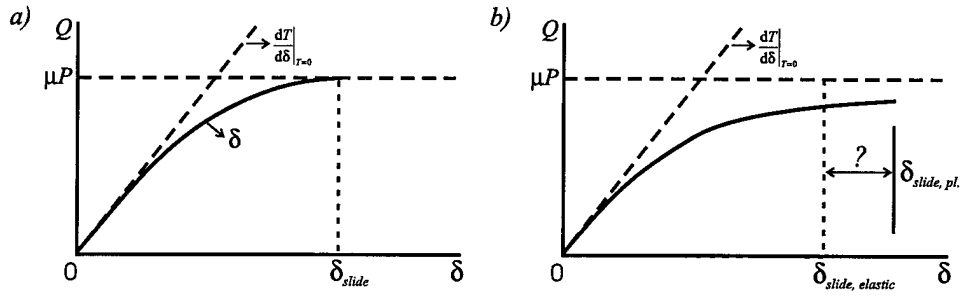

Figure 4-5: The change in maximum relative sliding displacement between a sphere and plane (without global sliding) for elastic loading and conditions of plasticity. (a) shows that Q becomes equal to μP at a particular displacement δ_{slide} and global sliding commences. In (b), plasticity allows relative motion greater in magnitude than the displacement δ_{slide} shown in (a) to occur before global sliding occurs.

The finite element model has been used to explore this phenomenon in more detail. The material system investigated is a high-strength aluminum alloy typically used as a structural material in military aircraft: Al 7075-T6. Properties are listed in Table 4.2. The loading condition simulated was as follows: sphere radius (R) of 1.435 mm, normal load (N) of 1.145 N, contact radius (a) of 0.025 mm, maximum contact pressure ($p_{\max}$) of 874.7 MPa, and a relative normal displacement (α) of 0.7143 μm. The maximum contact pressure is chosen to be below the yield strength of the material; upon the initial normal loading step, minimal plasticity ensues, and it is limited to a small area beneath the contact surface. The material strain hardening[2] was initially specified to be relatively low (4.3%) and was assumed to be isotropic; the model exhibits a nearly elastic-perfectly plastic response.

After normal loading, the sphere is slid to its maximum elastic displacement, as given by Eq. 2.8c. For the initial case, where μ was taken to be 1.3 to reflect experimental values, a complete fretting cycle was modeled with 25 sliding steps, and each step in 5 increments. Five steps, each of equal tangential displacement magnitude, were programmed for sliding from the initial starting point to the maximum positive

[2]Strain hardening is defined here as the increase in yield strength for a strain of 1.0, expressed as a percentage of Young's modulus for elastic loading. In the model, yield strength increases linearly from its value at the maximum elastic limit as a function of accumulated plastic strain.

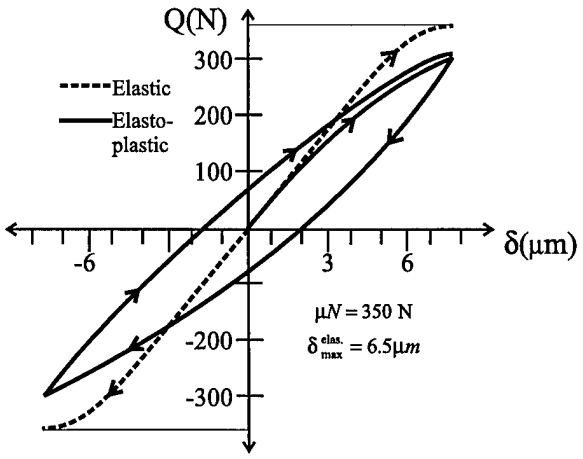

Figure 4-6: Evolution of T with relative sliding displacement for a fully reversed loading cycle of sphere-plane contact. The solid line shows the elastoplastic case, and the dashed line represents identical loading conditions, but with plasticity inhibited in the finite element model. After Giannakopoulos and Suresh (1997).

displacement, from the maximum displacement back to the initial starting point, from the starting point to the maximum negative displacement, etc. This allows the model to converge many more times within a given magnitude of sliding displacement than it did for elastic calculations, and is necessary to achieve convergence with a substantially more complex model (i.e., one that accommodates plasticity). For subsequent cases, the fretting cycle was modeled in only five steps, each again incorporating a movement to the maximum elastic sliding displacement from the starting position or *vice versa*. A higher number of increments within each step — 25 instead of only 5 — was used to ensure convergence throughout. Tangential force was monitored during the fretting cycle. For the case of $\mu = 1.3$, modeled in 25 sliding steps, the average computational time required per step was 1890 s, for a total time of 47,240 s (13.1 h) to model a single fretting cycle. For a typical case modeled in five steps, the time per step increased to an average of 6829 s, with the total time to model a complete fretting cycle decreasing to 34,150 s (9.5 h).

The only model parameter varied in this series was the coefficient of friction. As the maximum elastic sliding displacement is a function of μ, it changed with each test. In addition, the value of μN (the maximum value of Q attainable) changes for

Material Property	Value(s)
σ_y	505 MPa
E	70.3 GPa
G	26.1 GPa
ν	0.33
μ	0.4, 0.7, and 1.3

Table 4.2: Material properties of interest for Al 7075-T6. σ_y is tensile yield strength, E is Young's modulus, G is the shear modulus, ν is Poisson's ratio, and μ is the kinetic friction coefficient.

μ	$\delta_{\max}^{\text{elas.}}$ (μm)	μN
1.3	0.714	1.489
1.0	0.549	1.145
0.7	0.385	0.801
0.4	0.220	0.458

Table 4.3: Coefficient of friction and maximum sliding displacements used for elasto-plastic FEM models of fretting contact in Al 7075-T6 alloy.

each case. Values are given in Table 4.3.

Figure 4-7 shows the development of tangential force as a function of sliding displacement. For comparison the ordinate is normalized by μN; the abscissa is normalized by $\delta_{\max}^{\text{elas.}}$. As coefficient of friction increases, the initial $\mathrm{d}Q/\mathrm{d}\delta$ decreases so that a smaller portion of the maximum tangential load is developed within the first portion of the fretting cycle. Hysteresis response is more pronounced for higher friction coefficients, though, so that after completion of the full fretting cycle and returning to positive maximum displacement, the tangential force developed is significantly higher. The lower friction coefficient tests develop a greater percentage of

the maximum tangential load upon initial loading, and exhibit a small amount of hysteresis, with the tangential force-displacement curve nearly closing upon itself on returning to the maximum positive tangential displacement.

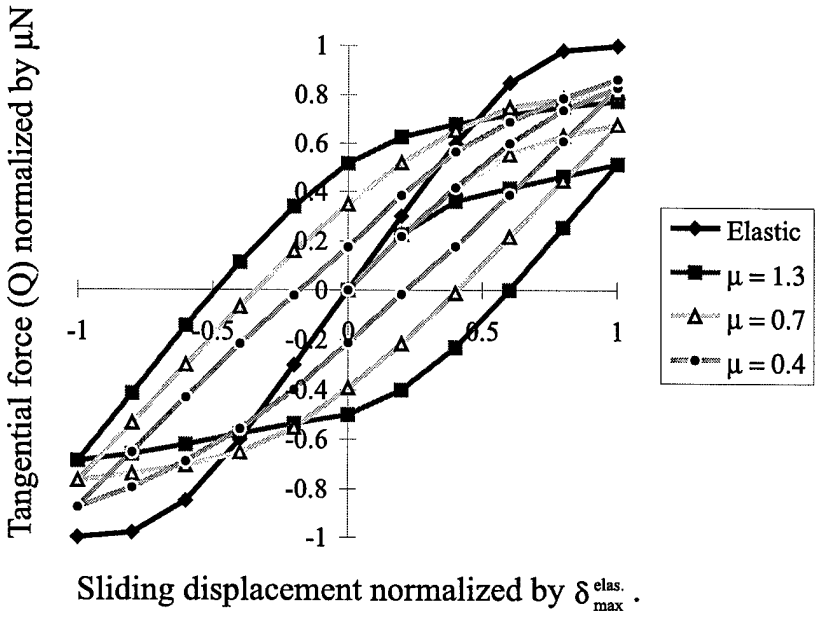

Figure 4-7: The evolution of tangential loads with sliding displacement for various coefficients of friction. The initial normal loading is identical for all cases, and strain hardening is modeled to be 4.3%.

These trends are consistent with the expected effects of plasticity as observed by Giannakopoulos and Suresh. Higher friction coefficients will lead to the development of higher contact stresses, hastening the growth of plasticity. Plastic flow increases the tangential compliance and increases the amount the sphere may be slid before global sliding occurs. In addition to the hysteresis response associated with irreversible plasticity, there is an additional effect of strain hardening that causes the final tangential force reached at maximum displacement to be higher than it was upon initial positive displacement. The finite element model permits a quantitative characterization of the increase in compliance and (with further tests) of the effects of strain hardening.

Note that in all force-displacement plots, an elastic response curve is given for reference. This is of course an imaginary reference, and a word about its nature is

in order so that it is not misleading. It is most important to note that the elastic response will not be observed in these simulations, because loading conditions are deliberately chosen to cause plasticity. Therefore, relative displacements may never be high enough to allow development of the limit tangential load, i.e., $Q = \mu N$. Indeed, the model does not have the capability to simulate an instance of global sliding. At the commencement of sliding, contact boundary conditions become ill-posed with an unbounded displacement of the mesh, and numeric instability ensues in employing the finite element method. For observation of tangential load and displacement for cases of global sliding, precise experimentation remains the only option.

The other elastic reference curve characteristic one must note is its false symmetry. In actuality, the curve shown is a set of two Mindlin curves for the development of tangential force for *initial* tangential loading; the half extending to the upper right corner of the plot corresponds to a loading in the positive sense, and the other half is for an initial loading in the opposite direction. These respective initial loadings are the Q and Q^* of Chapter 2. A more accurate idea of the expected elastic response is the one portrayed in Figure 2-5, as it is noted in Chapter 2 that compliance upon unloading is initially identical to that observed on initial loading. The reference curves are included as they are to give the reader a sense of how forces developed in fully reversed loading approach their maximum possible magnitude throughout a loading cycle.

4.4.2 Increased strain hardening

The first load-displacement curves shown in this chapter were for models incorporating a relatively low amount of strain hardening. Other simulations demonstrate the effects of increased strain hardening, which more accurately approximates an engineering alloy's response. Figure 4-8 shows load-displacement curves for the Al 7075-T6 alloy modeled previously, but now strain hardening is ~15%. It can be seen that the trends in maximum tangential load achieved for the maximum elastic displacement remain the same as before, i.e., lower friction coefficients correspond to the realization of a higher percentage of the maximum possible tangential load (because

there is less plastic compliance). However, the marked difference in Q from the first time displacement reaches the maximum positive distance to the second time has disappeared. We may postulate that a more rapidly strain hardening material reaches its steady-state response to cyclic plastic loading sooner than does an alloy without a high degree of strain hardening.

Two identical loading cycles are shown in Figure 4-8, both with $\mu = 1$. The simulations performed to produce this response incorporated different material yield strengths. The cycle which attains a higher percentage of the maximum possible tangential load has a σ_y of 505 MPa, the yield strength of Al 7075-T6; the curve for $\mu = 1.0$ that realizes a lower maximum value of Q has σ_y of 276 MPa, the yield strength of Al 6061-T6. As expected, the case where less plasticity develops, i.e. the alloy having a higher yield strength, develops a higher percentage of the maximum possible tangential load.

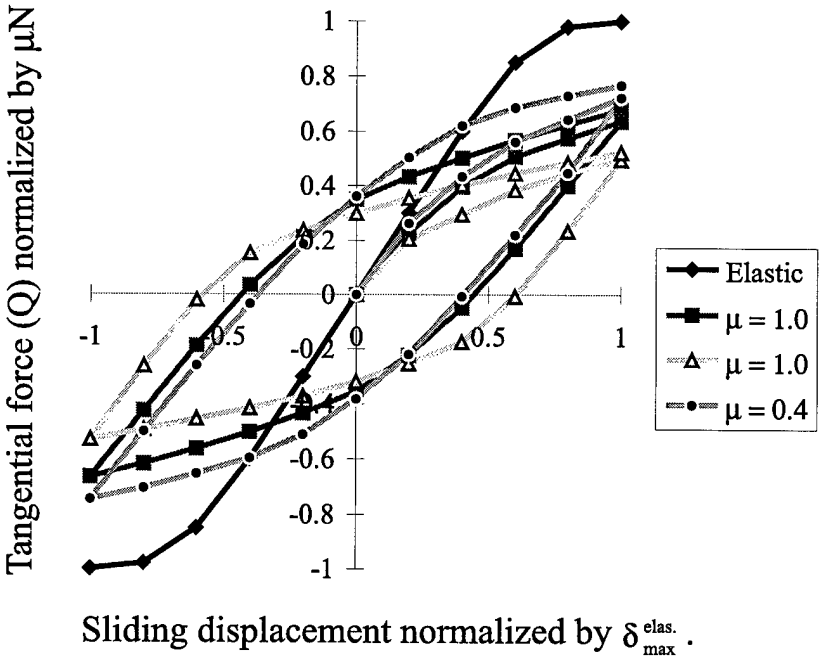

Figure 4-8: The evolution of tangential loads with sliding displacement for various coefficients of friction. The initial normal loading is identical for all cases, and strain hardening is modeled to be 15%. See related discussion.

The usefulness of predicting the increased tangential compliance due to plastic

yielding in fretting contact lies mainly in its application to experimentation. The analytic methods used to predict experimental conditions are based on fully elastic solutions, which do not account for effects of plasticity. An anticipation that tangential loads developed in fretting contact will not achieve values as high as an elastic analysis would predict — which is what the FEM analysis suggests — suggests to the experimentalist that increased relative sliding displacements are necessary to create the contact stress fields predicted by a purely elastic approach. Similarly, this indicates that the contact stress fields in service components may not be as high as an elastic analysis of an *in situ* measurement of relative sliding displacements might suggest, simply because of the increase in compliance caused by plastic yielding.

4.4.3 Accumulation of equivalent plastic strains

Knowledge of the plastic strain response of the sphere-plane system is also useful for life prediction. In particular, if the equivalent plastic strain increment ($\Delta\epsilon_{\mathrm{pl}}^{\mathrm{eq}}$) per fretting cycle is known, component life may be predicted via a Coffin-Manson (1959, 1960, 1962) type relation of the form

$$\left(\frac{\Delta\epsilon}{2}\right)_{\mathrm{pl}} = \epsilon'_{\mathrm{f}}\,(2N_f)^c, \tag{4.8}$$

where ϵ'_{f} is the fatigue ductility coefficient[3], $2N_{\mathrm{f}}$ is the number of load reversals to failure, and c is the fatigue ductility coefficient[4]. Equation 4.8 has been found to describe LCF behavior of metals. However, because it predicts failure based on the accumulation of local plasticity, the same approach may be valid for HCF situations.

The finite element model directly provides the equivalent plastic strain ($\epsilon_{\mathrm{pl}}^{\mathrm{eq}}$) accumulated at any given loading step. Figure 4-9 depicts the accumulation of equivalent plastic strains throughout a loading cycle. There are plateaus in this quantity corresponding to unloading and a reduction in magnitude of tangential force. The value returned following the final displacement step may be taken to be the plastic strain increment per loading cycle. The equation normally used for a strain-life approach

[3] ϵ'_{f} is approximately equal to ϵ_{f}, the true fracture ductility in monotonic tension.

[4] Equal to -0.5 to -0.7 for most metals.

to fatigue design,

$$\frac{\Delta\epsilon}{2} = \frac{\sigma'_f}{E}(2N_f)^b + \epsilon'_f(2N_f)^c, \tag{4.9}$$

which accounts for elastic and plastic components of total strain, is not used because the model gives plastic strains directly.

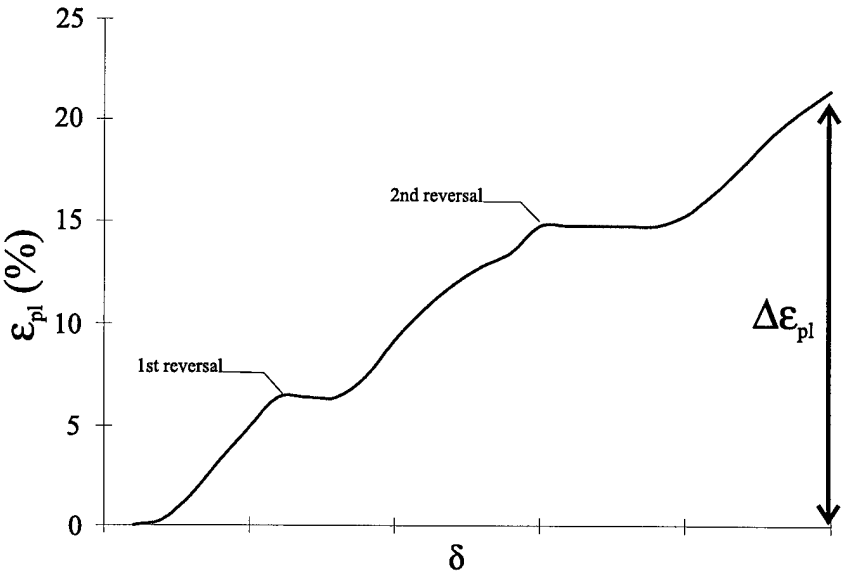

Figure 4-9: The evolution of equivalent plastic strain through one and a half fretting cycles. Plateaus in the value of plastic strain correspond approximately to load reversals, where tractions have suddenly decreased in magnitude and must increase to cause further plastification.

Because the hysteresis response of the system is expected to stabilize following one full fretting cycle, the accumulation of plastic strain will diminish in subsequent cycles. A more realistic life model would result from using the plastic strain increment observed over the second (or even third) fretting cycle. However, using the value at the end of the first cycle is a conservative approach for design purposes, and promises to be an improvement on the Goodman diagram approach.

Plastic strain accumulation for a single fretting cycle under various loading cases are summarized in Table 4.4, along with the predicted number of cycles to failure using Eq. 4.8. All simulations are depicted in Figure 4-10 according to their classification using Ponter et al.'s criteria. It is desirable to determine a relationship between the

accumulation of plastic strain for a given fretting load condition and where it falls within a given regime of elastic or elastoplastic behavior. If a recognizable trend in any regime can be established based on a few simulations, prediction of fatigue life using accumulated plastic strains could be accomplished with knowledge of only the fretting conditions, parameters which have recently been experimentally determined. If valid, this approach is not limited only to sphere-plane contact, but applies to any axisymmetric contact geometry that the model can simulate.

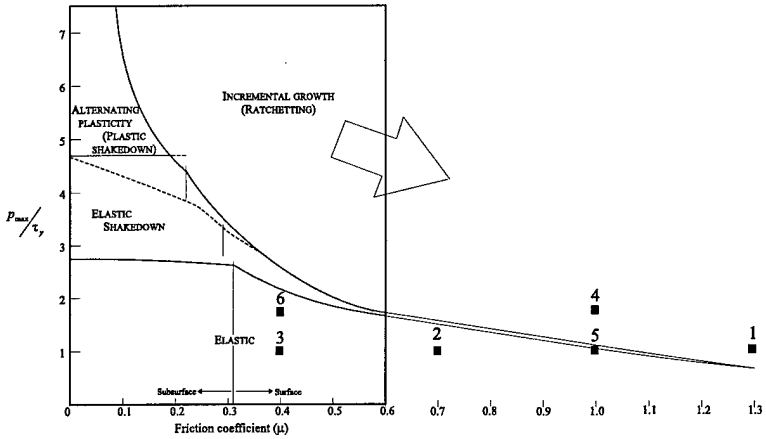

Figure 4-10: Showing steady-state elastoplastic behavior of a circular region under various tangential and normal loads and into which region of predicted behavior fretting simulation loading conditions place them. After Ponter et al. (1985).

Test	$\Delta\epsilon_{pl}^{eq}$ (%)	Pred. elastoplastic behavior	Pred. fatigue life
1	21.5	Ratchetting	3
2	9.43	Fully reversed	15
3	7.47	Fully reversed	23
4	17.8	Ratchetting	4
5	20.8	Ratchetting/fully reversed	3
6	5.39	Fully reversed	43
A	7.21	Fully reversed	22

Table 4.4: Accumulation of plastic strains for fretting simulations. Each accumulation occurs over initial loading and two subsequent reversals, with final tangential force at its maximum value. Test A is a simulation of the experimental test A, described in Chapter 6.

It is necessary to know which type of plastic response — a fully reversing plastic

strain ($\Delta\epsilon_f$) or a monotonically increasing strain ($\Delta\epsilon_r$) — to expect for cyclic plastic loading conditions. A fully reversed plastic strain increment is associated with LCF failure; a monotonically increasing plastic strain is associated with ratchetting, where growth of plasticity is unencumbered because a free surface is available. Kapoor (1994) discusses both of these mechanisms, and points out that they may compete. For contact conditions that are close to the border of the fully reversed flow regime and the ratchetting regime (as are the cases simulated here; see Figure 4-10), determination of the prevailing failure mechanism is difficult or impossible.

The appropriate life prediction relations are

$$N_r = \epsilon_c / \Delta\epsilon_r \tag{4.10}$$

for failure by ratchetting, where N_r is the number of cycles to failure under ratchetting, ϵ_c is a critical accumulated plastic strain, and $\Delta\epsilon_r$ is the accumulated ratchetting strain per cycle;

$$N_f = \left(\frac{2C}{\Delta\epsilon_f}\right)^{\frac{1}{n}}$$

describes failure by LCF; it is a form of Eq. 4.8. For the Al 7075-T6 alloy modelled in these simulations the relevant material properties are as follows: $\epsilon'_f = 0.19$ and $c = -0.52$ [see Fuchs and Stephens (1980)].

4.5 Remarks on the approach

The prediction of fatigue life for components subject to fretting loads may be accomplished via a finite element method determination of equivalent plastic strain increment per loading cycle. A drawback of this approach is that it is generally associated with LCF failure. Further, there may be competing failure mechanisms operating within a fretting fatigue damage site. It will be difficult to know whether the ultimate failure will be due to fully reversed cyclic plastic flow or because of ratchetting. If failure is by ratchetting, the critical plastic strain accumulation for failure must be determined. (This quantity is not as well known for engineering alloys as

the constants c and ϵ'_f in the Coffin-Manson relation (Eq. 4.8 that describes the LCF failure associated with fully reversed plastic flow.)

A single experimental case (test A described in Chapter 5) has been simulated using the finite element method. The specimen tested exhibited a fatigue life of 420,000 fatigue cycles. Application of the Coffin-Manson relation in the manner described predicts a fatigue life of only 22 cycles; the method seems overly conservative. More realistic fatigue life prediction may be obtained by monitoring the increment in equivalent plastic strain during fretting cycles subsequent to the first or second; in general the plastic strain increment will decrease substantially to a steady-state value after the first one or two fatigue cycles.

Chapter 5

Design and Construction of a New Fretting Fatigue Test Apparatus

5.1 Introduction

An important aspect of this work has been the design and construction of an apparatus for performing quantitative fretting fatigue tests. The device allows accurate measurement and control of normal contact force, tangential contact force, relative displacement between contacting surfaces, and bulk fretting loads, and allows measurement of average coefficient of friction. Its design is simple, and features interchangeable fretting contact pads, allowing use of various pad geometries without major adjustment. The device incorporates many points of adjustment for alignment and compliance, making it a robust frame for a wide variety of fretting-fatigue conditions involving different materials. This chapter addresses theoretical and practical design considerations for the device. The capabilities of this device are also demonstrated in Chapter 6 via fretting fatigue experiments conducted on a 7075-T6 aluminum alloy.

5.2 Previous fretting fatigue test devices

Experimental study of fretting fatigue in particular is fraught with difficulty. While the conditions of contact in fretting situations range from geometrically simple to very

complex in form, it is in all cases very difficult to replicate fretting contact conditions in a laboratory while maintaining a precise knowledge of what exactly the experimental conditions are. Several methods of fretting fatigue testing are available. One involves the use of an ordinary uniaxial fatigue test machine to hold a fretting specimen that is also laterally loaded by two fixed fretting pads. Relative displacements between contacting surfaces are caused by extension of the specimen and machine compliance. This type of frame was used by Nishioka and Hirakawa (1969*a*), Hoeppner and Goss (1974), Nowell (1988), and others. Another possibility is the use of a torsional fatigue test machine such as the one used by Endo et al. (1974), again laterally loading the specimen with fixed pads. Advantages of both of these machines are that they allow easy control of the specimen bulk stress level and permit use of different fretting pad geometries. Fenner and Field (1960) employed 'bridge'-type fretting pads, i.e., bracket-shaped contacts that produce flat contact in two places on each side of the specimen (see Figure 5-1*a*). Milestone (1970), in contrast, used flat cylindrical pads, which give the advantage of creating a contact stress field that is analytically calculable in closed form. Vincent et al. (1992) criticize any fretting test

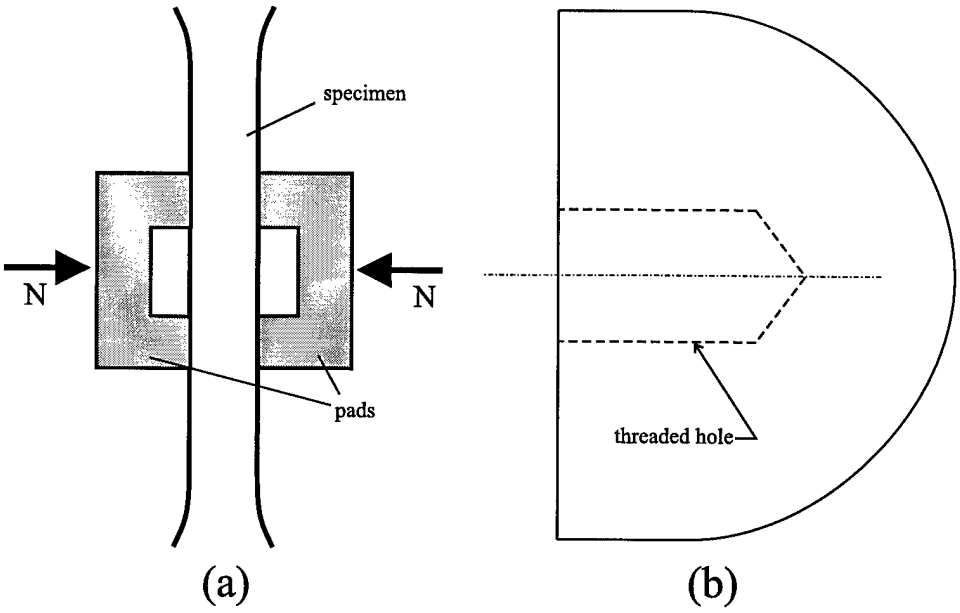

Figure 5-1: a) 'Bridge'-type fretting pads and b) spherical replaceable fretting pads.

assembly that uses fixed pads in conjunction with specimen bulk stress-induced rel-

ative displacements, citing a greater fretting-induced life reduction observed in tests than in actual service conditions, uncontrolled tribological conditions, and local overstresses of the specimen caused by the fretting pad. In particular, they point out that the calculated displacement (due to extension or twisting of the specimen) is always less than the actual relative displacement between contacting surfaces because of the compliance of the pad supports. Their recommendation is to use the third main type of fretting test apparatus, one which uses a static specimen with a fixed stress level. Relative displacements are created by moving the fretting pads back and forth with an actuator. This approach also allows use of many types of contact pad geometry, and perhaps a greater control over relative displacement between the contacting surfaces. Difficulty lies in construction of an actuator control system with which to move the pads. Here we also mention that controlling motion of fretting pads does not remove from consideration the issue of machine compliance as it relates to error in measured versus actual relative displacements. There remains some material between the point of actuator control and the point at which the pads contact the specimen; this also leads to a finite compliance in the pad system that must be accounted for. To our knowledge, no investigators have measured both tangential force and cyclic relative displacement during fretting fatigue tests; the apparatus described herein allows these measurements. Its design and construction are much simpler and more economical than the recently developed fretting test frames [c.f. Anton et al. (1997)], which utilize coordinated biaxial digital control. While such apparatus permit precise control of normal fretting loads synchronously and asynchronously at any phase angle with bulk axial specimen stress, they still suffer from serious difficulties in controlling cyclic displacements during fretting fatigue.

The new test apparatus described here builds on the first type mentioned, i.e., it utilizes a tensile fatigue test machine with nominally stationary fretting pads. The design incorporates the advantages of other fretting test assemblies reported in the literature while overcoming many of the limitations of these frames. Notable among these features is use of interchangeable fretting pads. Any geometry may be utilized; one must simply create pad attachments that thread onto the permanent pad

supports. The advantage is that small amounts of material may be used to create new fretting pads. The present work has utilized spherical fretting pads; these may be machined to any specified radius of curvature, but need never be larger than a cylinder 25 mm in diameter by ~25 mm in height (see Figure 5-1*b*). This is highly desirable for testing titanium alloys and other materials that are costly to acquire and machine.

Particular attention has been given in the development of this apparatus to the measurement of the actual relative displacements between the fretted surfaces. Rather than coarsely assume specimen extension at the point of contact to be equal to the relative displacement, an extensometer assembly has been included to record *in situ* displacement measurements between points on the fretting pad and on the specimen. These measurements may in turn be used to accurately determine the actual relative displacement at the point of contact, as described in Section 5.5. Vincent et al. (1992) claim that one of the key limitations of fretting test frames using fixed pads in conjunction with a uniaxial fatigue test machine is that the displacement developed during the test is solely a function of axial load applied to the specimen and a fixed and uncontrollable friction force. This is true for frames of a fixed compliance. It is noted that the present apparatus, however, offers means for adjusting compliance, both the compliance of the pad supports as well as the load train of the uniaxial test machine. This allows one to fix independently any combination of axial load, tangential load, and relative displacement within an envelope defined by material performance and machine actuator limitations.

Important parameters to control and/or monitor in fretting fatigue tests include: (*i*) normal contact force, (*ii*) amplitude of relative sliding displacement, (*iii*) cyclic loading frequency and waveform, (*iv*) specimen residual and bulk stresses, (*v*) tangential load developed at the point of contact, (*vi*) elastic properties of contacting materials, (*vii*) environment and temperature, and (*viii*) microstructural changes in the specimen and pads. Some parameters are measured with greater ease relative to others, but meaningful comparison of fretting test data cannot be accomplished without accurate observation of all of these. It is with a mind to facilitate this effort that

we offer the following description of a fretting fatigue test apparatus, observations about its construction, and comments on its use.

Section 5.3 offers a detailed description of the fretting fatigue test apparatus. Sections 5.4 and 5.5 describe the parameters which may be measured using the apparatus and their measurement in practice, respectively. Section 5.6 contains observations on friction coefficient measurements, an area of particular experimental difficulty. Further experimental work is described in Chapter 6.

5.3 Description

5.3.1 Basic construction

The fretting fatigue test apparatus is designed and constructed in conjunction with a servo-hydraulic uniaxial test system configured with a 10–kN load cell and capable of cyclic loading frequencies of 0–50 Hz. The *actuator* and *load cell* labeled LC1 in Figure 5-2 are part of the servo-hydraulic test system; the remainder of the components in the test frame are fabricated independently and attached to it. As shown in Figure 5-2, the *rigid base* is constructed of hot-rolled steel and bolts directly to the base of the servo-hydraulic test machine. The top and bottom of this base are machined to be parallel, and planarity is verified using a machinist's table. The *points of support* consist of steel bars which may be bolted anywhere along two sets of through-thickness slots cut out of the base. The bolts holding the points of support also attach the *flexible plates* on either side of the apparatus to the base. These cold-rolled steel plates may be of varying thickness and, along with adjustment of the position of their points of support, provide an appropriate amount of compliance for the fretting pad support assembly. The flexible plates attach to a *stiff plate* that spans the center of the test machine; attachment at both the points of support and the stiff plate is such that the plates behave as if they are beams with both ends fixed. Four *load cells* (labeled LC4, LC5, LC6, and LC7 in Figure 5-2) are threaded directly into the stiff plate and are used to measure tangential loads exerted on the fretting pads by the specimen. *Linear bearings* on both pairs of these load cells allow the horizontal trans-

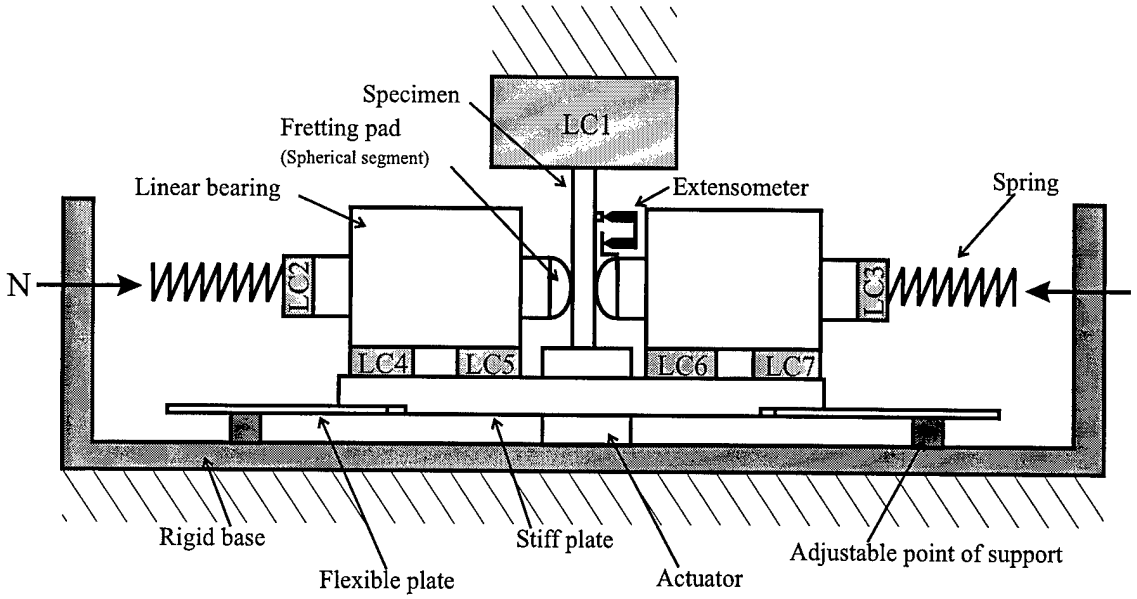

Figure 5-2: Fretting fatigue test frame schematic

lation of the *cylinders* that support the replaceable *fretting pads.* The load train for application of normal loads begins with an adjustable *spring* that extends normal to the vertical sides of the rigid base. Compression of the springs causes reaction forces that can be measured at the *load cells* labeled LC2 and LC3. The reaction force arises from resistance to cylinder motion by the linear bearing and, when the fretting pad contacts it, the countering force from the specimen. The resistance of the linear bearing is a "loss" of load in that the normal load on the specimen is necessarily less than that indicated by the load cells; this loss must be accounted for when calibrating the apparatus. Photographs of the test frame are shown in Appendix B.

Specimens are flat-sided plates with reduced rectangular gage sections, machined from a 12.7 mm diameter cylindrical test specimen, and with threaded ends to facilitate ease of alignment and slip-free support in the test machine. Various gage sections have been utilized to achieve various specimen compliances; the favored design has a gage length of 102 mm and a cross-sectional area of 41.6 mm^2. Two bolts are counter-screwed against LC1 and the actuator, respectively, to further decrease the likelihood of specimen slip relative to the uniaxial test machine. Specimens and the replaceable pads are shown in figure 5-3.

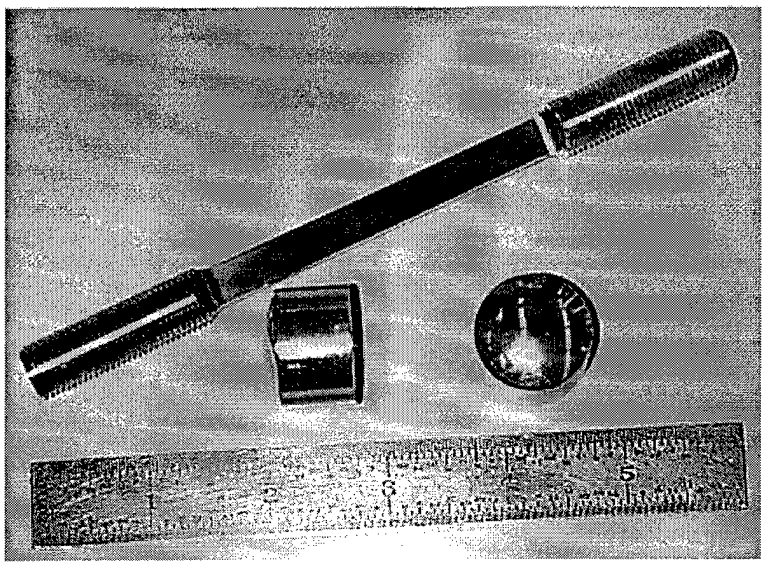

Figure 5-3: A test specimen (top) and two fretting pads, shown with a 152.4 mm ruler.

The *extensometer* assembly used to measure relative displacement between the pad and specimen is shown on Figure 5-2 to the right of the specimen and also in greater detail in Figure 5-4. In Figure 5-4, the first part of the *holding unit* for the extensometer is shown inserted between the replaceable fretting pad and its support cylinder. The horizontal length of this unit's horizontal arm may be adjusted so that the attachment point for the lower blade of the *extensometer* is the proper distance from the specimen, even if pads of varying thickness are used. The second part of the extensometer holding unit is simply a thin, rectangular ($\sim 5 \times 20$ mm) steel plate attached perpendicularly to the specimen with a super-glue. The upper and lower blades of the extensometer contact their respective holding units with knife edge contact surfaces. Both are held against the holding units with rubber bands that are looped around the specimen and permit free rotation of the extensometer blades relative to the holding units. In addition to the rubber bands, a super glue is applied along both knife edge contacts. This measure prevents sliding of the knife edges during the test, but does not inhibit their free rotation.

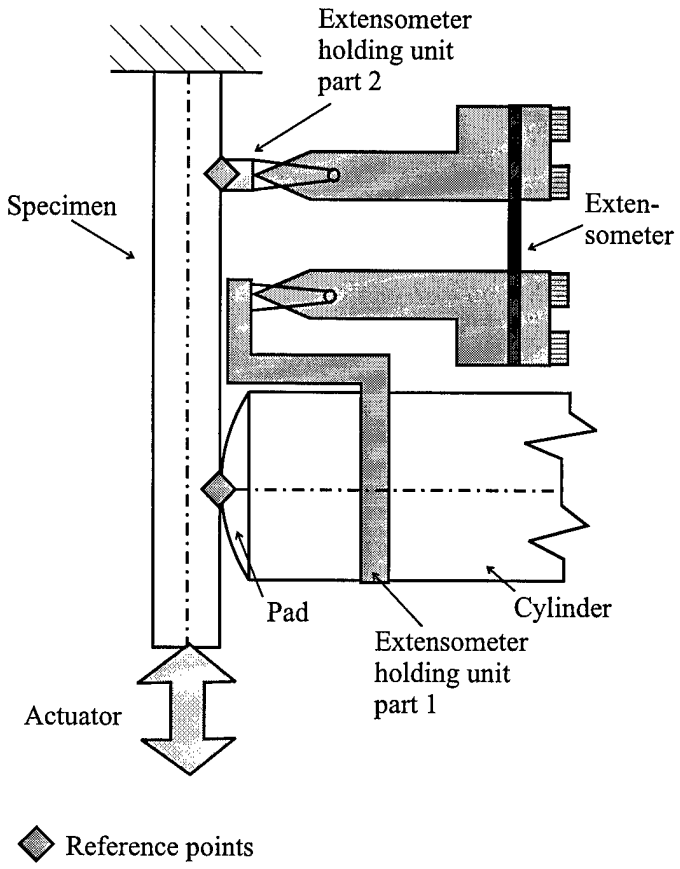

Figure 5-4: Schematic of the relative displacement measurement device

5.3.2 Data acquisition

Data are acquired from the 10-kN load cell onboard the uniaxial test machine, the six 100-N load cells used to measure normal and tangential loads on the specimen, and the extensometer strain gage. LabVIEW® (1996) version 4.0, a PC-based, virtual instrument data acquisition system, is utilized for real-time graphical display and periodic storage of this information. Transducer output signals are conditioned with IC-based signal conditioning cards and with digital filters implemented within LabVIEW.

Several LabVIEW data acquisition programs have been written for fretting tests. These programs are specialized to minimize computational cost for a desired application. Since normal loads are usually set and left constant throughout any given test, one program monitors only load cells 2 and 3, enabling immediate display of precise

real-time load values. A second program designed for use in friction coefficient tests monitors only load cells 1, 3, 6, and 7, and displays a real-time plot showing the sum of load cells 6 and 7 normalized by the value from load cell 1. A 'closed' curve (see Figure 5-5*a*) indicates a stick-slip condition, as tangential force varies directly with specimen elongation, but an 'open' curve (see Figure 5-5*b*) identifies conditions of global sliding, with tangential forces plateauing above a given specimen displacement amplitude. See Section 5.5 for discussion of friction coefficient measurements.

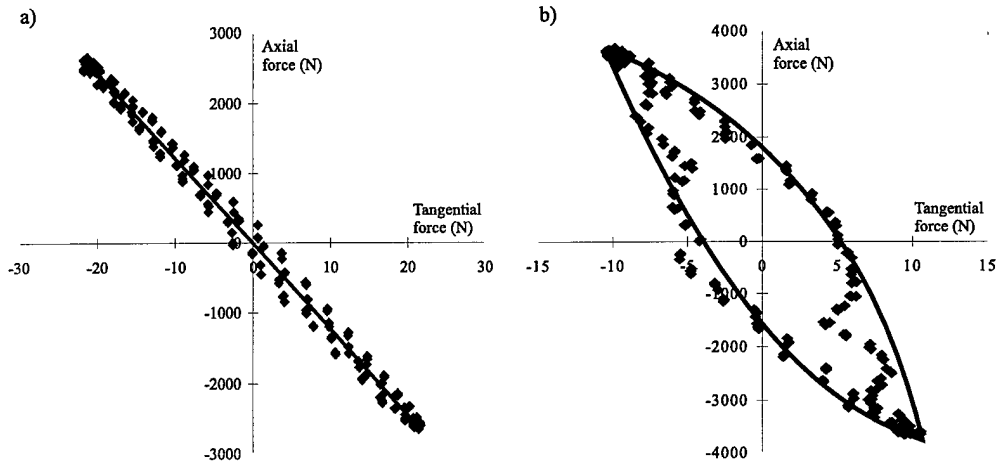

Figure 5-5: Showing a) 'closed' and b) 'open' plots of friction force normalized by axial force.

The master data acquisition program displays and records data from all eight sensing devices. It permits zeroing of all load cell and strain gage readings, and allows a correction factor for the extensometer so that relative displacement between the two reference points may be accurately represented. Normal loads and friction loads are displayed. Plots that indicate a stick-slip or global sliding contact condition (as described in the paragraph above) are included for both the left and right fretting pads. The master program is typically used for observing and storing data from fretting fatigue tests. At a predetermined interval a complete data set is written to a spreadsheet file for subsequent analysis and observation of long-term trends.

5.3.3 Alignment and adjustment

A critical concern for design of a fretting test fixture is alignment of its several components. Meaningful comparison of experimental results to theoretical predictions occurs only if a test frame is sufficiently robust to permit the realization of the theoretical conditions to be duplicated. Here we describe the procedures taken to ensure alignment of the various components of the fretting apparatus.

The most fundamental level of alignment in the fretting fixture is that of the frame itself relative to the uniaxial test machine to which it is attached. The base of the servo-hydraulic test machine was assumed to be flat, although subsequent alignment of other components means this assumption need not be true to have an aligned test system. As previously described, the top and bottom surfaces of the fixture base were verified to be plane and parallel to ± 100 μm. Machining tolerances for all components were within ± 25 μm, thus complementary components on either side of the fixture's vertical axis of symmetry are nearly identical. A cylindrical brass sleeve was machined with an inner diameter slightly larger than the maximum diameter of the test machine actuator and an outer diameter slightly smaller than the circular hole cut out of the stiff plate on the fixture. The cylinder was made to simultaneously fit around the actuator and within the hole in the stiff plate while the fixture was tightly bolted to the test machine. Thus, the center (taken to be the center of the cut-out in the stiff plate) of the fixture corresponds to the center of the test machine actuator. Along an axis that intersects this center point, the actuator travels within a close-fitting cylinder that is normal to the stiff plate. Since the stiff plate is already known to be parallel to the fixture and servo-hydraulic test machine bases, the movement of the test machine actuator can be verified to be along the vertical axis of symmetry of the entire assembly.

At the top of the close-fitting brass sleeve described above are cut two holes aligned perpendicular to the longitudinal axis of the sleeve, with diameters corresponding to the diameter of the pad support cylinders. With the brass sleeve in place around the actuator and within the stiff plate, the pad support cylinders were placed through the aligned holes, and their support structure (including the linear bearings and load

cells 4, 5, 6, and 7) was attached to the stiff plate. This ensures that the longitudinal axes of the cylinders are collinear.

Overall fixture alignment may be set once and periodically rechecked by reinstalling the brass sleeve. Alignment of specimens must be accomplished prior to every test, however. To facilitate specimen alignment, a special specimen was created with its sides carefully checked to be parallel to one another. This alignment specimen was then installed in the servo-hydraulic test machine. Ink was placed on the ends of fretting pads installed in the fretting fixture, and they were pushed into contact with the specimen. The locations of the ink spots left on the specimen sides were noted, and the alignment adjusted (via rotation about the specimen longitudinal axis) if the marks were not centered front-to-back on the specimen sides. The process was repeated until ink spots were centered front-to-back on the specimen sides; the specimen was then taken to be aligned with its sides normal to the longitudinal axes of the pad support cylinders. A straight edge was placed flat against either side of the specimen and extended to a fixed area on the actuator, where indelible marks were made corresponding to the location of the straight edge resting point on each side. Alignment of subsequent specimens is verified by installing them in the uniaxial test machine, then adjusting until a straight edge held against either side of the specimen rests on the marks made on the actuator. This technique has worked very well in practice; fretting scars are symmetric with respect to each other and aligned with the loading path of the pad support cylinders, hence they are known to be created during contact with the exact centers of the fretting pads.

It is desirable to have the blades of the extensometer exactly normal to the side of the specimen during a test so that the measured displacement is known to be the relative displacement of the two points to which the blades are attached (see section 5.6). As described above, the point of support for the lower blade of the extensometer (attached between the right-side fretting pad and its support cylinder) may be adjusted so that it is the same distance from the edge of the specimen as the upper point of support (attached directly to the specimen).

5.3.4 System compliance

Much of the robustness of this fretting fixture lies in its potential to have an intentionally varied compliance. Desired combinations of normal force, tangential force, and relative displacement may be achieved by controlling the stiffness of the pad support assembly against tangential motion of the fretting pads. The means of controlling this stiffness are through the load train of the uniaxial test machine and by adjusting the points of support for the flexible plates of the load fixture. Load train stiffness of the servo-hydraulic test machine is constrained to an upper bound by the characteristics of the test machine control system. It may be increased, however, by the installation of a more compliant component between the crosshead and top of the specimen, such as a hollow steel cylinder with female threads to accept specimens and male threads that permit insertion into the test machine crosshead. An increase in compliance of the specimen relative to the pads is also realized by increasing the distance between the points of contact of the fretting pad and the upper end of the specimen gage section. This distance may be considered to be the effective gage length (l_{eff}) for the test. Another simple means of adjusting compliance is with the points of support of the flexible plates. Moving these points of support away from the center axis of the fretting fixture increases its compliance and *vice versa*. The theoretical compliance of the assembly may be calculated via an elastic analysis using strength of materials assumptions.

In practice, though, it is necessary to ascertain the overall effective compliance of the test machine-fixture system (C_{eff}) by performing a static or dynamic test where no global sliding occurs. Since an increase in compliance of the specimen is equivalent to a proportional decrease in compliance of equal magnitude of the fretting frame, the overall value of $\frac{C_{\text{p}}}{C_{\text{q}}} = C_{\text{eff}}$ may be adjusted to the desired level for a given test via the most convenient means available.[1] In general, this is accomplished by adjusting

[1]Compliance is defined as a displacement resulting from a given loading, i.e., $C = \frac{X}{Load}$. In this case, C_{p} is the extension of the specimen for a given axial load, P, or $C_{\text{p}} = \frac{X_{\text{spec}}}{P}$. C_{q} is the displacement of the fretting pad at the point of contact due to the pad support compliance under a given tangential load acting parallel to the specimen longitudinal axis, or $C_{\text{q}} = \frac{X_{\text{pad}}}{Q}$.

the effective gage length of the specimen within a 'compliance envelope' created by a given combination of test machine load train compliance and flexible plate support distance,[2] (h). Experience has shown that effective compliance is a linear function of l_{eff} for a given combination of load train configuration and h. These functions for several combinations have been noted, and thus a wide range of C_{eff} may be achieved with little difficulty.

5.4 Parameters controlled during fretting tests

The following is a list of experimental parameters which may be controlled during fretting experiments:

(1) A **contact load** (N) is applied to either side of the specimen through the fretting contact pads and is controlled via compression of the loading springs over a distance s; it is generally held constant throughout a given test.

(2) The specimen **axial load** (P) may be set with the control system for the servo-hydraulic uniaxial test machine. P is varied to achieve a desired shear force Q, which is itself dependent on P, the total compliance of the test machine system (C_{p}), and the compliance of the fretting pad supports (C_{q}).

(3) The manner of controlling the **tangential load** (Q) depends on whether or not global sliding occurs. Under conditions of global sliding, the amplitude of Q depends on the friction coefficient μ and normal load N; in this case it may be controlled directly by varying N. For stick-slip conditions, variation of Q with respect to time will depend on the compliance of the system used to apply the specimen axial load (P) (i.e., the compliance of the test machine components, C_{p}), as well as the compliance of the pad supports, C_{q} [Endo et al. (1974), Hills and Nowell (1992)]. By appropriately adjusting these compliances, the amplitude of Q may be set; its value at any moment will be

$$Q = -\frac{C_{\text{p}}}{C_{\text{q}}} P, \tag{5.1}$$

[2]That is, h is the distance between the points of support for the flexible plates and the points where the flexible plates are connected to the stiff plate.

where Q is positive when it acts to produce an axial load in the specimen of the same sense as a positive axial load (P). As discussed in the previous section, specimen compliance (C_p) may be changed by modifying the contact point of the fretting pads on the specimen (changing the effective gage length (l_{eff}) and consequently the displacement (δ_a) of the contact point), or by adding a compliant element between the test machine load cell (LC1) and the specimen.

(4) For conditions of global sliding, the **relative displacement** δ between contact points is controlled in a manner similar to that used to fix Q in stick-slip conditions. When Q reaches its maximum value of μN and global sliding commences, its amplitude is indirectly related to P, N, C_p, and C_q through the relation

$$\begin{aligned} \delta &= [P + 2Q]C_p + QC_q - 2\Delta \\ &= [P + 2\mu N]C_p + \mu NC_q - 2\Delta, \end{aligned} \tag{5.2}$$

where Δ is the relative displacement due to Q between the center of the contact zone and point D [see Figure 5-6; Johnson (1985)].

(5) The **contact zone size** a may be changed by using different contact pad geometries. In point and line contact, the size depends on the radii of the contacting spherical or cylindrical surfaces, respectively. A similar effect on contact zone size is realized for other pad shapes, e.g. circular flat or rounded pads. For nonconforming contact surfaces, e.g. sphere-plane contact, variation of N produces a change in contact size. This geometric change also produces a change of contact stresses. For example, in point contact with all other parameters held constant, a change in pad radius produces a change in the maximum surface contact stress. To maintain a constant value of this maximum stress for a changing pad radius, new values of Q and N must be applied. The equations defining the size of the contact zone (a) and maximum stress (p_0) are

$$a = \left(N \frac{3\,(1-\nu^2)}{4} \frac{R^*}{E^*} \right)^{\frac{1}{3}} \tag{5.3}$$

and

$$p_0 = \frac{3N}{2\pi a^2}, \tag{5.4}$$

where E^* and R^* are the equivalent Young's modulus and radius of the spherical surfaces, respectively, given by

$$R^* = \frac{R_1 R_2}{R_1 + R_2} \tag{5.5a}$$

$$E^* = \frac{E_1 E_2}{E_1 + E_2}, \tag{5.5b}$$

where the subscripts 1 and 2 refer to the bodies in contact.[3] To maintain constant p_0 after changing a, N must be altered according to equations (5.3) and (5.4).

(6) While it is a parameter (or more correctly a set of parameters) generally desired and set to be constant for all experiments, **alignment** is a critical consideration for fretting fatigue tests. The effect of misalignment differs with the type of contact pad used.

- In the case of point contact, it is important to have the center of the contact zone at the center of the pad, along the path of sliding for the pad, and with the force vector of N completely normal to the plane of the specimen. Then loading is symmetric, with no load components outside of an axis normal to the specimen surface.

- For line contact, the longitudinal axis of the cylindrical surface must be perpendicular to the specimen longitudinal axis and parallel to the contact plane. Normal load must be distributed evenly along the line of contact. To avoid nonuniform distribution of loading pressure in this configuration, a connection allowing rotation about an axis parallel to the specimen longitudinal axis may be employed.

- For planar contact with either flat or round pads, alignment is of utmost importance, as misalignment creates an asymmetric pressure distribution. Special care must be given to avoid rotation of the fretting pads due to shear loads Q. While in point and line contact this rotation produces only a small displacement

[3]Eq. 5.5b holds for bodies comprised of materials having identical Poisson's ratios (ν).

of the contact point or line via relative rolling between the specimen and pad, the effect is more pronounced in complete contact geometries. Sato (1992) has analyzed the effects of pad support stiffness in the fields developed under planar contacts. For all types of contact, it is essential to verify that any rotation of the pads due to the tangential load Q does not significantly alter the contact position.

5.5 Measurement of key parameters

The following parameters of interest may be controlled using the fretting fixture:

(1) The **contact load** (N) is measured independently on each side with 100-N capacity load cells (LC2 and LC3), which are placed at one end of the cylinders through which the normal load is applied, away from the contact point. See Figure 5-2.

(2) The specimen **axial load** (P) is measured with the load cell of the servo-hydraulic uniaxial test machine (LC1). Its value is monitored both by the onboard control systems of the test machine as well as the PC-based data acquisition software.

(3) The **tangential load** (Q) is measured independently on the right side of the assembly by load cells LC4 and LC5, and on the left side by load cells LC6 and LC7. On either side, Q is the sum of the load measured by the load cells associated with that side, i.e., $Q_{\text{right}} = F_{\text{LC4}} + F_{\text{LC5}}$ and $Q_{\text{left}} = F_{\text{LC6}} + F_{\text{LC7}}$.

(4) Measurement of the **relative displacement** δ between the contact surfaces is a task of some difficulty. Many investigators have performed fretting fatigue tests during which they measured relative displacement of the contacts — see Nishioka and Hirakawa (1969*a*), Blanchard et al. (1991), Fouvry et al. (1995), Gaul and Duquette (1980), and Bryggman and Söderberg (1988) — but there are substantial differences among the various reference points and measurement systems they utilize. Consequently, true relative displacements may vary significantly from reported values. For example, Nishioka and Hirakawa (1969*b*,*d*) report in the literature cases for which the relationship between tangential load and measured relative displacement is essen-

tially linear. These results are produced because the measured displacements do not actually reflect relative sliding, but rather relative displacement between two points far enough from the contact zone that significant relative motion occurs even when there is no global sliding at the contact. It is misleading to report a relationship between this relative displacement and damage accumulation; damage accumulation is affected by relative displacement at the contact, which may differ substantially from the relative displacement of these distant points.

To ascertain a valid relationship between sliding amplitude and the resulting damage, it is necessary to perform accurate and precise measurement of the actual relative displacement between the contacting surfaces. The fretting apparatus described here permits such measurement, utilizing an extensometer specially designed with a high level of compliance so that it produces negligible loads under typical fretting displacements (see Figure 5-4).

The extensometer measures relative displacement between two reference points. One blade of the extensometer is fixed at point B' on the specimen; the other is fixed directly to the pad support at C'(see Figure 5-6*a*). The extensometer measures only the relative displacement between the reference points shown in the figure. To calculate the actual relative displacement at the point of contact, it is necessary to also consider the increase in length between points A and B, the displacement (Δ) between the reference points A and D and the centers of their respective surfaces (see Figure 5-6*b*), and the relative motion between points C' and D. If δ is defined as the relative sliding distance between two arbitrary points on the surfaces of the specimen and pad, displacement between A and D can be represented by

$$\delta_{\text{ad}} = \delta + 2\Delta \tag{5.6}$$

The value of Δ is related to the stresses produced by contact loads, and is given by

$$\Delta = -\frac{3Q}{16a}\frac{2-\nu}{G}\left(1-\left(1-\frac{|Q|}{\mu N}\right)^{\frac{2}{3}}\right), \tag{5.7}$$

where ν is the Poisson ratio, $|Q|$ is the absolute value of Q, and G is the shear modulus.

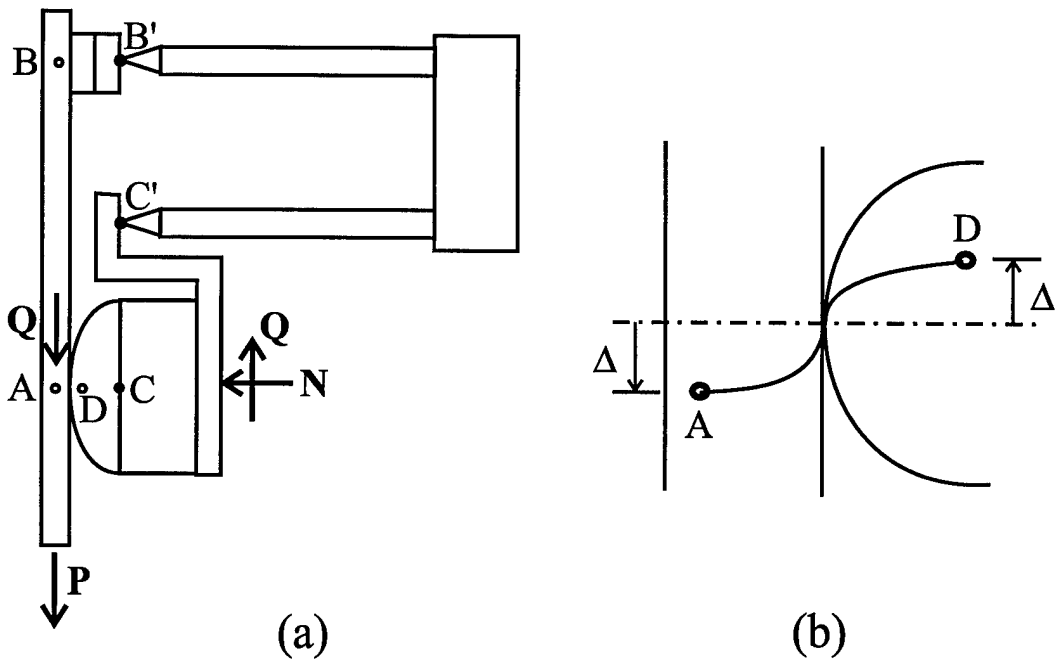

Figure 5-6: Showing a) various points on the relative displacement measurement assembly referred to in the pertinent discussion. The detail in b) shows displacements (Δ) between points A and D and corresponding points at the surfaces of their related components.

Between D and C there is a relative motion produced by the rotation of the line $\overline{CD}$. The magnitude of this rotation is a linear function of Q, but is in all cases very small because the distance CD is small:

$$\delta_{\mathrm{DC}} = -\alpha l_{\mathrm{DC}} Q, \tag{5.8}$$

Here l_{CD} is the distance CD and α is a constant with linear dependence on the compliance C_{q}. The value of α may be obtained by conducting two static tests in a stick-slip contact situation, each one with a different distance DC (D_1C_1 *and* D_2C_2), but with the same Q, and applying the relation

$$\delta_{\mathrm{ext1}} - \alpha l_{\mathrm{D_1C_1}} Q = \delta_{\mathrm{ext2}} - \alpha l_{\mathrm{D_2C_2}} Q. \tag{5.9}$$

The vertical component of the motion of point C is the same as that of point C', which has a very small horizontal motion. Taking into account the distance $B'C'$, the horizontal motion of C' has no effect on the lecture of the extensometer. Points

B and B' have the same vertical position. Thus, the vertical motion of C relative to B (δ_{bc}) is equal to the opening or closing displacement of the extensometer (δ_{ext}). Additionally, the motion of A relative to B can be written

$$\delta_{ab} = \frac{P + 2Q}{SE} l_{ab} \tag{5.10}$$

where S is the cross-sectional area of the specimen and E is the specimen Young's modulus. Therefore the relative displacement δ is

$$\delta = \delta_{ab} - (\delta_{ext} + \delta_{DC} + 2\Delta)\,. \tag{5.11}$$

A final check of the accuracy of the relative displacement measuring system can be obtained by performing a fretting fatigue test under stick-slip conditions. For this case,

$$\delta_{ab} - (\delta_{ext} + \delta DC) = 2\Delta, \tag{5.12}$$

where δ_{ab} and δ_{DC} can be obtained from equations (5.10) and (5.8), respectively, and Δ can be calculated from equation (5.7). These calculations are accomplished by LabVIEW in real time, providing a direct display of the relative displacement.

(5) Another parameter of importance in fretting fatigue processes is the **friction coefficient** μ. Under global sliding conditions, μ can be obtained by directly measuring the contact normal force N and the amplitude of the tangential force Q; it is the ratio

$$\mu = \frac{|Q|}{N}.$$

Accurate measurement of the friction coefficient for stick-slip conditions is a more difficult task.

Endo and Goto (1976) have shown that the friction coefficient between surfaces under relative sliding, global or partial, changes during a fretting fatigue test. In stick-slip conditions, relative sliding begins with a low value of μ when an axial load P is applied. If Q is high enough initially, global sliding may be produced. The friction coefficient increases with increasing cycles until contact conditions are those

of partial sliding and $\mu = |Q|/N$. After this, part of the contact zone does not experience sliding; its friction coefficient does not change. Another part — the slip zone — may experience a continued increase in μ until it stabilizes at a certain value. During this process, the increase of the friction coefficient coincides with an increase in the size of the stick zone. Generally, it takes a small number of fretting cycles, with either global or partial sliding, to achieve quasi-stable value of μ, although Endo and Goto (1976) and Blanchard et al. (1991) have observed that the number of cycles may in some cases be very high. This suggests that the value of μ may change from point to point in the stick zone, and also differs at the boundary between the stick zone and slip zone, with smaller values in the stick zone. If μ has a dependency on the relative sliding amplitude, it could also vary within the slip zone.

Under such circumstances (i.e., stick-slip conditions), an increase in the amplitude of the axial load (P) may produce global sliding; this is coincident with an increase in μ in the area that was previously a stick zone where a stabilized value of μ had not been achieved. This in turn may lead to a new stick-slip situation following some number of cycles of global sliding. The new conditions produce a smaller stick zone. Subsequent increases in P result in corresponding increases in μ within the stick zone and reduction in stick zone size. A permanent global sliding condition results after a final increment of P. It may be assumed that once the value of μ has stabilized at any point in the slip zone, it does not change after global sliding again commences due to incremental increases in P. Following this assumption, the ratio $|Q|/N$ at the moment of incipient global sliding after the final increment of P can be considered a good approximation of μ within the slip zone. For point contact or line contact conditions, μ can also be measured using one of the following procedures:

- Apply a cyclic load P with a constant normal load N. The compliances C_{p} and C_{q} must be adjusted to achieve an amplitude of the tangential load Q that creates a stick-slip condition. After enough cycles to ensure stabilization of the system, the test is stopped and the dimensions of the stick zone are measured.

The friction coefficient can be obtained using the relation

$$\frac{b}{d} = \left[1 - \frac{Q}{\mu N}\right]^{\frac{1}{2}} \tag{5.13a}$$

in the case of line contact, and

$$\frac{c}{a} = \left[1 - \frac{Q}{\mu N}\right]^{\frac{1}{3}} \tag{5.13b}$$

in the case of point contact; d and b are the half-widths of the contact zone and stick zone, respectively, and a and c are the radii of the contact zone and stick zone, respectively.

- A procedure proposed by Hills and Nowell (1992) for the case of line contact may also be extended to point contact. Following the application of loads P and N as described above and after applying enough cycles to ensure hysteretic stabilization, the test is stopped. Maintaining the normal load N, the amplitude of P is increased until global sliding commences. The tangential load at the moment of sliding Q_{slip} is recorded. If, as usual, there is global sliding at the beginning of this test, then the size of the stick zone has grown with a constant value of Q. For this case, it is valid to assume that in the stick zone, $x < b$, $\mu(x)$ varies to satisfy

$$\frac{Q}{N\mu(x)} = 1 - \left[\frac{x}{a}\right]^{\frac{1}{2}} \tag{5.14}$$

and that outside the stick zone, $x > b$, μ has a constant value. The size of the stick zone b has an unkown value. However, with these data and the pressure distribution $p(x)$ on the contact zone, it is possible to calculate the value of μ that satisfies

$$\frac{Q_{\text{slip}}}{2h'} = \int_0^b \mu(x)p(x)\,dx + \int_b^d \mu p(x)\,dx, \tag{5.15}$$

where d is the outer boundary of the two-dimensional (2D) h' is the length of the contact line. Discussion of cases of two-dimensional (2D) contact are included

5.6 On the measurement of friction coefficients

Various means of measuring the friction coefficient μ merit some discussion here.

(1) The procedure described above in Section 5.5, wherein the amplitude of axial load (P) is increased stepwise in small increments (and so also Q) until stabilized global sliding results, gives a good estimation of the average friction coefficient. Almost all points on the contact surface experience partial slip conditions for at least some amount of time, so it is reasonable to assume that these points have similar friction coefficients. The procedure is applicable to any contact pad geometry.

Accuracy of the results obtained using this method depends on the following factors:

- During the measurement, all points in the contact zone are subjected to global sliding following increments of P; among different arbitrary points, amplitudes of relative sliding vary. The approach produces the same μ that is produced in the slip zone during stick-slip conditions, provided that the final friction coefficient is not dependent on the amplitude and number of cycles of relative global sliding. If the friction coefficient *is* dependent on relative sliding amplitude and number of cycles, then the value of μ obtained after several increments of P is different from that obtained during a fretting fatigue test with a single amplitude of P throughout.

- Accuracy is also dependent on the increment in P used for each loading step. Assuming that $\mu = |Q|/N$ at the beginning of permanent global sliding presupposes μ to be constant throughout the contact zone, with no variation between the stick zone and the slip zone. Experimental deviation from this assumed condition produces an error, the magnitude of which depends on the size of the stick zone before the increment of P and on the difference between μ in the stick zone and μ in the slip zone.

(2) Another method of measuring the stabilized friction coefficient for line or point contacts necessitates the measurement of fretting scar and stick zone sizes following

the application of a number of loading cycles under conditions of partial slip. The following considerations are relevant to this measurement:

- The maximum value of Q/N during the test must not be close to the value of the friction coefficient. In practice, it must be small enough to avoid any possibility of global sliding at the commencement of cyclic loading. Any occurrence of global sliding damages the stick zone, making it difficult to detect and measure. The maximum value of $|Q|/N$ used in the test must be close to the initial friction coefficient. In some material systems, this value is quite small compared to the stable value realized in the slip zone during fretting.

- With such small values of Q/N, high b/d or c/a ratios are necessarily produced. According to the relations among these ratios and μ, Q, and N (Eqs. (5.13)), μ is very sensitive to any variation in b/d or c/a. Thus, any error in the measurement of stick zone size produces higher error in the estimation of μ, particularly for point contacts.

(3) The third procedure mentioned above was proposed by Hills and Nowell (1992) to measure μ for line contacts. The method assumes that after initial global sliding, the contact condition transitions to become one of partial slip, and that stick zone size and friction coefficient vary continuously and smoothly such that μ becomes constant in time, although different from point to point, for all points that have stopped sliding. If these conditions exist, the value of $\mu(x)$ for all x in the stick zone, $x \leq c$, can be taken to be the value at which that point stopped sliding, i.e. when $x = c$. Assuming that all points sliding at this moment have the same friction coefficient, $\mu(x)$ can be expressed

$$\frac{Q}{N\mu(x)} = 1 - \left[\frac{x}{a}\right]^{\frac{1}{2}} \tag{5.16a}$$

The equivalent expression for point contact is written

$$\frac{Q}{N\mu(r)} = 1 - \left[\frac{r}{a}\right]^{\frac{1}{3}} \tag{5.16b}$$

where r is the radial position of the point relative to the center of the contact zone. Continuing with these assumptions, the value of Q_{slip} when global sliding commences

under a quasistatic load Q increasing from zero, following the application of a cyclic load with amplitude $Q_2 < Q_1$, may be expressed as

$$Q_{\text{slip}} = \int_0^{2\pi} \left[\int_0^c \mu(r) r p(r)\, dr + \int_c^a \mu r p(r)\, dr \right] d\theta \tag{5.17a}$$

where $p(r)$ is the contact zone pressure distribution:

$$p(r) = p_0 \left[1 - \left(\frac{r}{a} \right)^2 \right]^{\frac{1}{2}}$$

Following substitution of the above expression and equation (5.16b) on Q_{slip}, a change of variable r to $r' = r/a$, and integration from 0 to 2π, 5.17a may be written

$$Q_{\text{slip}} = 2\pi a^2 p_0 \left[\int_0^{\frac{c}{a}} \frac{Q}{N} r' \frac{\left(1 - r'^2\right)^{\frac{1}{2}}}{1 - r'^3}\, dr' + \int_{\frac{c}{a}}^1 \mu r' \left(1 - r'^2\right)^{\frac{1}{2}}\, dr' \right] \tag{5.17b}$$

Recalling that for point contact,

$$p_0 = \frac{3N}{2\pi a^2}$$

and

$$\frac{c}{a} = \left[1 - \frac{Q}{\mu N} \right]^{\frac{1}{3}}$$

the expression can be written

$$Q_{\text{slip}} = 3Q \int_0^{\left[1 - \frac{Q}{\mu N}\right]^{\frac{1}{3}}} r' \frac{\left[1 - r'^2\right]^{\frac{1}{2}}}{1 - r'^3}\, dr' + \mu N \left[1 - \left[1 - \frac{Q}{\mu N} \right]^{\frac{2}{3}} \right]^{\frac{3}{2}} \tag{5.17c}$$

or

$$\frac{Q_{\text{slip}}}{Q} = 3I_1 + \frac{\mu N}{Q} \left[1 - \left[1 - \frac{Q}{\mu N} \right]^{\frac{2}{3}} \right] \tag{5.17d}$$

where I_1 is obtained numerically as a function of $Q/(\mu N)$ (Figure 5-7). Referring to Figure 5-7, the relation $Q/(\mu N)$ can be obtained after measurement of Q_{slip}, and thus μ can be found. The only source of error in the calculation of μ by this procedure is the error in the assumption of $\mu(r)$, which may be significant. The previous assumption of $\mu(r)$ (see Eq. (5.16b)) in the stick zone can be taken as the minimum value of the coefficient of friction for each point in that zone. For a given value of Q_{slip}, the

value of μ in the slip zone is an upper limit of μ; the value $\mu = Q_{\text{slip}}/N$ is a lower limit. When the value of Q in cyclic loading is close to Q_{slip}, the upper and lower limits are very close. For example, when $Q_{\text{slip}}/Q = 1.15$, the lower limit for μ is $\mu = Q_{\text{slip}}/N = 1.15Q/N$; in contrast, Figure 5-7 predicts $\mu = 1.25Q/N$. Since the error inherent in this approach is less than or equal to the range between the two solutions, it is desirable to reduce this range as much as possible. Reduction of the stick zone radius during cyclic loading accomplishes this, thus it is important to begin with cyclic loads Q close to μN when using this procedure.

5.6.1 Additional pad geometries

As discussed previously, a strength of this fretting test fixture design is that it permits the use of multiple fretting pad geometries with out extensive reconfiguration. For any type of pad geometry that does not involve sharp edges (such as cylindrical or flat punches with rounded edges) the pads need only be machined to specifications and threaded onto the end of the pad support cylinders. One additional consideration is essential for pads that involve sharp edges, such as bridge pads or cylindrical punches. The linear bearings used to hold and allow horizontal translation of the pad support cylinders undergo an appreciable amount of rotation each fretting cycle; the rotation is caused by the tangential load Q developed at the contact point, and is effectively C_{q} for the system. This does not pose a problem for incomplete contact geometries such as a sphere-plane configuration. However, even a small bit of rotation in a complete contact condition like plane-plane contact can cause one side of the fretting pad to gouge the fretting specimen and/or force part of the pad off the specimen surface, thereby creating an asymmetric contact stress distribution. For complete contact geometries, a different pad support mechanism is preferred. This adaptation utilizes two flexible plates that extend vertically, normal to the base of the fretting fixture. They rise quite close to the specimen, and fretting pads attach directly to the plates, so as to minimize the distance over which rotation may occur. The load application springs apply a normal force to the flexible plates, displacing them so that the fretting pads contact the specimen. Normal load measurement must occur via a

load cell placed between the fretting pad and the flexible plate so as to exclude the resistant force of the thin plates being acted upon by the springs.

See Chapter 6 for verification of the fretting fixture's performance.

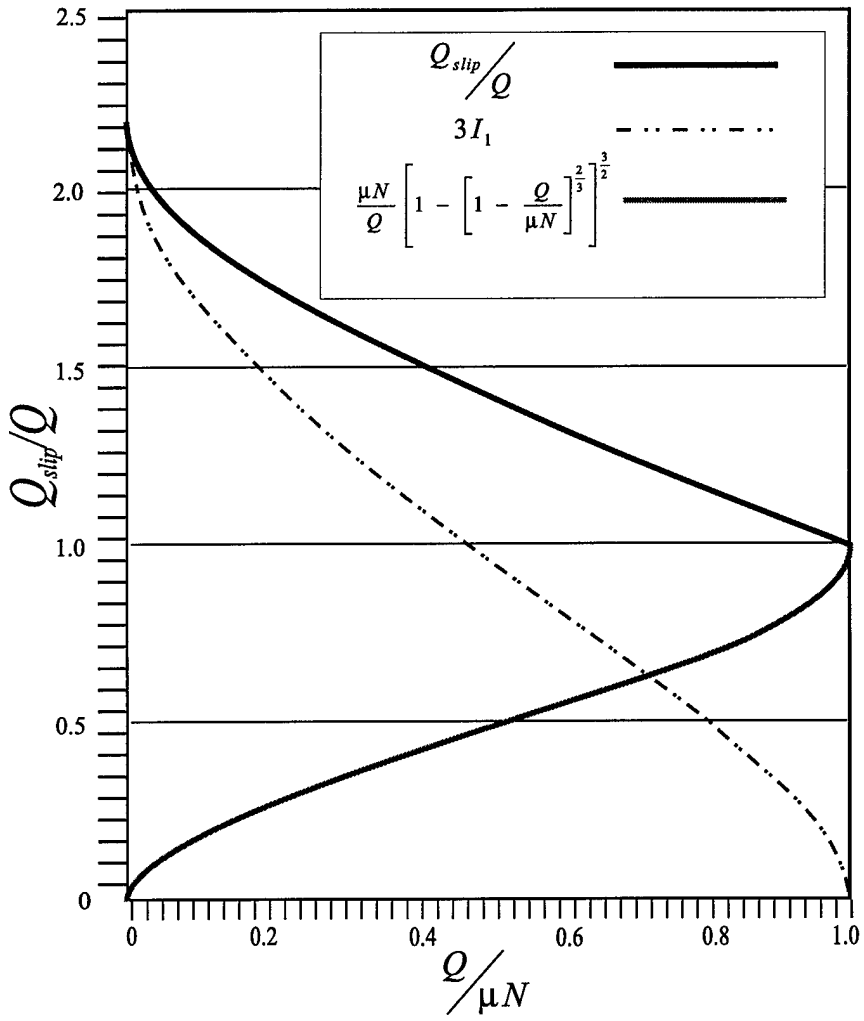

Figure 5-7: Plots of the first and second terms of Eq. (5.17d) and their sum. The sum (the uppermost curve) of the lower two curves may be used to determine μ directly following measurement of Q_{slip}.

Chapter 6

Experimental Results for 7075-T6 Aluminum

The fretting fixture described in Chapter 5 has been used for various types of fretting fatigue studies of a sphere-plane contact geometry. Initial tests were performed primarily for refinement and calibration of the apparatus. The alloy used for tests, Al 7075-T6, is an important structural alloy in modern aircraft. It should be noted at the outset that the T6 heat treatment of this alloy has a notoriously poor resistance to fretting fatigue, and so other heat treatments are used for components susceptible to this type of damage. Regardless, the alloy is ideally suited to use for verification tests because it is relatively inexpensive and there is a large body of experimental literature available for data comparison. A partial list of tests performed and relevant parameters is given in Table 6.1; many of these tests are mentioned in the discussion that follows.

6.1 Creation of fretting scars

The first experimental endeavor was creation of a fretting scar whose dimensions, when compared to the expected dimensions predicted by Mindlin et al.'s (1949, 1953) theoretical work pertaining to contacting spheres under varying tangential loads, would verify proper operation of the fretting device. The apparatus was configured so

Test	N (N)	Q (N)	P (N)	σ_{ax} (MPa)	N_f	Q/N
i[1]	30	±15	±2200	±85	480,000	0.5
A	30	±15	±2200	±85	480,000	0.5
B	20.8	±15	±2150	±83	449,500	0.72
C	15.6	±15	±2200	±85	395,000	0.96
D	12.5	±15	±2150	±83	361,000	1.2
E	18.5	±13.6	±2000	±77	551,000	0.74
F	16	±11.7	±2150	±83	530,000	0.73
G	8.75	±7	±2150	±83	3,000,000*	0.80
H	13	±7	±2150	±83	10,000,000*	0.54
I	13.9	±10	±2150	±83	803,000	0.72
J	10.3	±7.5	±2150	±83	2,940,000	0.73
K	7.31	±6.6	±2150	±83	3,450,000*	0.90
L	8.33	±8	±2150	±83	616,500	0.96
M	8.33	±8	±2150	±83	500,000†	0.96
N	16	±11.7	±2550	±54	424,000†	0.73
O	20	±11.5	±2600	±55	1,410,000*	0.58
P	20	±16	±2600	±62.5	2,186,000*	0.80
Q	20	±20	±2600	±62.5	2,500,000*	1.00
R	24	±20.3	±2600	±62.5	2,660,000*	0.84
					*no failure †test interrupted before failure	

Table 6.1: Fretting test parameters for selected tests.

that contact loading conditions would nominally lead to development of a stick-slip zone, i.e., a circular section of contact where no relative motion between pads and specimen would occur, surrounded by an annulus of microslip. A micrograph of the resulting fretting scar is shown in Figure 6-1. This fretting scar was produced by Al 7075-T6 pads in contact with an Al 6061-T5 specimen. Because of the higher yield strength of Al 7075-T6 (~480 MPa compared to ~320 MPa for Al 6061-T5), this was the last time an Al 6061 specimen was used.

Subsequent tests of Al 7075 specimens contacted by pads of the same material under nominal stick-slip conditions produced fretting scars whose dimensions are in close agreement with theoretical predictions. More photographs of fretting scars may be found in Appendix C. A metric suitable for comparing experimental data to theory is the difference between predicted and observed contact radii. Figure 6-2 shows the

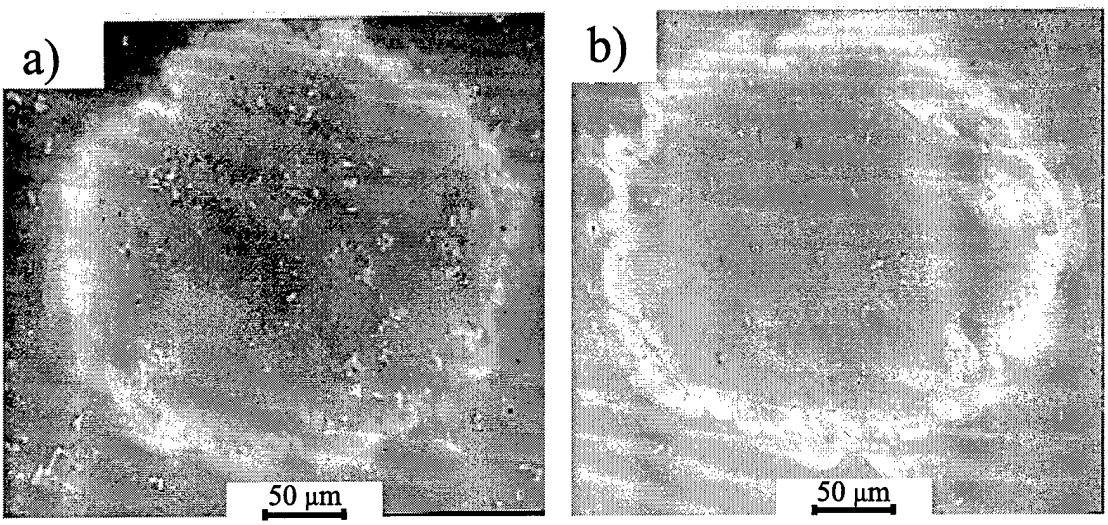

Figure 6-1: Fretting scars produced under stick-slip conditions. Shown in (a) is the scar from the Al 7075-T6 fretting pad, while (b) is the corresponding scar from the Al 6061-T5 specimen. In both the pad and specimen, a circle of undamaged material (the stick region) is seen inside an annulus of microslip. The normal load applied during the test was 15 N, the diameter of the sphere was 12.7 mm, and the test ran for 165,000 cycles.

deviation in radius length of experimentally created fretting scars from the predicted lengths. It is noted that there is good agreement between observed and predicted values for most of the scars shown. The wide deviation exhibited in test H is likely due to the exceptionally high number of cycles experienced. Wear mechanisms have substantially changed the contact geometry and removed a good deal of material from the specimen.

6.2 Measurement of friction coefficient

Tests to determine the coefficient of kinetic friction (μ) have been performed as described above in Section 5.5. For the Al 7075-T6 system studied, μ has been found to be within the range 1.3–1.4, consistent with the findings of investigators such as Lamacq et al. (1997). Note that the friction coefficient at the beginning of tests is considerably lower than that realized at the end of a test. A finite number of fretting

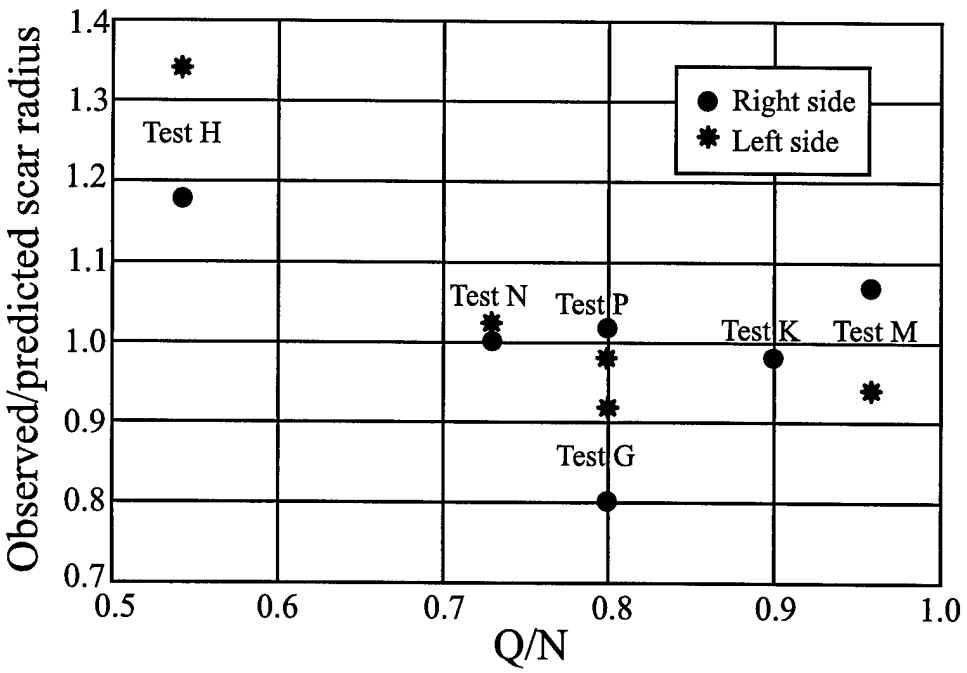

Figure 6-2: Comparison of observed fretting scar dimensions to predicted dimensions.

cycles must occur before the refined surface finish with which the tests are begun has been degraded enough to give the system its steady-state friction coefficient. For low values of $Q/\mu N$ (indicating a large stick region and small slip annulus), equilibrium may be achieved within a few dozen cycles. For loading cases resulting in or approaching global sliding, equilibrium friction coefficient may be achieved only after 10,000 cycles.

6.3 Fretting fatigue tests

Experiments involving fretting fatigue *per se* have been performed. Principal aims for these tests include identification of a threshold value of bulk specimen stress below which surface cracks initiated under the effects of the contact stress fields self-arrest. Further, the initial orientation of cracks, any subsequent change in orientation (e.g., initially oblique cracks turning to grow normal to the specimen surface), and related length dimensions are examined by stopping fretting fatigue tests prior to failure and incrementally polishing and photographing the specimen surface. Several surface

representations at varying depths may be reconstructed to show the crack profile. Since fatigue tests typically run to millions of cycles, fretting scars produced lack the 'clean' appearance of those shown above. This may be caused both by the buildup of wear particles that abrade the entire contact zone as well as some number of cycles where the system undergoes global sliding. In such cases, fretting scars observed at the end of the test have an appearance similar to that shown in Figure 6-3.

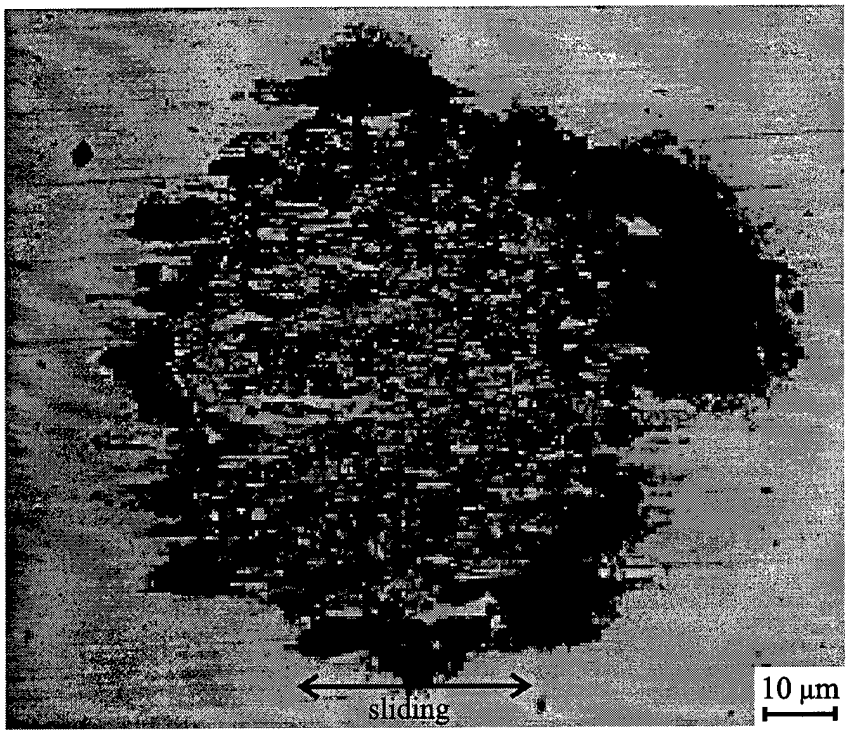

Figure 6-3: Micrograph of a fretting scar produced under nominal stick-slip contact conditions in Al 7075-T6 during a fretting fatigue test. Note that clearly delineated areas of stick and slip are not easily visible, as the accumulation of wear particles and possible global sliding have obscured them.

The first experiments performed were to ensure that observed trends were consistent with expected experimental outcomes. Preliminary data for fretting fatigue tests in the Al 7075-T6 material system are shown in Figure 6-4. Two data sets are shown in the figure. The data points exhibiting a linear trend are for a series of tests wherein tangential load was held constant at 15 N and the maximum amplitude of applied specimen stress was 83 MPa. The ratio Q/N was varied by changing the

normal load. As expected, the fatigue life under fretting conditions decreases as the normal load is increased. The increase in normal load corresponds to an increase in maximum contact pressure and the magnitude of other related elastic values. The data set portrayed with triangular markers is for a set of tests where the maximum amplitude of applied specimen stress is again 83 MPa, but now the ratio Q/N is constant at 0.75. The normal load (shown on the right ordinate scale) and tangential load are varied proportionally. The data exhibit a trend toward longer life at lower values of Q and N. Both of these trends are predicted by the Crossland parameter-based fretting failure maps described in Chapter 3, and serve to validate proper operation of the fretting fixture.

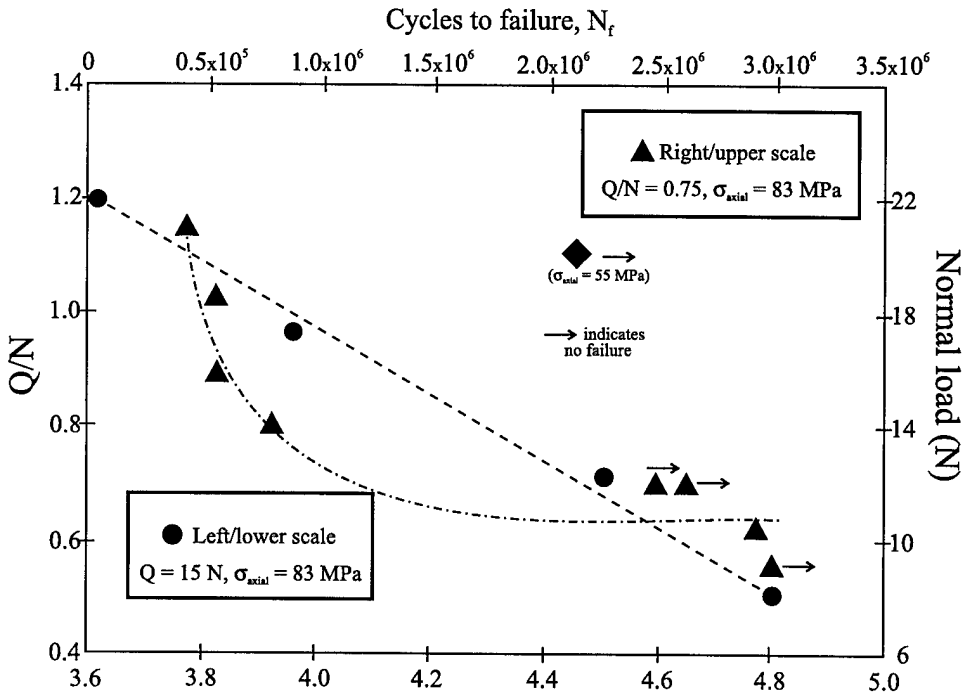

Figure 6-4: Preliminary fretting fatigue test data for Al 7075-T6 specimens. Note the dual scales for both data sets.

6.4 Relative displacement measurement results

Of particular value in the experimental apparatus is its capability to measure relative sliding displacements between the pad and specimen surface. As described in

Section 5.5, some manipulation of the raw extensometer data must be performed to extract actual relative displacement, but this task is not difficult. Proper function of the relative displacement measurement system was verified first in a test known to exhibit stick-slip characteristics, both by theoretical prediction and by observation of a closed tangential load curve (see Section 5.3) during the test. Figure 6-5 shows plots of (a) the raw extensometer data and (b) the data after correction according to the procedure described in Section 5.4. As expected, the displacement is always zero, as there is no relative displacement at the point of contact (the surfaces are perfectly adhered).

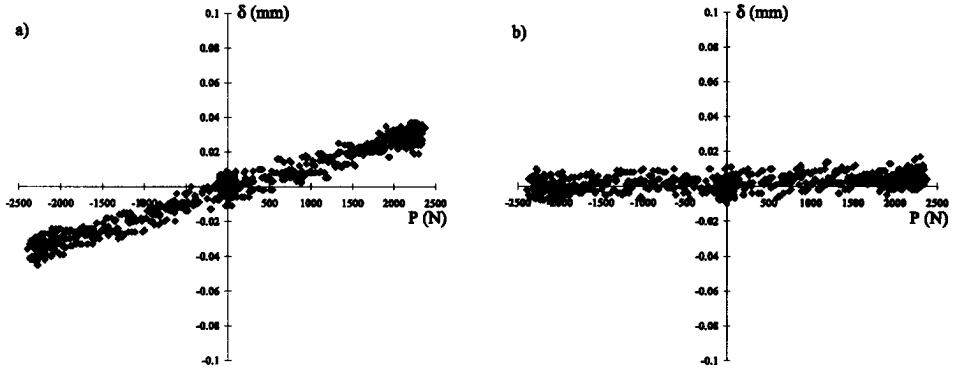

Figure 6-5: a) Raw extensometer data for a *stick-slip* fretting condition. b) Data corrected to show relative displacements between contacting surfaces.

Next, the relative displacement system was utilized in a manner that exploits its true usefulness, i.e. measuring relative displacement in a test involving global sliding. Figure 6-6 shows the raw extensometer data for a global sliding test as well as the corrected values that give actual displacements for the test. Relative displacements are plotted as a function of specimen axial load, thus load extrema correspond to maximum and minimum values of relative displacement.

The open load-displacement curve portrayed here may be explained in the following manner: At a given axial load during initial loading — corresponding to the point at which Q exceeds μN — relative displacement increases monotonically from zero. It reaches a peak value at the maximum axial load. Upon unloading, the relative displacement remains fixed until the opposing shear force magnitude exceeds μN,

from whence it decreases monotonically until the minimum axial load is achieved. This stick-slide process is the same for all load reversals, resulting in a stable load-displacement curve. The initial stick is not shown in Figure 6-6, because data used to make the plot are taken from a series of fretting cycles that do not include the initial loading. Total δ can be determined by simply subtracting the minimum value from the maximum value.

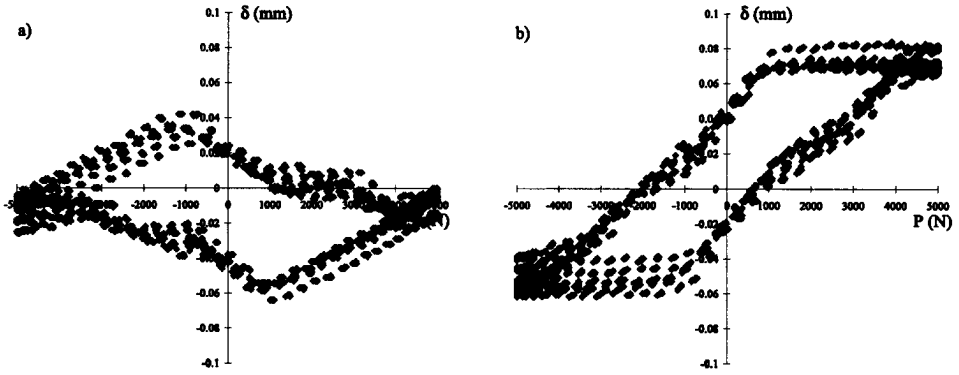

Figure 6-6: a) Raw extensometer data for a *global sliding* fretting condition. b) Data corrected to show relative displacements between contacting surfaces.

Comparison of experimental data collected using the present apparatus with theoretical predictions and the data of other researchers has verified its capability to successfully conduct fretting fatigue tests that incorporate a sphere-plane contact geometry. Further testing should serve to identify which of the life prediction techniques described in this work — the finite element approach to determining buildup of local plasticity (Ch. 4), application of the modified Crossland parameter (Ch. 3), or application of linear elastic fracture mechanics via the crack analogue approach (Ch. 7) — best describe the fretting response of aircraft alloys.

Chapter 7

Potential Application of Fracture Mechanics

It is the author's desire and responsibility to present to the US Air Force as much useful information pertaining to fretting fatigue as possible in this document. Because of recent developments in the application of fracture mechanics to the fretting problem, this chapter offers a description of fracture mechanics as it may be applied to fretting fatigue in various manners, although other work described here did not utilize fracture mechanics approaches. Note that in this chapter alone the symbol a denotes crack length (as per the standard nomenclature of fracture mechanics) instead of contact radius as it does elsewhere.

7.1 Fracture mechanics overview

7.1.1 Griffith energy and linear elastic stress analysis approaches

The beginnings of fracture mechanics are found in the work of Griffith (1921), who determined the necessary conditions for unstable crack growth in brittle solids by equating the loss in mechanical potential energy of a body with a growing crack to the increase in its surface energy due to this growth. In an infinite plate having an

internal through thickness crack, critical crack growth results when the strain energy release rate ($\mathcal{G}$) is twice the surface energy (γ_s). In lieu of this energy approach, necessary conditions for crack growth can be gotten from a linear elastic stress analysis approach. Solutions for the asymptotic stress-displacement fields near the tip of a crack may be given in terms of expressions that involve a stress intensity factor (K) term, nonsingular stresses (also called T-stresses), and other higher order terms. It can be shown that K and $\mathcal{G}$ are related by

$$\mathcal{G} = \frac{1}{E}\left(K_{\mathrm{I}}^2 + K_{\mathrm{II}}^2\right) \tag{7.1a}$$

for plane stress loading and through

$$\mathcal{G} = \frac{1-\nu^2}{E}\left(K_{\mathrm{I}}^2 + K_{\mathrm{II}}^2\right) + \frac{1+\nu}{E}K_{\mathrm{III}}^2 \tag{7.1b}$$

for conditions of plane strain. The indices I, II, and III associated with K denote the stress intensity factors associated with pure mode I, mode II, and mode III crack tip loading, respectively.

7.1.2 Region of K-dominance

Because the stress fields at a crack tip are singular, a plastic zone surrounds the crack tip. Its size may be estimated by determining where the local von Mises equivalent stress fields as determined by a linear elastic analysis exceed the material yield strength. For a mode I crack, the plastic zone radius is given by

$$r_{\mathrm{p}} \approx \frac{1}{3\pi}\left(\frac{K_I}{\sigma_{\mathrm{y}}}\right)^2 \tag{7.2a}$$

for plane strain and

$$r_{\mathrm{p}} \approx \frac{1}{\pi}\left(\frac{K_I}{\sigma_{\mathrm{y}}}\right)^2 \tag{7.2b}$$

for plane stress.

For fatigue cracks, the crack tip experiences reversed plastic flow because the crack tip stresses alternate direction with reversed cyclic loading. For cracked bodies

partially unloaded from a far-field tensile stress, a (smaller) cyclic plastic zone within the monotonic plastic zone is formed at the crack tip. Its radius is

$$r_c \approx \frac{1}{\pi}\left(\frac{\Delta K_I}{2\sigma_y}\right)^2. \tag{7.3}$$

For many crack geometries, the stress fields around the crack tip beyond the plastic zone are closely approximated by the K terms alone over a certain distance, until they begin to deviate substantially from the full stress solutions. This region is the zone of so-called K-dominance. The K-dominated fields are useful for predicting crack growth behavior under fatigue conditions if they completely contain the zone of inelastic behavior immediately surrounding the crack tip. Misapplying concepts that rely on dominant K-fields to problems where higher order terms prevail upon the full solution leads to dangerously nonconservative estimations of crack growth behavior.

7.1.3 Paris 'law'

A concept that rests on the K fields is the empirical relation between crack growth rate per load cycle ($\mathrm{d}a/\mathrm{d}N$) and the crack growth driving force as quantified by the cyclic change in K proposed by Paris, Gomez, and Anderson (1961):

$$\frac{\mathrm{d}a}{\mathrm{d}N} = C\Delta K^m. \tag{7.4}$$

Here C and m are experimentally determined scaling constants affected by many material properties and test parameters. This theory has become the most common means of predicting crack growth rates for a plethora of engineering materials and applications. Since ΔK is a function of applied stress, a, and a geometrical correction factor (often itself varying with a), the expression may be integrated to determine the number of a loading cycles required to grow a crack a given length. If the length of the crack corresponds to a critical failure length, this technique may be used as a life prediction method.

7.1.4 Short crack problem

Many adaptations of the Paris law make it very useful even beyond a consideration of simple — e.g. solely mode I, through thickness, or having faces that do not experience closure during loading — cracks. In spite of its unparalleled success, the nature of the K fields upon which it is predicated dictate that it should not be applied in certain circumstances. One of these limitations is the matter of short cracks. If crack growth rate is predicted solely on the basis of the crack driving force as given by ΔK, it will mimic the solid curve shown in Figure 7-1. The Paris law generally approximates the linearly increasing crack growth rate of the second stage shown in this figure. It is seen that short cracks (dashed lines) in reality exhibit a much higher cyclic growth rate than is predicted, however.

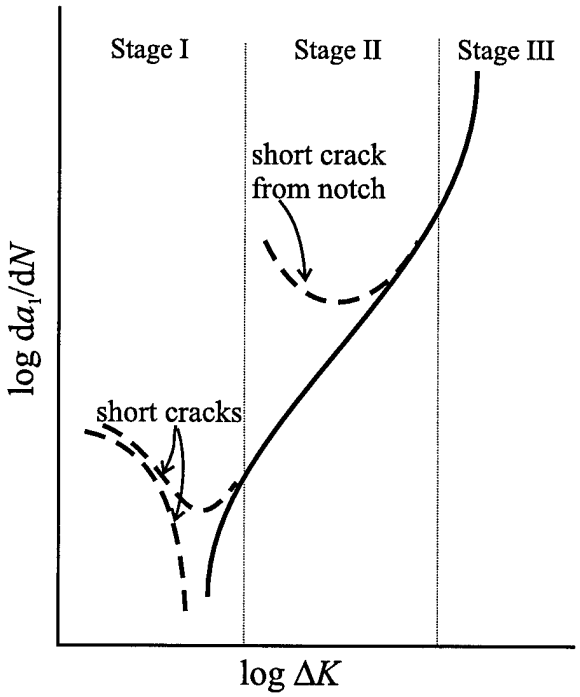

Figure 7-1: A schematic contrasting real short crack growth rates (dashed lines), observed long crack growth rate behavior, and short crack behavior predicted by empirical relations that rely on calculated ΔK values. After Suresh (1991).

Suresh and Ritchie (1984) list the following definitions available to describe short cracks:

1. Cracks near in size to a characteristic microstructural dimension such as grain size are *microstructurally small.*

2. Cracks which have a length close to the size of the plastic zone around them or that are completely surrounded by the plastic strain field near a notch are *mechanically small.*

3. Cracks which are larger than the microstructural dimension and the scale of local plasticity but are 1 or 2 mm or less in length are *physically small.*

4. Cracks which would normally be characterized by a Paris law relation but deviate from this behavior below a certain crack length because of environmental stress corrosion effects are *chemically small.*

All of the above situations prevent successful application of empirical relations based on ΔK to predict crack growth rates. There are a host of other limitations to LEFM (such as mode mixity and crack closure) as well as many other more involved techniques to apply fracture mechanics to cases where LEFM does not apply (the J-integral tops this list), but discussion of these is not appropriate here. Instead we consider methods of circumventing the small crack problem that still allow the employment of LEFM. The typical design technique employed in damage tolerant inspection schemes to overcome an ill-characterized small crack growth stage is that of assuming the presence of cracks the size of detection resolution or larger. Inspection intervals for components subject to LCF, for example, may be determined by integrating the Paris law over a crack length interval defined by a_0, an arbitrary initial crack size for which the Paris law applies, and a_{crit}, the critical failure crack length. (A factor of safety is added.)

This technique is not so useful in preventing HCF failure, however.[1] Because components are subject to a high number of fatigue cycles, cracks that have initiated will grow rapidly. In operational terms, this could mean that a crack in an aircraft turbine blade that was not detectable may grow to critical length over the course of a single

[1]This is not meant to imply that it is not done anyway; c.f. Hattori et al. (1988) and Sato et al. (1986).

sortie. Compounding this difficulty is the reality that most components experiencing HCF are in contact with one another, making most standard inspection schemes impractical. The focus on ameliorating HCF effects then becomes a determination of how to prevent cracks from starting within a given *service interval.* Chapters 2 through 6 of this work have described various ways to predict crack initiation (which often equates with catastrophic failure in HCF situations) through analytical, numerical, and empirical stress- and strain-based approaches. Since fracture mechanics, and particularly LEFM, is such a developed discipline, it is desirable to develop a means of utilizing the body of knowledge related to it that is practicable for dealing with HCF problems like fretting fatigue.

7.2 Crack analogue concept

Recently, Giannakopoulos et al. (1998) have shown an important link between the disciplines of contact mechanics and fracture mechanics that promises to have important practical ramifications in addressing the problem of fretting fatigue. Specifically, they have shown that for some contact geometries — in particular certain complete contact geometries — the asymptotic elastic fields derived from classical contact mechanics analyses are identical to those available from linear elastic fracture mechanics (LEFM) solutions for analogous geometries.

The immediate usefulness of this development is that it allows one to avoid the 'short crack' problem. The contact zone associated with fretting contact can provide a non-arbitrary size scale for the application of LEFM. Indeed, the contact length may be taken to be a fictitious crack length already present in the system. The approach taken in applying this method is summarized as follows:

1. Determine a cracked specimen configuration that is geometrically equivalent, via an appropriate coordinate transformation, to a sharp-edged punch contacting a planar specimen of the same material. (Giannakopoulos et al. have applied this method to a rectangular punch contacting a flat substrate and a cylindrical punch contacting a flat substrate; these geometries and their crack analogues

are shown in Figures 7-2 and 7-3, respectively.)

2. Use classical contact analysis to find asymptotic solutions for elastic fields at the edges of sharp contact.

3. Use LEFM to determine elastic fields for the analogous cracked body. Assume that the body is subjected to a compressive load equal in magnitude to the normal load (N) that the punch exerts on the planar substrate. The scalar amplitude of the crack tip singular fields is given by the stress intensity factor (K).

4. Take the various components of the stress fields found in the two preceding steps, equate them, and solve for K as a function of N, the cracked body geometry, and the characteristic punch dimension.

5. Determine K for the cracked body as a function of N and its geometry; reference any standard fracture mechanics text or handbook.

6. Prove quantitative equivalence between the contact and fracture mechanics solutions by showing that steps 4 and 5 lead to identical results.

Giannakopoulos et al. focus their analysis on the region at a corner of the sharp-edged indenter. It is probable that cracks will initiate at an angle θ below the surface and outside the contact area, as shown in Figure 7-2*a*. Analogously, a kinked crack oriented at an angle ϕ will likely form at the tips of the mode I cracks as shown in Figure 7-2*b*. The two crack orientations are equivalent via the coordinate transform $\pi - \theta = \phi$ for $0 \leqslant \theta \leqslant \pi$.

Further details pertinent to the crack analogue method, including normal (mode I in the crack analogue) and tangential (mode II) loading, the superposition of bulk substrate loading (T-stress), the three-dimensional analogue, and limitations of the approach are left to Giannakopoulos et al. (Note also that this approach is not limited solely to LEFM application. For some cases, it may be extended to encompass the two-parameter approach involving the J-integral and triaxiality parameter.[2]) We

[2]The triaxiality parameter is commonly denoted Q; c.f. O'Dowd and Shih (1991).

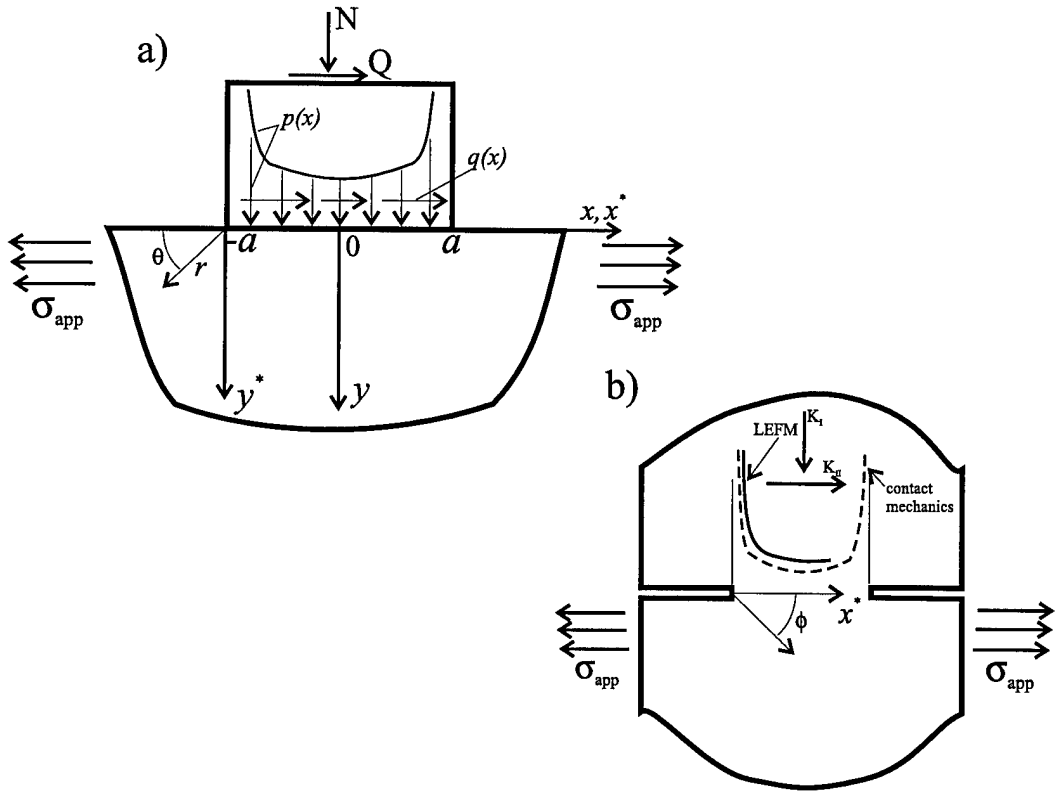

Figure 7-2: a) A flat punch contacting a planar substrate and b) its crack analogue, a double-edge cracked plate with uncracked ligament size equal to the punch dimension.

turn immediately to the application of the method to the problem of fretting fatigue. Many fretting contact conditions in service meet the criteria listed below, which are assumptions made in the static analysis upon which the crack analogue approach rests.

- The substrate is semi-infinite with respect to the punch and is linear elastic and isotropic with small-strain deformation at all times.

- Small-scale yielding occurs at the sharp edges of contact so that the plastic or damage zone is small compared to the contact area, i.e., $r_{\mathrm{p}} \leqslant a/5$.

- Gross sliding does not occur between the punch and the substrate, and partial slip at the outer edge of contact does not significantly affect the asymptotic solutions obtained from contact mechanics.

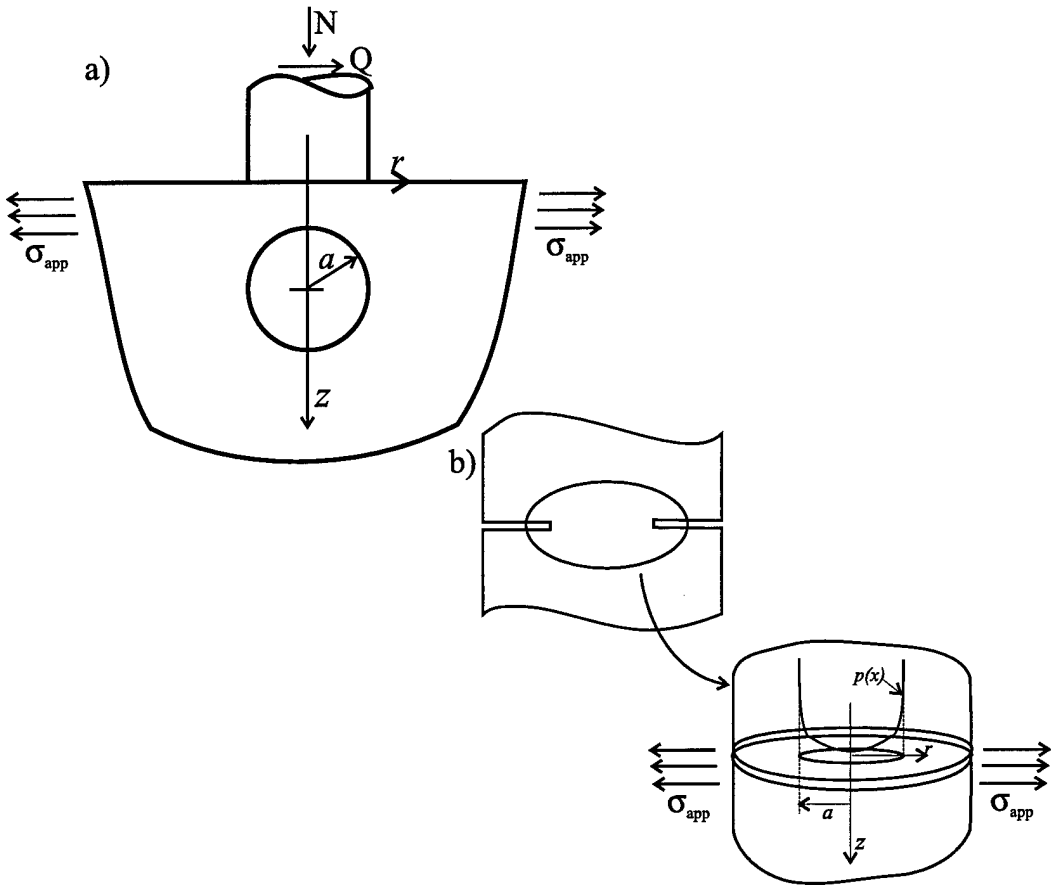

Figure 7-3: a) A cylindrical punch contacting a planar substrate and b) its crack analogue, a circumferentially cracked cylindrical rod.

Following initiation of a crack in the contact region due to contact loads, its advance will be controlled by the amplitudes of local stress intensity factors, Δk_1 and Δk_2, which are related to the remote K_{I} and K_{II}, respectively, by (c.f. Cotterell and Rice 1980):

$$k_1 = a_{11}(\phi)K_{\mathrm{I}} + a_{12}(\phi)K_{\mathrm{II}}$$
$$k_1 = a_{21}(\phi)K_{\mathrm{I}} + a_{22}(\phi)K_{\mathrm{II}}. \qquad (7.5a)$$

The dimensionless parameters to a first approximation in ϕ for the infinitesimal kink

are

$$a_{11}(\phi) = \frac{1}{4}\left(3\cos\frac{\phi}{2} + \cos\frac{3\phi}{2}\right),$$
$$a_{12}(\phi) = -\frac{3}{4}\left(\sin\frac{\phi}{2} + \sin\frac{3\phi}{2}\right),$$
$$a_{21}(\phi) = \frac{1}{4}\left(\sin\frac{\phi}{2} + \sin\frac{3\phi}{2}\right),$$
$$a_{22}(\phi) = \frac{1}{4}\left(3\cos\frac{\phi}{2} + \cos\frac{3\phi}{2}\right). \qquad (7.5b)$$

Equations 7.5 show that k_1 arises from K_{II}. The influence of local contact loads that provide a large Δk_1 to advance the crack rapidly after its initiation rapidly diminish as the crack grows out of the local contact stress fields. At a distance l_c (see Figure 7-3 for a schematic representation), the crack will tend to reorient itself normal to the applied cyclic stress (σ_{app}). If at l_c the applied cyclic loads create a tensile opening stress intensity factor greater than the effective mode I threshold stress intensity factor (ΔK_{th}), the crack will change direction[3] and continue growing in mode I, perpendicular to σ_{app}. If not, the crack will arrest.

Fretting of the dovetail fitting at the attachment of an aircraft engine turbine blade to the disk is amenable to analysis using the crack analogue approach. It is a complex biaxial loading condition accompanied by cyclic bulk loading. These characteristics may be accommodated by combining mode I and mode II solutions and incorporating the T-stress, respectively, in the present approach. Several experimental studies of the onset and progression of cracks near the fretting contact region are available for various engineering alloys (including Ti-Al alloys; see Antoniou and Radtke 1997), and Giannakopoulos et al. have shown that the crack analogue approach exhibits good agreement with this experimental data.

7.3 Life prediction methodology

The final outcome of the application of the crack analogue approach to fretting fatigue is the development of a life prediction methodology. Giannakopoulos et al. (1998)

[3]The change in orientation would actually occur gradually over a finite distance.

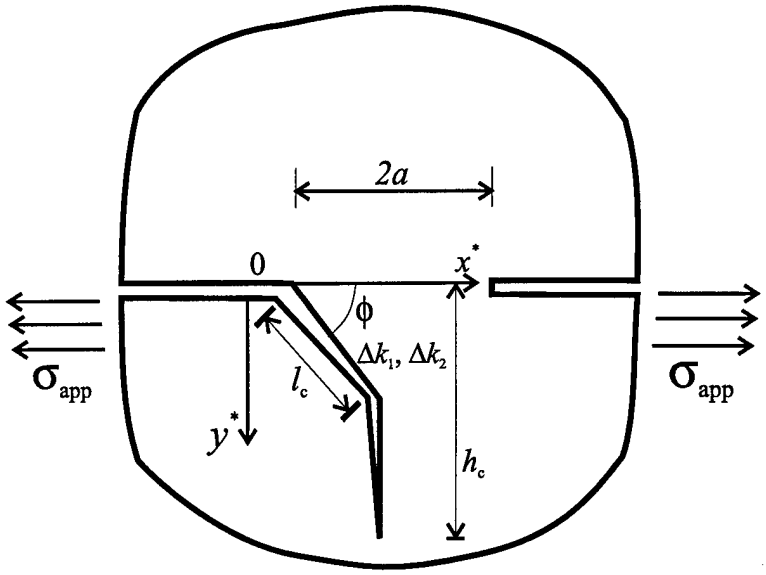

Figure 7-4: Analysis of cracking patterns in fretting fatigue using the crack analogue model. A surface crack initiates at an angle ϕ to the contact surface, advancing a distance l_c. With sufficient applied stresses (σ_{app}), the crack will reorient itself normal to the applied load and penetrate to a depth h_c, whereupon catastrophic failure ensues.

accomplish this by dividing the crack growth process into two stages:

- Stage I: A surface crack initiates under contact loads at an angle ϕ to the contact surface. It grows until reaching a critical length l_c.
- Stage II: The crack has oriented itself normal to σ_{app}, and this cyclic stress controls further crack growth.

Initial crack growth is postulated to occur along a direction for which the local mode II stress intensity factor vanishes, and the Paris law will describe this regime as

$$\frac{\mathrm{d}l}{\mathrm{d}N} = C_1(\Delta k_1)^{m_1}, \tag{7.6}$$

where C_1 and m_1 are material constants representative of the growth of small surface flaws and the local mixed mode loading conditions, and l is the instantaneous crack length measure along its initial growth plane.

Stage II crack growth is characterized by

$$\frac{\mathrm{d}l}{\mathrm{d}N} = C_2(\Delta k_1)^{m_2} = C_2\left(1.12\Delta\sigma_{\mathrm{app}}\sqrt{\pi l}\right)^{m_2}, \tag{7.7}$$

with C_2 and m_2 empirical constants representative of the growth of a long edge crack in the substrate material from an initial length $l = l_c \sin\phi$ to a final length h_c.

The total life to failure then consists of two parts, N_1 and N_2, corresponding to near-surface flaw propagation in stage I and mode I crack growth due to $\Delta\sigma_{\mathrm{app}}$ in stage II. N_1 refers to the number of oscillations of the punch on the substrate, while N_2 is the number of applied stress oscillations; neither frequency is necessarily dependent on the other. Eqs. 7.6 and 7.7 may be integrated to determine N_1 and N_2:

$$N_1 = \int_0^{l_c} \frac{\mathrm{d}l}{C_1\left(\Delta k_1\right)^{m_1}} \approx \frac{l_c}{C_1\left(\Delta k_1\right)^{m_1}} \tag{7.8a}$$

$$\begin{aligned} N_2 &= \int_{l_c\sin\phi}^{h_c} \frac{\mathrm{d}l}{C_2\left(1.12\Delta\sigma_{\mathrm{app}}\sqrt{\pi l}\right)^{m_2}} \\ &= \frac{1}{C_2\left(1.12\Delta\sigma_{\mathrm{app}}\sqrt{\pi}\right)^{m_2}} \cdot \left(\frac{2}{m_2-2}\right) \cdot \left[\left(l_c\sin\phi\right)^{(2-m_2)/2} - h_c^{(2-m_2)/2}\right], m_2 \neq 2 \\ &= \frac{1}{C_2\left(1.12\Delta\sigma_{\mathrm{app}}\sqrt{\pi}\right)^{2}} \cdot \ln\frac{h_c}{l_c\sin\phi}, m_2 = 2. \end{aligned} \tag{7.8b}$$

If $\nu_{1,\mathrm{c}}$ and $\nu_{2,\mathrm{c}}$ are the cyclic frequency of pad oscillations and the cyclic frequency of applied stress, respectively, total time to failure (t_{f}) for a fretting fatigue condition is given by

$$t_{\mathrm{f}} = t_{\mathrm{inc}} + \frac{N_1}{\nu_{1,\mathrm{c}}} + \frac{N_2}{\nu_{2,\mathrm{c}}}, \tag{7.8c}$$

where t_{inc} is the incubation period required to initiate a surface crack described adequately by C_1 and m_1. For a conservative life estimate, this term may be neglected, as it is difficult to know the loading history of any given component, making it almost impossible to know the probability that a crack will nucleate in it within a given time increment.

7.4 Recommendation

The reasonable inspection scheme to develop based on this approach is one that refurbishes components subject to fretting fatigue at intervals that are shorter than the predicted life. Complexity of the problem may be exacerbated by LCF damage occurring at engine spin-up at the beginning of sorties, e.g., but the potential usefulness of this life prediction methodology remains high, and further determination of loading conditions and material properties that will allow its full implementation as the basis for an inspection scheme merit further investigation.

Chapter 8

Conclusions, Recommendations, and Future Work

8.1 Conclusions

A three-pronged approach to the problem of fretting fatigue is offered in this work. The first is a quantitative approach that assumes fretting contact may be approximated by a sphere-plane geometry, and utilizes the known contact mechanics solutions for the stress fields associated with this type of contact. Fretting failure maps have been constructed that may be used to predict whether a given sphere-plane fretting fatigue loading condition will result in catastrophic failure. They are based on a modified Crossland criterion that incorporates the amplitude of the second invariant of the stress deviator and the maximum hydrostatic stress. Use of the Crossland criterion as calculated using the ratio $Q/\mu N$ and the appropriate value of friction coefficient yields fail/no-fail predictions that compare favorably with experimentation.

The second approach is a computationally intensive model that calculates quantities that may not easily be found using analytical means. A finite element model of sphere-plane fretting contact has been utilized to predict the accumulation of equivalent plastic strains during a fretting cycle. This information may be used to predict life in fretted components via a Coffin-Manson-type relation. Comparison of this method to experimental data has shown it to be an overly conservative method; improvement

is likely if the accumulation of plastic strain during fatigue cycles subsequent to the first cycle is monitored and used in the Coffin-Manson life model.

The third aspect of this work is experimental. The design, construction, and use of an improved fixture for performing fretting tests have been described. The apparatus permits use of varied contact pad geometries, and allows precise control and measurement of key fretting parameters. Of particular note is that both tangential loads and relative displacements may be accurately controlled and measured *in situ.* Various methods of measuring the friction coefficient over a fretting contact surface are provided. The performance of the apparatus has been verified through the creation of fretting scars with dimensions that closely match theoretical predictions, as well as through fretting fatigue tests.

For completeness, a review of the crack analogue approach used in adapting LEFM principles to the contact mechanics associated with fretting fatigue is included, along with a related life prediction methodology. This technique is another promising analytical development that has become available recently.

8.2 Recommendations

All of the approaches to the study of fretting fatigue in military aircraft components described here merit further study to evaluate their level of agreement with collected experimental data. The crack analog approach offers promise as an aspect of design criteria for components subject to HCF damage. Experimental work should continue, particularly using specimens made of the alloy Ti-6Al-4V, which is of interest because it is commonly used in the early fan stages of the F-100 turbofan engines utilized in many military jet aircraft.

8.3 Future work

Utilization of the **analytical** computer programs created in this work should continue as a means of determining experimental conditions, i.e. stress fields due to contact,

bulk stresses, maximum tangential contact forces, and expected relative displacements, prior to conducting tests. Comparison of experimental data to the Crossland parameter maps will be useful for verification of the approach as a viable approach to component design.

Further **computational** fretting simulation using the finite element model of Giannakopoulos and Suresh (1997) is necessary. These tests should serve to monitor the accumulation of plastic strains due to fretting contact in several regimes of contact-induced plasticity, elastic shakedown, and fully reversed elasticity as described by Ponter (1985). Comparison of the Coffin-Manson relation-based life prediction method should be compared with experimental results. In particular, the plastic strain increment should be obtained for fretting cycles subsequent to the first cycle, or preferably, the second cycle. This value will be closer to the actual steady-state value, and will perhaps lead to more accurate use of the Coffin-Manson relation as a life prediction method for fretting in the context of HCF damage.

In the course of this work, several Ti-6Al-4V specimens and fretting pads have been created. These should soon be tested in the **experimental** frame. New experiments should:

- Attempt to determine the deleterious effects of fretting on plain fatigue life of Ti-6Al-4V.

- Undertake and refine the use of fretting pads of non-spherical geometries for conducting fretting tests. Of particular interest will be overcoming the problem of 'gouging' with sharp-edged geometries. A first measure to overcome this difficulty may be utilizing flat punches with rounded edges.

- Observe the orientation, change in growth angle, and critical failure length of cracks nucleated from fretting scars. This data will be of use in determining the usefulness of the **crack analogue** method as a life prediction technique for fretting fatigue.

Appendix A

Finite Element Results

This appendix contains graphical output of interest from the finite element model.

A.1 Nature of the model

Figure A-1 shows the 3D nature of the model by displaying magnified displacement fields for a typical fully elastic contact condition.

A.2 Elastic finite element results

Figures A-2 through A-5 demonstrate the results obtained from the finite element model for completely elastic simulations. The equivalent von Mises stresses in these simulations never approach the material yield strength, making consideration of plastic yielding unnecessary. Observe that the maximum von Mises equivalent stress ($\bar{\sigma}$) occurs beneath the surface at a depth of one-half the contact radius for normal contact, but transitions to the trailing edge of contact for tangential sliding with a coefficient of friction of 0.3 and above.

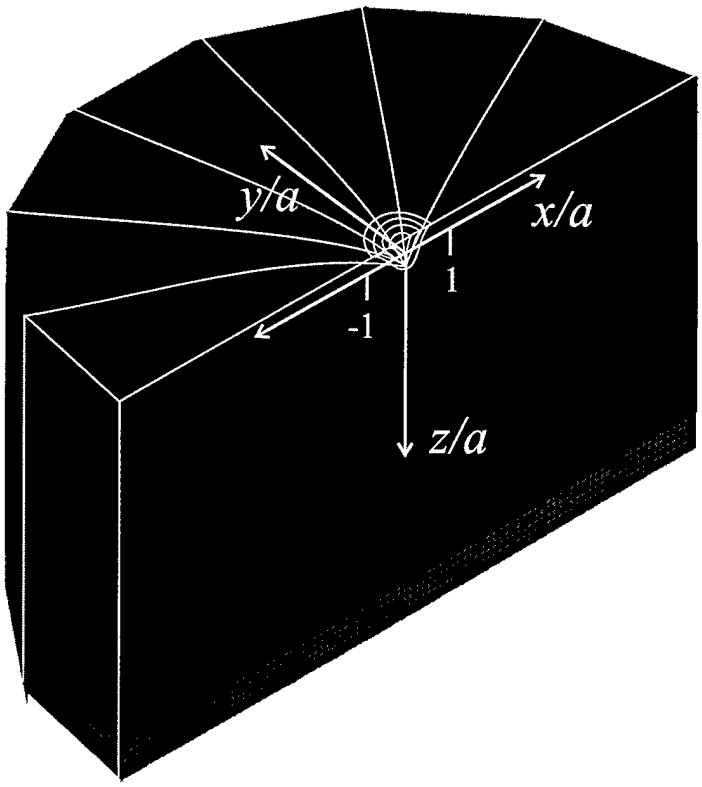

Figure A-1: A depiction of the displacement fields (magnified 75× relative to the scale of the picture) created for one case of normal contact, showing the 3D nature of the finite element model. Axes coordinates are normalized by contact radius, so that -1 and 1 on the x/a axis define the contact zone.

A.3 Plastic finite element results

Figure A-6 shows simulation ouputs for fretting contact cases modeled with the potential to exhibit plastic yielding; in (*a*) are the von Mises equivalent stresses for an aluminum substrate subject to a normal load such that the maximum stress level is slightly above the material yield strength. Part (*b*) shows the equivalent plastic strains for the corresponding loading case. Note that the maximum plastic strains correspond to the location of maximum von Mises equivalent stress, and that no plasticity occurs at the surface.

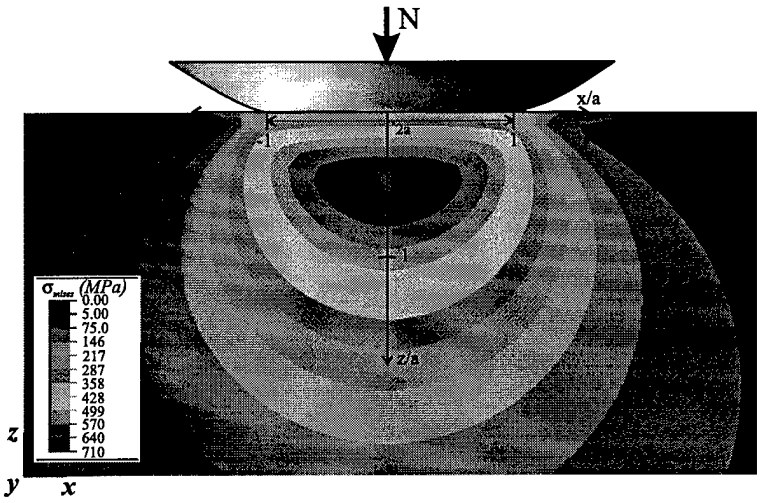

Figure A-2: Von Mises equivalent stress ($\bar{\sigma}$) for normal loading of a Ti-6Al-4V substrate by a sphere such that $\bar{\sigma}$ is well below σ_y.

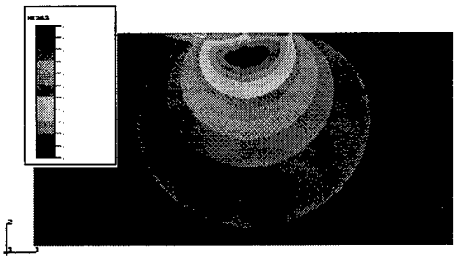

Figure A-3: Von Mises equivalent stress ($\bar{\sigma}$) for the loading case in Fig. A-2; the sphere has been slid to the maximum elastic sliding displacement, with $\mu = 0.3$. The maximum von Mises stress is located at the trailing edge of contact; μ of 0.3 and above will always result in a transition of the maximum von Mises stress from below the surface to the surface for sliding sphere-plane contact.

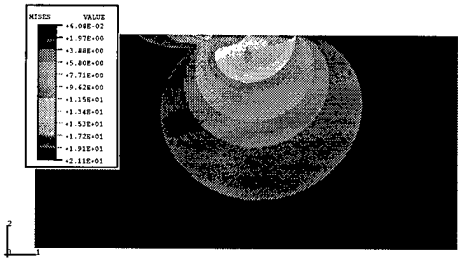

Figure A-4: Von Mises equivalent stress ($\bar{\sigma}$) for the loading case in Fig. A-2; the sphere has been slid to the maximum elastic sliding displacement, with $\mu = 0.5$. The maximum von Mises stress location (and its shift away from beneath the center of contact) is more pronounced.

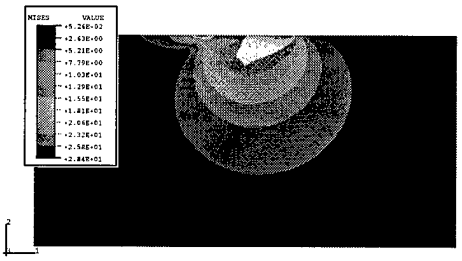

Figure A-5: Von Mises equivalent stress ($\bar{\sigma}$) for the loading case in Fig. A-2; the sphere has been slid to the maximum elastic sliding displacement, with $\mu = 0.7$. The trend observed in Figures A-3 and A-4 continues.

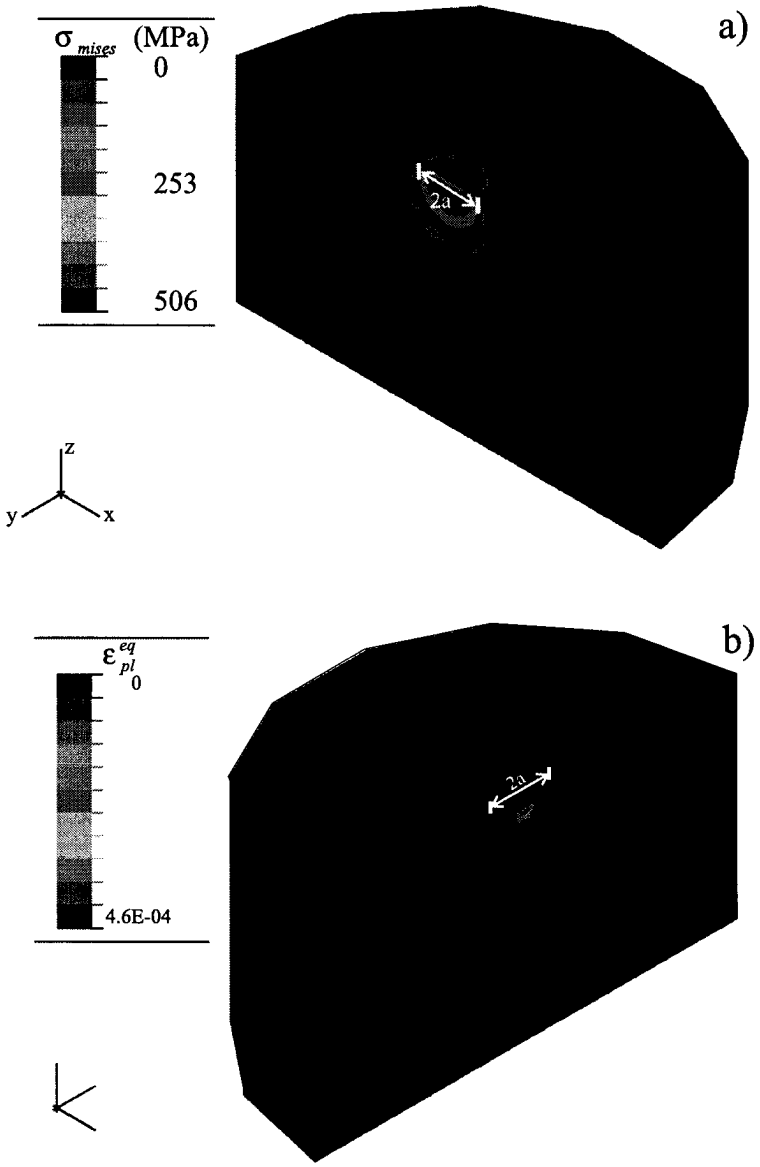

Figure A-6: Showing a) von Mises equivalent stress fields for the normal loading of an Al 7075-T6 substrate by a sphere of the same material such that $\bar{\sigma}$ is slightly above σ_y and b) equivalent plastic strains for the same loading condition.

Appendix B

Experimental Protocol

This appendix describes details relevant to conducting successful fretting tests using the experimental apparatus. It is intended as a reference for those who will in the future make use of the fixture for their own fretting tests.

B.1 Test frame materials

The choices for all materials used in construction of the fretting frame were based compliance and weight considerations. The choice of thick (12.7 mm) hot-rolled steel for construction of the base was driven by the desire for a very stiff frame that would not deform appreciably under the loading it would experience. The same characteristics were sought for the the adjustable points of support. The springs were chosen to have a high enough spring constant to exert the desired range of loads with an equilibrium displacement of not more than 20 mm; they are of a typical spring steel. The flexible plates are of cold-rolled steel on the order of 1.6 mm thick. The stiff plate is made from a high-strength aluminum alloy, as are the linear bearing housings. Both these components are in motion throughout the test, and it is desirable for them to have low masses to minimize intertial effects. The pad support cylinders are of a low-carbon steel; a better altenative would be an aluminum alloy of lesser density, again because of the potential intertial effects of moving parts. The compliant member sometimes used in the load train may be of many materials, as its weight does not

affect the tests, but it is thin (with a radius approximately twice that of a specimen's radius) and made of low-carbon steel for the tests described in this work. A schematic of the basic fretting test frame is shown in Figure B-1.

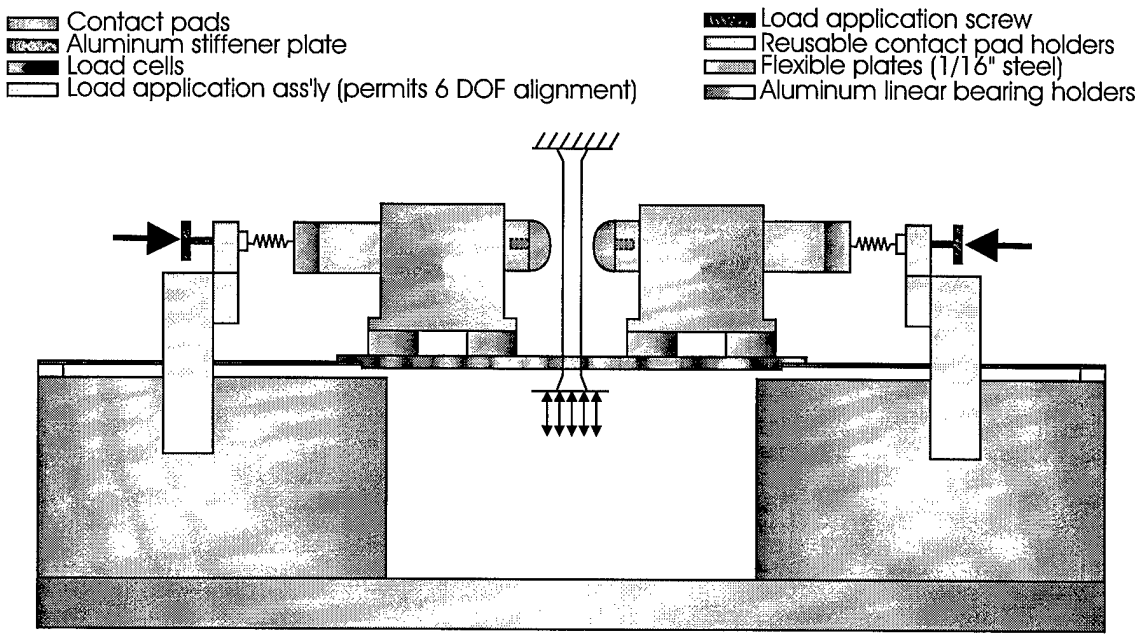

Figure B-1: Fretting test frame schematic

Although it is not shown in the schematic, the compliant member that may be included in the load train during testing is shown in Figure B-2, a photograph of the entire experimental assembly.

B.2 Fretting specimens and pads

The fretting specimens used are typical cylindrical uniaxial test specimens with parallel flat surfaces in the gage section. They are shown in Figure B-3. Note that the gage length may be varied for experimental convenience. For example, in the case of aluminum alloy specimens, a gage length of 15.2 cm was most typically utilized because it gave a broader range of possible specimen compliance and allowed easy installation of the extensometer. Fretting pads are machined from cylindrical stock (if available), and have one flat end and one end machined with a specified radius of curvature. These are shown in Figure B-4.

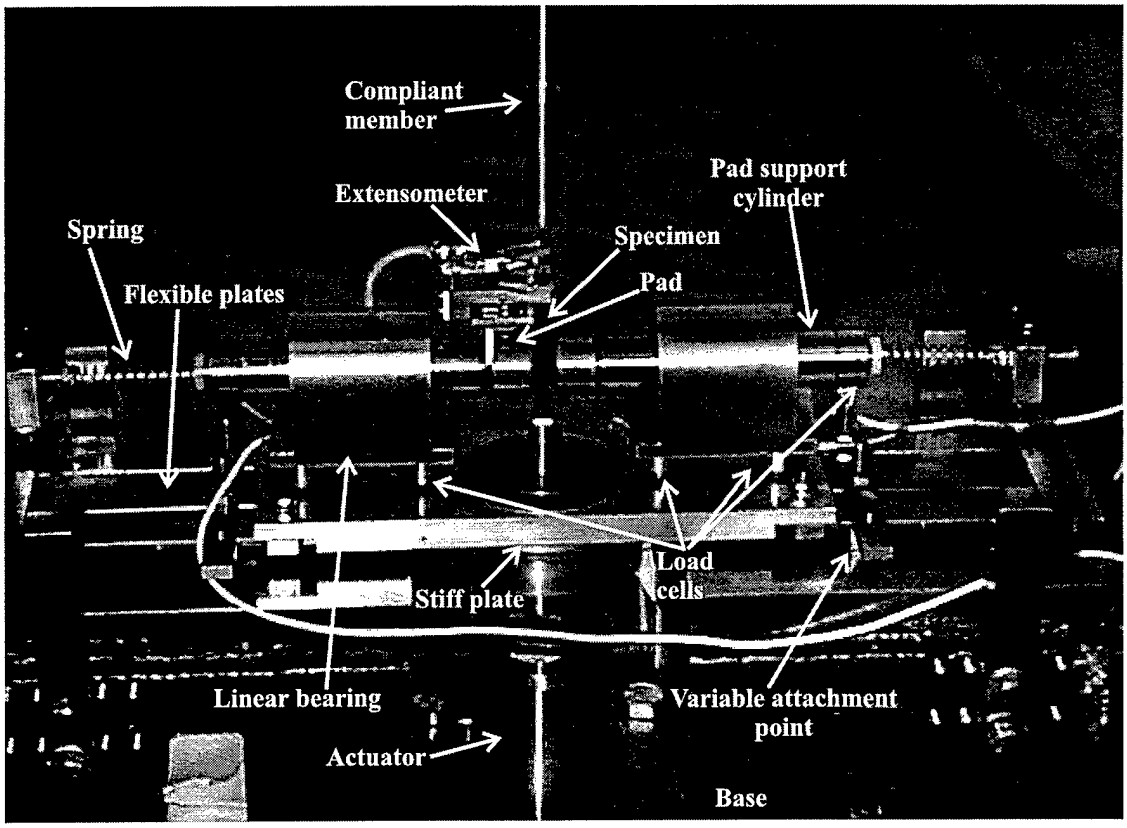

Figure B-2: Photograph of entire test frame.

The hatched regions shown in Figure B-4 correspond to those regions which are chemically milled to achieve final surface finish (if chem-milling is used for a particular set of specimens). For the specimens, use of chem-milling implies that both sides of the gage section are treated.

B.3 Specimen and pad preparation

The properties of the alloys selected for testing are shown in Tables 4.1 and 4.2. A major factor in the selection of an aluminum alloy for fixture refinement and testing lies in the cost of material and preparation. Machining and chem-milling costs alone for the 11 fretting specimens and 24 pads created were approximately $ 11,000. A batch of about one dozen 7075-T6 specimens and corresponding pads can be procured for under $ 500.

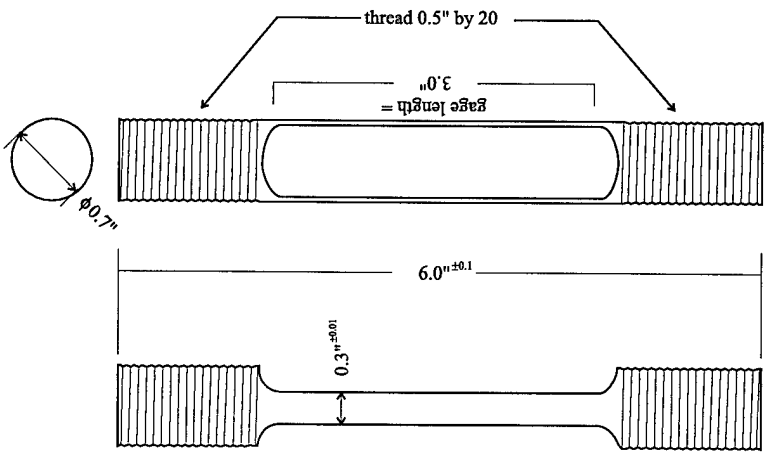

Figure B-3: Fretting fatigue test specimens

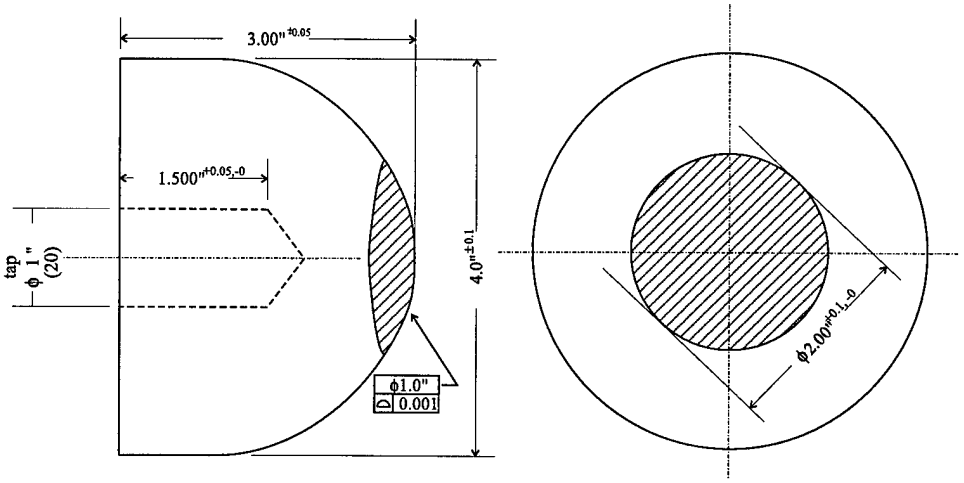

Figure B-4: Spherical fretting pads

The Ti-6Al-4V specimens and pads created (but not yet utilized) for this effort were manufactured in accordance with the standard procedures prescribed for work in the context of the Multi-University Research Initiative (MURI) on "High-Cycle Fatigue," Air Force Office of Scientific Research Grant No. F49620-96-1-0478. A forging of raw material was requested for release from the University of Dayton Research Institute (UDRI). Metcut Research, Inc. was the primary contractor for machining and assumes responsibility for adherence to final specifications. Specimens were machined in accordance with GE document number RP1055-S, which specifies vacuum stress relief after machining and chem-milling to achieve final surface finish. Vacuum stress relief and chem-milling were accomplished by outside subcontractors to Metcut, Inc.

Although the threaded sections of existing specimens were not properly masked during the chem-milling process, resulting in visible discolorization of parts of the surface, the specified tolerances were achieved, and the specimens are acceptable for testing without further modification.

Machining of the aluminum specimens and pads was accomplished at the MIT Central Machine Shop. Pads and specimens are received with a #4 finish. Both of the flat sides of the specimen gage length and pads are subsequently polished by hand prior to testing. A steel bar, approximately 46 cm×38 mm×12.7 mm is tightly wrapped at one end with a 102 mm×12.7 mm piece of polishing medium. A pivot point is created at the opposite end of the bar by wrapping masking tape around a ball of paper. The section of the wide (38 mm) side of the bar with polishing medium on its surface is used for polishing. The steel bar holds the polishing medium flat against the surface of the specimen, ensuring that planarity of the gage section faces is maintained.

The polishing media used are 800-, 1200-, 2400-, and 4000-grit abrasive papers, followed by a suspension of 0.3 μm alumina (Al_2O_3) in ethanol. The suspension is poured onto pieces of cotton, which may be wrapped around the steel bar in the same manner as the sandpaper. Aprroximately 200 polishing strokes per side are done for each polishing step. Periodic rinsing of the specimen surface and polishing surface is done with water for all steps involving abrasive papers. Ethanol is used before and during polishing with the alumina suspension.

Pads are prepared using the same number of polishing steps as specimens. Polishing media are supported by several layers of soft cloth, which permits them to conform to the surface contour of the pads as they are polished. Polishing motion is in a circular direction, and the polisher should rotate the pad in his hand periodically to ensure uniform coverage, as well as checking the surface visually. Uniform polishing of pads is of paramount importance in keeping radial dimensions intact.

Both specimens and pads are cleaned ultrasonically for 5–10 minutes after polishing is completed to remove residual alumina and other debris. Surfaces are checked for uniform surface finish using an optical microscope, and should have a mirror finish

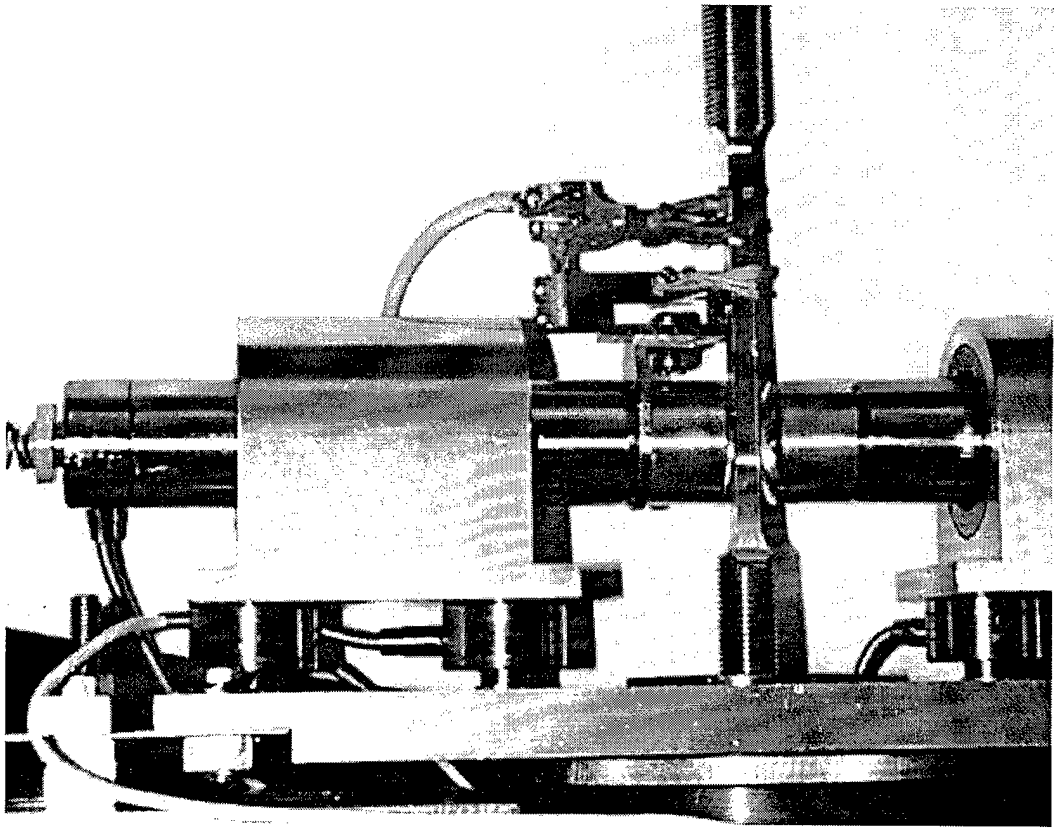

Figure B-5: Close-up of half of the experimental apparatus, showing the extensometer assembly and attachments.

to the naked eye.

Appendix C

Fretting Scars

This appendix shows and describes selected fretting scars produced during experiments. Tests are referred to by the labels given in table 6.1. FigureC-1 shows how the buildup of fretting wear debris may obscure a fretting scar after its initial removal from the fretting fixture. Subsequent ultrasonic cleaning removes this debris and reveals the true characteristics of the scar.

Figure C-2 shows a fretting scar resulting from a stick-slip contact condition. In contrast to Figure 6-1, the annulus of microslip for this case is large, so that the dimension c is less than $\frac{1}{2}a$.

Figure C-3 shows both sides of a single specimen (for test K). The right side of the specimen developed a crack that advanced from the contact perimeter to the edges of the specimen. However, the crack was stable under bulk loading conditions, and the test was stopped prior to catastrophic failure. Specimens such as these may be used to determine crack initiation and propagation angles, which are useful for verification of the crack analogue method of fretting fatigue life prediction.

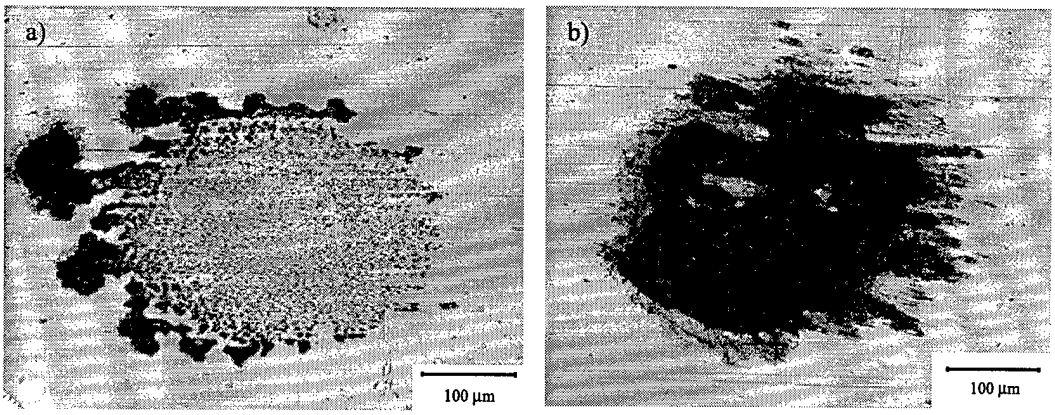

Figure C-1: A fretting scar from the test G specimen, a) before and b) after ultrasonic cleaning.

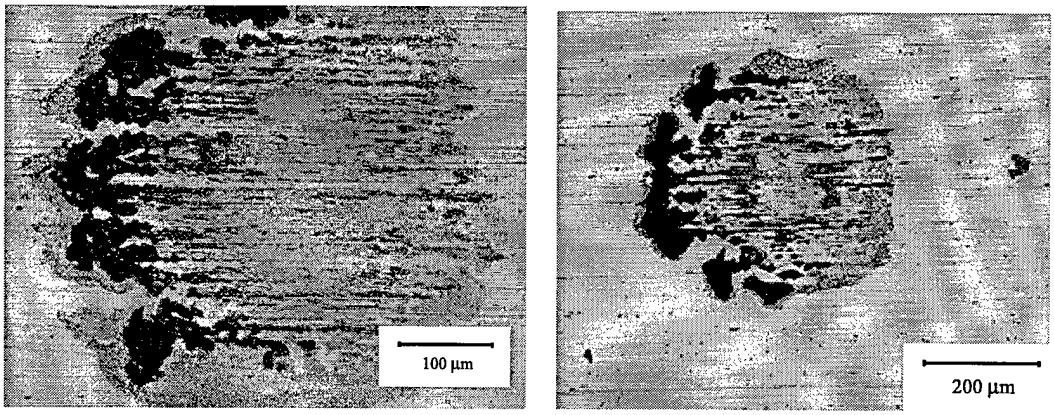

Figure C-2: Both a) and b) show micrographs of a fretting scar on the left side of the test H specimen. The stick and microslip zones are easily evident in spite of the fact that this specimen experienced more than 10^7 fatigue cycles.

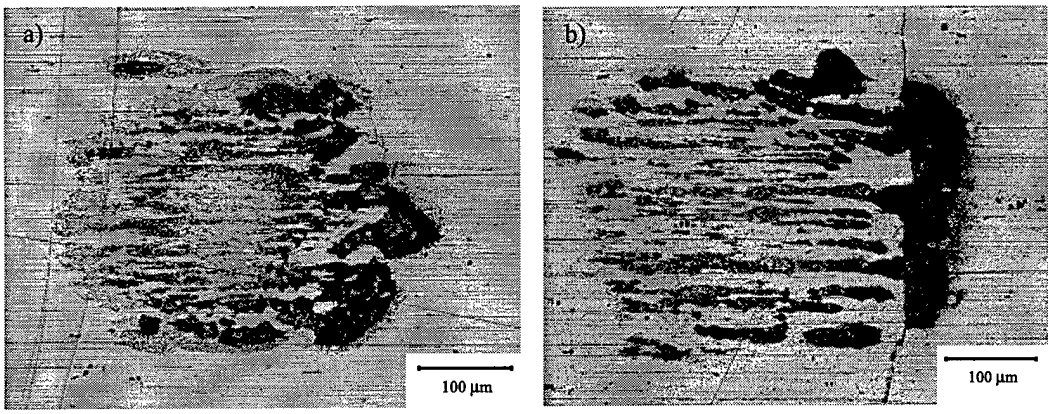

Figure C-3: Showing a) the left side of the specimen used in test K and b) the right side of the same specimen (where a crack is visible).

Bibliography

[1] Adibnazari, S. & Hoeppner, D.W. A fretting fatigue normal pressure threshold concept. *Wear*, **160**, 33–35.

[2] Alic, J.A., Hawley, A.L., & Urey, J.M. (1979) Formation of fretting fatigue cracks in 7075-T7351 aluminum alloy. *Wear*, **56**, 351–361.

[3] Almen, J.O. (1937) Lubricants and false brinelling of ball and roller bearings. *Mechanical Engineering*, **59**, 415.

[4] Anton, D.A. et al. (1997) Demonstration of fretting fatigue test apparatus with biaxial control, United Technologies Research Center, Hartford CT, March 1997.

[5] Antoniou, R.A. & Radtke, T.C. (1997) *Materials Science and Engineering*, **A237**, 229.

[6] *Symposium on fretting corrosion* (1952), *ASTM STP 144*, ASTM, Philadelphia, USA.

[7] Attia, M.H. & D'Silva, N.S. (1985) Effect of mode of motion and process parameters on the prediction of temperature rise in fretting wear. *Wear*, **106**, 206–224.

[8] Attia, M.H. & Ko, P.L. (1986) On the thermal aspects of fretting wear-temperature measurements in the subsurface layer. *Wear*, **111**, 363–376.

[9] Beard, J. (1982) An investigation into the mechanism of fretting fatigue. *Ph.D. Thesis*, University of Salford.

[10] Berthier, Y., Colombie, C., Vincent, L., & Godet, M. (1987) Fretting wear mechanisms and their effects on fretting fatigue. *ASLE/ASME Tribology Conference*, ASME, USA.

[11] Blanchard, P., Colombie, C., Pellerin, V., Fayeulle, S. and Vincent, L. (1991) Material effects in fretting wear: application to iron, titanium and aluminum alloys. *Metallurgical Transactions*, **22A**, 1535–1544.

[12] Bramhall, R. (1973) Studies in fretting fatigue. DPhil thesis, Oxford University.

[13] Brown, S.A. & Merritt, K. (1981) Fretting corrosion in saline and serum. *Journal of Biomedical Materials Research*, **15**, 479–488.

[14] Bryggman, U. & Söderberg, S. (1986) Contact conditions in fretting. *Wear*, **110**, 1–17.

[15] Bryggman, U. and Söderberg, S. (1988) Contact conditions and surface degradation mechanisms in low amplitude fretting. *Wear*, **125**, 39–52.

[16] Campbell, W.E. & Thomas, U.B. (1938) Films on freshly abraded copper surfaces. *Nature*, **142**, 253.

[17] Campbell, W.E. (1939) Studies in boundary lubrication. *Transactions of the American Society for Mechanical Engineers*, **61**, 633.

[18] Cattaneo, C. (1938) Sul contatto di due corpi elastici. *Accademia dei Lincei, Rendicotti, Series 6*, **27**, 342–348, 434–436, and 474–478.

[19] Coffin, L.F. (1960) Stability of metals under cyclic plastic strains. *Transactions of the ASME, Journal of Basic Engineering*, **82D**, 671–682.

[20] Colombie, C., Berthier, Y., Floquet, A., Vincent, L., & Godet, M. (1984) Fretting: Load carrying capacity of wear debris. *Transactions of the ASME*, **106**, 194.

[21] Colombie, C., Berthier, Y., Vincent, L., & Godet, M. (1986) How to choose coatings in fretting. *Conference: advances in surface treatments, technology applications, and effects*, Pergamon Press, UK, 321–334.

[22] Comyn, R.H. & Furlani, C.W. (1963) *Fretting corrosion — a literature survey*, United States Army Material Command, Harry Diamond Laboratories, Washington.

[23] Cook, S.D., Gianoli, G.J., Clemow, A.J.T., & Haddad, J.R. (1983) Fretting corrosion in orthopaedic alloys, *1 Biomat., Med., Dev., Art. Org.*, **11**, 281–292.

[24] Cotterell, B. & Rice, J.R. (1980) *International Journal of Fracture*, **16**, 155.

[25] Cottrell, A.H. (1964) *Theory of Crystal Dislocations.* New York: Gordon and Breach.

[26] Cowles, B.A. (1996) High cycle fatigue in aircraft gas turbine engines – an industry perspective. *International Journal of Fracture*, **80**, 147–163.

[27] Dang Van, K. Sur las résistance à la fatigue des métaux. Thèse de Doctorat ès Sciences, *Sci. Techniq. l'Armement*, **47**, 647.

[28] Del Puglia, A., Pratesi, F., & Zonfrillo, G. (1994) Experimental procedure and parameters involved in fretting fatigue tests. *Fretting Fatigue*, ESIS 18. R.B. Waterhouse & T.C. Lindley, eds., London: Mechanical Engineering Publications, 219–238.

[29] Dobromirski, J. & Smith, I. (1987) Metallographic aspects of surface damage, surface temperature and crack initiation in fretting fatigue. *Wear*, **117**, 347–357.

[30] Doeser, B. (1981) The study of fretting fatigue using finite element analysis and electron microscopy. PhD Thesis, Nottingham University.

[31] Eden, E.M., Rose, W.N., & Cunningham, F.L. (1911) The endurance of metals. *Proceedings of the Institution for Mechanical Engineers*, **4**, 839–974.

[32] Edwards, P.R. (1981) The application of fracture mechanics to predicting fretting fatigue. In *Fretting fatigue*, R.B. Waterhouse, ed., London: Elsevier Applied Science Publishers, 67–99.

[33] Endo, K., Goto, H., & Nakamura, T. (1969) Effects of cycle frequency on fretting fatigue life of carbon steel. *Bulletin of the JSME*, **12**, 1300–1308.

[34] Endo, K., Goto, H., & Fukunaga, T. (1974) Behaviors of frictional force in fretting fatigue. *Bulletin of the JSME*, **17**, 647–654.

[35] Endo, K. & Goto, H. (1976) Initiation and propagation of fretting fatigue cracks. *Wear*, **38**, 311–324.

[36] Evans, U.R. & Miley, H.A. (1931) Measurements of oxide films on copper and iron. *Nature*, **139**, 283.

[37] Feng, I-Ming & Rightmire, B.G. (1952) The mechanism of fretting. Massachusetts Institute of Technology, Cambridge, MA, AD 4463.

[38] Fenner, A.J. & Field, J.E. (1960) A study of the onset of fatigue damage due to fretting. *Proceedings N.E. Coast Institute of Engineers and Shipbuilders*, **76**, 183.

[39] Forsyth, P.J.E. (1981) Occurrence of fretting fatigue failures in practice. In *Fretting Fatigue*, R.B. Waterhouse, ed., London: Elsevier Applied Science Publishers, 99–125.

[40] Fouvry, S., Kapsa, Ph., and Vincent, L. (1995) Analysis of sliding behavior for fretting loadings: determination of transition criteria. *Wear*, **185**, 35–46.

[41] Frost, N.E., Marsh, K.J., and Pook, L.P. (1974) *Metal Fatigue*, Clarendon Press, Oxford.

[42] Fuchs, H.O. & Stephens, R.I. (1980) *Metal Fatigue in Engineering*, John Wiley and Sons, New York.

[43] Gaul, D.J. & Duquette, D.J. (1980*a*) The effect of fretting and environment on fatigue crack initiation and early propagation in a quenched and tempered 4130 steel. *Metallurgical Transactions A*, **11A**, 1555–1561.

[44] Gaul, D.J. & Duquette, D.J. (1980*b*) Cyclic wear behavior (fretting) of a tempered martensite steel. *Metallurgical Transactions A*, **11A**, 1581–1588.

[45] Giannakopoulos, A.E., Lindley, T.C., & Suresh, S. (1998) Aspects of equivalence between contact mechanics and fracture mechanics: theoretical connections and a life-prediction methodology for fretting fatigue. *Acta Materialia, in press.*

[46] Giannakopoulos, A.E. & Suresh, S. (1998) A Three-Dimensional Analysis of Fretting Fatigue. *Acta Materialia et Metalurgica*, **46**, 177–192.

[47] Godfrey, D. (1950) Investigation of fretting corrosion by microscopic observation. NACA Technical Note 2039.

[48] Gordelier, S.C. & Chivers, T.C. (1979) A literature review of palliatives for fretting fatigue. *Wear*, **56**, 177–190.

[49] Griffith, A.A. (1921) The phenomenon of rupture and flow in solids. *Philosophical Transactions of the Royal Society, London*, **A221**, 163–197.

[50] Hamilton, G.M. & Goodman, L.E. (1966) The stress field created by a sliding circular contact. *Journal of Applied Mechanics*, **88**, 371–376.

[51] Hamilton, G.M. (1983) Explicit equations for the stresses beneath a sliding spherical contact. *Proceedings of the Institution of Mechanical Engineers*, bf 197C, 53–59.

[52] Harris,W.J. (1974) *AGARD Conference Proceedings AGARD-CP-161*, Session III, Paper 7.

[53] Hattori, T., Nakamura, M., Sakata, H., & Watanabe, T. (1988) Fretting fatigue analysis using fracture mechanics. *JSME International Journal I*, **31**, 100–107.

[54] Hertz, H. (1882) On the contact of elastic solids. *J. Reine und Angewandte Mathematik*, **92**, 156–171.

[55] Hills, D.A. and Nowell, D. (1992) The development of a fretting fatigue experiment with well-defined characteristics. *Standardization of Fretting Fatigue Test Methods and Equipment*, ASTM STP 1159, M. Helmi Attia and R.B. Waterhouse, eds. American Society for Testing and Materials, 69–84.

[56] Hills, D.A. & Nowell, D. (1994) *Mechanics of Fretting Fatigue.* Dordrecht, the Netherlands: Kluwer Academic Publishers.

[57] Hoeppner, D.W. (1974*a*) Fretting of aircraft control surfaces. *AGARD Conference Proceedings No. 161*, AGARD, Munich.

[58] Hoeppner, D.W. & Goss, G.L. (1974*b*) A fretting fatigue damage threshold concept. *Wear*, **27**, 175–187.

[59] Hoeppner, D.W. & Goss, G.L. (1974*c*) Metallographic analysis of fretting fatigue damage in Ti-6Al-4V MA and 7075-T6 aluminum. *Wear*, **27**, 175–187.

[60] Hoeppner, D.W. (1981*a*) Material/structure degradation due to fretting and fretting-initiated fatigue. *Canadian Aeronautics and Space Journal*, **27**, 213–221.

[61] Hoeppner, D.W. & Gates, F.L. (1981*b*) Fretting fatigue considerations in engineering design. *Wear*, **70**, 155–164.

[62] Hoeppner, D.W. (1994) Mechanisms of fretting fatigue. in *Fretting Fatigue*, ESIS 18. R.B. Waterhouse & T.C. Lindley, eds., London: Mechanical Engineering Publications, 3–19.

[63] Huber, M.T. (1904) On the theory of elastic solid contact. *Annln. Phys. Lpz.*, **14**, 153–163.

[64] Hurricks, P.L. (1970) The mechanisms of fretting — a review. *Wear*, **15**, 389–409.

[65] Hurricks, P.L. (1972) The fretting wear of mild steel from room temperature to 200 deg C. *Wear*, **30**, 189–212.

[66] Air Force Aircraft Jet Engine Manufacturing and Production Process, Report of the Ad Hoc Committee (1992), United States Air Force Scientific Advisory Board, SAF/AQQS, the Pentagon, Washington DC 20330-1000.

[67] Johnson, R.L. & Bill, R.C. (1974) *AGARD Conference Proceedings AGARD CP-161*, Session II, Paper 5.

[68] Johnson, K.L. (1985) *Contact Mechanics.* Cambridge: Cambridge University Press.

[69] Jørgensen, O. (1993) Ring-element analysis of layered orthotropic bodies. *Computational Methods of Applied Mechanical Engineering*, **2**, 319.

[70] Jørgensen, O., Giannakopoulos, A.E. & Suresh, S. (1997) *International Journal of Solids and Structures*, in press.

[71] Kantimathi, A. & Alic, J.A. (1981) The effect of periodic high loads on fretting fatigue. *Journal of Engineering Materials*, **103**, 218–225.

[72] Kapoor, A. (1994) A re-evaluation of the life to rupture of ductile metals by cyclic plastic strain. *Fatigue and Fracture of Engineering Materials and Structures*, **17**, 201–219.

[73] LabVIEW (1996) *User's Manual*, Version 4.0, National Instruments, Inc., Austin, TX.

[74] Lamacq, V., Dubourg, M.C. and Vincent, L. (1997) A theoretical model for the prediction of initial growth angles and sites of fretting fatigue cracks. *Tribology International*, **30**, 6, 391–400.

[75] Lindley, T.C. & Nix, K.J. (1985) The role of fretting in the initiation and early growth of fatigue cracks in turbo-generator materials. *Conference: multiaxial fatigue*, ASTM, Philadelphia, USA, 340–360.

[76] Mathematica (1992) *Mathematica: a System for Doing Mathematics by Computer*, Version 2.2, Wolfram Research, city??.

[77] McDowell, J.R. (1953) *American Society for Testing of Materials, Special Technical Publication 144*, p. 24.

[78] Mendelson, A., Hirschberg, M.H., & Manson, S.S. (1959) The stability of metals under cyclic plastic strain. *Transactions of the ASME, Journal of Basic Engineering*, **82D**, 671–682.

[79] McDiarmid, (1987) *Fatigue and Fracture of Engineering Materials and Structures*, **9**, 457–475.

[80] Milestone, W.D. (1970) Fretting and fretting fatigue in metal to metal contacts. *Proceedings AIAA Structural dynamics and materials conference*, Denver, 86.

[81] Milestone, W.D. & Janeczko, J.J. (1971) Friction between steel surfaces during fretting. *Wear*, **18**, 219–240.

[82] Mindlin, R.D. (1949) Compliance of elastic bodies in contact. *Journal of Applied Mechanics*, **71**, 259–268.

[83] Mindlin, R.D. & Deresiewicz, H. (1953) Elastic spheres in contact under varying oblique forces. *Journal of Applied Mechanics*, **75**, 327–344.

[84] Specialists' meeting on fretting in aircraft systems. (1974) NATO-AGARD conference proceeding No. 161, *AGARD*.

[85] Nicholas, T. & Zuiker, J.R. (1996) On the use of the Goodman diagram for high cycle fatigue design. *International Journal of Fracture*, **80**, 219–235.

[86] Nishioka, K., Nishimura, S., & Hirakawa, K. (1968) Fundamental investigation of fretting fatigue — part 1. On the relative slip amplitude of press-fitted axle assemblies. *Bulletin of the JSME*, **11**, 437–445.

[87] Nishioka, K. & Hirakawa, K. (1969*a*) Fundamental investigation of fretting fatigue — part 2. Fretting fatigue testing machine and some test results. *Bulletin of the JSME*, **12**, 180–187.

[88] Nishioka, K. & Hirakawa, K. (1969*b*) Fundamental investigation of fretting fatigue — part 3. Some phenomena and mechanisms of surface cracks. *Bulletin of the JSME*, **12**, 397–407.

[89] Nishioka, K. & Hirakawa, K. (1969*c*) Fundamental investigation of fretting fatigue — part 4. The effect of mean stress. *Bulletin of the JSME*, **12**, 408-414.

[90] Nishioka, K. & Hirakawa, K. (1969*d*) Fundamental investigation of fretting fatigue — part 5. The effect of relative slip amplitude. *Bulletin of the JSME*, **12**, 692-697.

[91] Nishioka, K. & Hirakawa, K. (1972) Fundamental investigation of fretting fatigue — part 6. *Bulletin of the JSME*, **15**, 135–144.

[92] Nix, K.J. & Lindley, T.C. (1985*a*) The application of fracture mechanics to fretting fatigue. *Fatigue and Fracture of Engineering Materials and Structures*, **8**, 143–160.

[93] Nix, K.J. & Lindley, T.C. (1985*b*) The initiation and propagation of small defects in fretting fatigue. *Conference: life assessment of dynamically loaded materials and structures*, Engineering Materials Advisory Services Limited, UK, 89–98.

[94] Nowell, D. (1988) An analysis of fretting fatigue. Doctor of Philosophy Thesis, Lincoln College, Oxford University, 1988.

[95] Nowell, D. & Hills, D.A. (1990) Crack initiation criteria in fretting wear. *Wear*, **136**, 329–343.

[96] O'Dowd, N.P. & Shih, C.F. (1991) *Journal of the Mechanics and Physics of Solids*, **39**, 989.

[97] Papadopoulos, I.V. (1987) Fatigue polycyclique des métaux: une nouvelle approche. Thèse de Doctorat, Ecole Nationale des Ponts et Chaussées, Paris.

[98] Papadopoulos, I.V., Davoli, P., Gorla, C., Filippini, M., & Bernasconi, A. (1997) A comparative study of multiaxial high-cycle fatigue criteria for metals. *International Journal of Fatigue*, **19**, 219–235.

[99] Paris, P.C., Gomez, M.P., & Anderson, W.P. (1961) A rational analytic theory of fatigue. *The Trend in Engineering*, **13**, 9–14.

[100] Peterson, R.E. & Wahl, A.M. (1935) Fatigue of shafts at fitted members, with a related photoelastic analysis. *Transactions of the American Society for Mechanical Engineers*, **57**, A-1.

[101] Ponter, A.R.S., Hearle, A.D., & Johnson, K.L. (1985) Application of the kinematical shakedown theorem to rolling and sliding point contacts. *Journal of the Mechanics and Physics of Solids*, **33**, 339–362.

[102] Poon, C.J. & Hoeppner, D.W. (1981) A statistically based investigation of the environmental and cyclic stress effects of fretting fatigue. *Journal of Engineering Materials*, **103**, 218–223.

[103] Repetto, E.A. & Ortiz, M. (1997) A micromechanical model of fatigue-crack nucleation in FCC metals. *Acta Metallurgica*, **45**, 2577–2595.

[104] Ravichandran, K.S. (1990) Fatigue crack growth behavior near threshold in Ti-6Al-4V alloy: microstructural aspects. *Fatigue 90*, 1345–1356.

[105] Ruiz, C., Boddington, P.H.B., & Chen, K.C. (1984) An investigation of fatigue and fretting in a dovetail joint. *Experimental Mechanics*, **SEP**, 208–217.

[106] Sackfield, A. & Hills, D.A. (1983) Some useful results in the classical Hertz contact problem. *Journal of Stress Analysis*, **18**, 107.

[107] Sato, K., Fuji, H., & Kodama, S. (1986) Crack propagation behavior in fretting fatigue. *Wear*, **107**, 245–262.

[108] Sato, K. (1992) Determination and control of contact pressure distribution in fretting fatigue. *Standardization of Fretting Fatigue Test Methods and Equipment*, ASTM STP 1159, M. Helmi Attia and R.B. Waterhouse, eds. American Society for Testing and Materials, 85–100.

[109] Suresh, S. & Ritchie, R.O. (1984) Propagation of short fatigue cracks. *International Metals Reviews*, **29**, 445–476.

[110] Suresh, S. (1991) *Fatigue of Materials.* Cambridge: Cambridge University Press.

[111] Suresh, S. (1998) *Fatigue of Materials.* 2^{nd} ed. Cambridge: Cambridge University Press.

[112] Tavernelli, J.F. & Coffin, L.F. A compilation and interpretation of cyclic strain fatigue tests on metals. *Transactions of the ASM*, **51**, 438–453.

[113] Tavernelli, J.F. & Coffin, L.F. (1962) Experimental support for generalized equation predicting low cycle fatigue. *Transactions of the ASME, Journal of Basic Engineering*, **84D**, 533–541.

[114] Tomlinson, G.A. (1927) The rusting of steel surfaces in contact. *Proceedings of the Royal Society, London, Series A*, **115**, 472–483.

[115] Tomlinson, G.A., Thorpe, P.L., & Gough, H.J. (1939) An investigation of fretting corrosion of closely fitting surfaces. *Proceedings of the Institution for Mechanical Engineers*, **141**, 223.

[116] Uhlig, H.H., Feng, I-Ming, et al. (1953) Fundamental investigation of fretting corrosion. NACA Technical Note 3029.

[117] Uhlig, H.H. (1954) Mechanism of fretting corrosion. *Journal of Applied Mechanics*, **21**, 401–407.

[118] Vincent, L., Berthier, Y., Dubourg, M.C., & Godet, M. (1992) Mechanics and materials in fretting. *Wear*, **153**, 135–148.

[119] Vingsbo, O. & Söderberg, S. (1988) On Fretting Maps. *Wear*, **126**, 131–147.

[120] Von Tein, V. & Seibert, P.E. (1974) *AGARD Conference Proceedings AGARD-CP-161*, Session 1, Paper 2, 1974.

[121] Warlow-Davies, E.J. (1941) Fretting corrosion and fatigue strength: brief results of preliminary experiments. *Proceedings of the Institution for Mechanical Engineers*, **146**, 32.

[122] Waterhouse, R.B. (1955) Fretting corrosion. *Proceedings of the Institution for Mechanical Engineers*, **169**, 1159-1172.

[123] Waterhouse, R.B. (1961) Influence of local temperature increases on the fretting corrosion of mild steel. *Journal of the Iron and Steel Institute*, **197**, 301-305.

[124] Waterhouse, R.B., Brook, P.A., & Lee, M.C. (1962) *Wear*, **5**, 235–244.

[125] Waterhouse, R.B. & Allery, M. (1965) *Wear*, **8**, 421–447.

[126] Waterhouse, R.B., Dutta, M.K., & Swallow, P.J. (1971*a*) Fretting fatigue in corrosion environments. *Proceedings of the conference on the mechanical behavior of materials*, 3, The Society of Materials Science, Japan, 294–300.

[127] Waterhouse, R.B. & Taylor, D.E. (1971*b*) The initiation of fatigue cracks in a 0.7% carbon steel by fretting. *Wear*, **17**, 139-147.

[128] Waterhouse, R.B. (1972) *Fretting Corrosion*, Oxford: Pergamon Press.

[129] Waterhouse, R.B. (1981) *Fretting Fatigue*, London: Elsevier Applied Science.

[130] Waterhouse, R.B. and Lindley, T.C. (1994) *Fretting Fatigue.* ESIS Publication No. 18, European Structural Integrity Society. Mechanical Engineering Publications Limited, London.

[131] Waters, K. (1959) *American Society for Testing of Materials Special Technical Publication 274*, 99–111.

[132] Wise, S. & Burdon, E.S. (1965) *Institute for Locomotive Engineering*, **54**, 298.

[133] Wright, G.P. (1970) Studies in fretting fatigue. Doctor of Philosophy thesis, Oxford University.